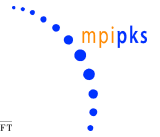


**TECHNISCHE  
UNIVERSITÄT  
DRESDEN**



MAX-PLANCK-GESELLSCHAFT



---

Fakultät Mathematik und Naturwissenschaften Fachrichtung Physik

---

Max-Planck-Institut für Physik komplexer Systeme

# High Harmonic Generation with Twisted Electrons

**Sebastian Gemsheim**

Born on: 13th June 1989 in Zwickau, Germany

**Master Thesis**

to achieve the academic degree

**Master of Science (M.Sc.)**

First referee

**Prof. Dr. Jan-Michael Rost**

Second referee

**Dr. Frank Grossmann**

Supervising professor

**Prof. Dr. Jan-Michael Rost**

Submitted on: 20th July 2018



## Abstract

The main objective of this thesis is an investigation toward the qualitative understanding of high harmonic generation with electrons possessing intrinsic orbital angular momentum in strong laser fields. A non-relativistic single-atom framework is chosen for this work. The emission pattern and the spectral intensity is investigated by means of a semiclassical spectrum based on the quantum mechanical expectation value of the electric dipole acceleration. A perturbative approach is used to include the magnetic field beyond the usual dipole approximation for the laser potential. Based on the corresponding interaction Hamiltonian, an analytical twisted wavefunction is derived in the strong field approximation, i.e., with the exclusion of the atomic binding potential. The dipole acceleration is calculated for an effective two-level system composed of one bound Hydrogen state and the twisted electron state. The use of twisted electrons does not change the high harmonic cutoff compared to untwisted electrons. However, the emission pattern is that of a rotating dipole, in contrast to the linear dipole emission of traditional high harmonic generation. Furthermore, the spontaneous recombination process restricts the number of possible recombination channels due to the conservation of angular momentum. The findings are confirmed by numerical integrations and supplemented by a full quantum simulation of the three-dimensional atomic system. The simulation results are in qualitative agreement with the analytical approximations. Quantum electrodynamical calculations complement the semiclassical approach and a formula for the recombination probability is derived. The final result is a full quantum mechanical, analytical expression for the generated high harmonic spectrum in a three-dimensional system with a twisted electron.

## Zusammenfassung

Die vorliegende Arbeit beschäftigt sich mit der qualitativen Untersuchung der Erzeugung Hoher Harmonischer im Emissionsspektrum von Rekombinationsprozessen mit Elektronen mit intrinsischem orbitalen Drehimpuls, beschleunigt in einem starken Laserfeld. Die nichtrelativistische Betrachtung eines einzelnen Atoms steht dabei im Fokus dieser Arbeit. Die Abstrahlcharakteristik und die spektrale Intensität werden mit Hilfe von elektromagnetischen Feldern untersucht, welche aus dem quantenmechanischen Erwartungswert der elektrischen Dipolbeschleunigung unter einer semiklassischen Betrachtungsweise gewonnen werden. Das magnetische Feld des Lasers wird durch eine störungstheoretische Behandlung des Vektorpotentials einbezogen und erweitert die übliche Dipolnäherung. Eine analytisch exakte Lösung der resultierenden Schrödingergleichung wird, unter der Vernachlässigung des atomaren Potentials, für das sogenannte „twisted“ Elektron hergeleitet. Weiterhin wird das Gesamtsystem durch ein effektives Zwei-Niveau-System, bestehend aus einem stationären gebundenen Zustand des Wasserstoffatoms und der Wellenfunktion des „twisted“ Elektrons, approximiert. Ein analytisch hergeleiteter Ausdruck für die Dipolbeschleunigung ermöglicht die Untersuchung der emittierten Strahlung. Im Gegensatz zum Emissionsprofil eines linearen Dipols in der traditionellen Erzeugung von Hohen Harmonischen ergab sich hierbei eine veränderte Abstrahlcharakteristik, die eines rotierenden Dipols. Die obere Grenze für das charakteristische, spektrale Plateau bleibt jedoch unverändert. Darüber hinaus wird die mögliche Zahl der Rekombinationsmöglichkeiten durch die Drehimpulserhaltung beschränkt. Die theoretischen Resultate werden durch numerische Integrationen bestätigt. Weiterhin erfolgt eine dreidimensionale quantenmechanische Simulation des vollen Systems zur Untersuchung des Einflusses des bindenden Potentials. Die Simulationsergebnisse zeigen eine qualitative Übereinstimmung mit den analytischen Approximationen. Nachfolgende quantenelektrodynamische Berechnungen vervollständigen die semiklassische Beschreibung und erlauben die Herleitung der Rekombinationswahrscheinlichkeit in Abhängigkeit der Wechselwirkungszeit. Das finale Ergebnis repräsentiert einen voll quantenmechanischen, analytischen Ausdruck für das Spektrum Hoher Harmonischer in einem dreidimensionalen System mit „twisted“ Elektronen.



# Contents

|  |           |
|--|-----------|
| <b>Abstract/Zusammenfassung</b>                                | <b>3</b>  |
| <b>1 Introduction</b>  | <b>7</b>  |
| <b>2 High Harmonic Generation</b>                              | <b>9</b>  |
| 2.1 Spectral characteristics . . . . .                         | 9         |
| 2.2 Semiclassical spectrum . . . . .                           | 10        |
| 2.3 Origin of spectral characteristics . . . . .               | 12        |
| <b>3 Twisted Electrons</b>                                     | <b>19</b> |
| 3.1 Twisted wavepackets . . . . .                              | 19        |
| 3.2 Generation of twisted electrons in experiment . . . . .    | 20        |
| 3.3 Construction from plane-waves . . . . .                    | 22        |
| <b>4 Model for HHG with Twisted Electrons</b>                  | <b>25</b> |
| 4.1 Hamiltonian of atomic system . . . . .                     | 25        |
| 4.2 Wavefunction splitting . . . . .                           | 25        |
| 4.3 Initial state . . . . .                                    | 27        |
| <b>5 Twisted Electrons in Strong Laser Field</b>               | <b>29</b> |
| 5.1 First order correction with $1/c$ -expansion . . . . .     | 29        |
| 5.2 Plane-wave Volkov solutions . . . . .                      | 31        |
| 5.3 Twisted wavepacket . . . . .                               | 32        |
| 5.4 Properties . . . . .                                       | 34        |
| 5.5 Laser and model parameters . . . . .                       | 37        |
| <b>6 Analytical Results</b>                                    | <b>39</b> |
| 6.1 Hydrogen atom . . . . .                                    | 39        |
| 6.2 Dipole acceleration . . . . .                              | 39        |
| 6.3 Spectrum of interference term . . . . .                    | 44        |
| <b>7 Numerical Results</b>                                     | <b>51</b> |
| 7.1 Dipole acceleration . . . . .                              | 51        |
| 7.2 Full quantum simulation . . . . .                          | 58        |
| 7.3 Results of simulation . . . . .                            | 59        |
| <b>8 Quantum Electrodynamical Approach</b>                     | <b>69</b> |
| 8.1 Theoretical groundwork . . . . .                           | 69        |
| 8.2 Spontaneous emission process . . . . .                     | 71        |
| 8.3 Radiative recombination . . . . .                          | 73        |
| 8.4 Connection to dipole acceleration formalism . . . . .      | 74        |
| 8.5 Results . . . . .  | 75        |
| 8.6 Application to quantum simulation - hybrid model . . . . . | 77        |
| <b>9 Conclusion and Outlook</b>                                | <b>79</b> |

---

|          |   |           |
|----------|---|-----------|
| <b>A</b> | <b>Theorems</b>   | <b>81</b> |
| A.1      | Plancherel theorem . . . . .  | 81        |
| A.2      | Ehrenfest theorem . . . . .   | 81        |
| <b>B</b> | <b>Calculations</b>   | <b>83</b> |
| B.1      | Plane-wave Volkov solutions in velocity and length gauge . . . . .                | 83        |
| B.2      | Derivation of $\phi$ -integration in plane-wave decomposition . . . . .           | 85        |
| B.3      | Momentum space integration of Volkov wavefunctions . . . . .                      | 85        |
| B.4      | Main integral . . . . .   | 89        |
| B.5      | Summation over emission directions . . . . .                                      | 92        |
| <b>C</b> | <b>Miscellaneous</b>  | <b>95</b> |
| C.1      | Atomic units . . . . .  | 95        |
| C.2      | Expectation value of momentum operator for stationary bound eigenstates . . . . . | 95        |

# 1 Introduction

One of the most fundamental principles in physics is to probe a system's response to an external stimulus and deduce the internal properties and dynamics from the accessible physical observables. However, the observable scales depend greatly on the typical scales of the stimulus. Hence, the greater the ability to control the external stimulus, the better will be the attainable insight into the internal mechanisms and the capability to ultimately tailor any desired response of the driven system. In the case of electromagnetic phenomena, these mechanisms are due to an interplay of radiation and charged particles. The systems under study can be composed of many such particles and may range from simple Hydrogen atoms to complex molecules, up to solid state structures. The fundamental electronic processes in such systems are confined to very small regions of space, i.e., down to inner atomic length scales, and happen on very short time-scales, i.e., classical orbital periods of the inner electrons. In order to probe and to control the processes taking place in any kind of matter it is necessary to engineer ultrashort, high-energetic pulses of light. This is the domain of femto- ( $10^{-15}$ ) and attosecond ( $10^{-18}$ ) time scales and an electromagnetic energy range spanning from visible light to x-ray radiation (Figure 1.1).

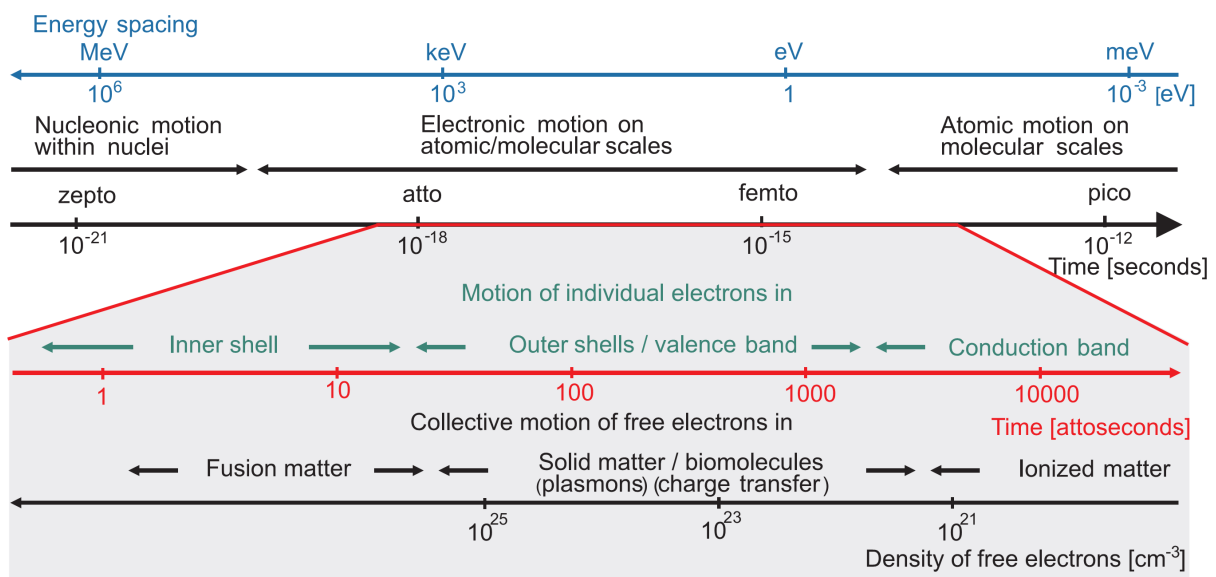


Figure 1.1: The relevant time and energy scales for microscopic motion of nucleons, electrons and atoms is shown in the upper part. The lower part comprises a further distinction of time scales for individual and collective electronic motion in ensembles of electrons with varying density. Reprinted from [1]

The advances in laser technologies led to the generation of femtosecond (fs) pulses with 2.6 fs pulse duration in the near infrared regime [2]. Yet, this time resolution is not sufficient to probe inner shell electron dynamics (Figure 1.1). The discovery of high harmonic generation [3] in 1987 marked an important step toward the generation of sub-femtosecond pulses. It constitutes the highly non-linear process of converting many low-frequency photons to a single high-energetic photon by means of an atomic system driven by a laser. 25 years later, high harmonic generation of orders greater than 5000 became experimentally feasible and the resulting x-ray emission could theoretically support a single-cycle pulse of 2.5 attoseconds [4]. The application of soft

x-ray sub-femtosecond pulses from high harmonic generation has been experimentally demonstrated for the observation of the time-resolved emission of Auger electrons [5]. Many theoretical and experimental efforts are underway to further increase the accessible photon energy and the conversion efficiency.

In 1992 and 2007, respectively, it was realized that photons and electrons can possess an intrinsic orbital angular momentum in free space. Due to their vortex character they have been named “twisted” light or “twisted” electrons. The intrinsic orbital angular momentum represents a relatively new theoretical and experimental concept and serves as an additional degree of freedom. Theoretical studies for twisted electrons include non-relativistic [6] and relativistic approaches, including electron spin effects [7]. Also the experimental generation has been demonstrated, for example in electron microscopes, and became a common tool in the last years [8]. The possible applications of twisted beams are manifold. For example, twisted light has been used for the rotation of optically trapped micro-objects [9], while twisted electrons have the potential to measure magnetic properties of materials at a desired spatial resolution [10]. At a more fundamental level, it is believed that twisted electrons might help to resolve the spin structure of the proton in high-energy vortex-particle collisions [11].

The availability of a new degree of freedom for light and electrons offers a great opportunity to explore new techniques for the enhancement and the control of high harmonic emission. First steps have been undertaken to incorporate twisted light into strong field physics [12, 13, 14, 15], including high harmonic generation. An unexplored domain is however the combination of twisted electrons with high harmonic generation. The goal of this thesis is to take a first step toward closing this gap and to combine both concepts. We aim to qualitatively understand the dynamics involved and to characterize the emission spectrum. Today's laser technologies can cover large regions in the energy-time domain and necessitate an appropriate theoretical treatment depending on the two laser parameters, intensity and frequency. Therefore, we decide to work in a non-relativistic setting and do not take spin into account. For the purpose of investigating the elementary dynamics, we focus on a single Hydrogen atom.

A brief introduction of the concepts of high harmonic generation and twisted electrons is given in Chapters 2 and 3, respectively. The model Hamiltonian and the choice of the initial conditions are presented in Chapter 4 and the behavior of twisted electrons in a strong laser field is treated in Chapter 5. Chapter 6 contains the analytical derivations of the high harmonic spectrum of twisted electrons driven by a strong laser field. We confirm and extend the results from the preceding chapter with numerical integrations and simulations in Chapter 7. The approach of a quantum electrodynamical setting is discussed in Chapter 8. We conclude in Chapter 9 and give an outlook of different possibilities that can be explored to improve the results obtained in this work.



# 2 High Harmonic Generation

High harmonic generation (HHG) describes the characteristic light emission of a quantum mechanical system, e.g., atom or molecule, driven by a strong laser field with an angular frequency  $\omega_0$ . High harmonics refer to the peaks in the emission spectrum for angular frequencies which are multiples of the base frequency, i.e.,  $\omega = n\omega_0$  ( $n \in \mathbb{N}$ ). The underlying quantum mechanical process is highly non-linear and converts many low-frequency photons from the driving mode to one high-frequency photon. The special features of this mechanism are described in this chapter and start with a summary of the typical spectral pattern in Section 2.1. It is followed by the derivation of a semiclassical (SC) dipole spectrum in Section 2.2. Section 2.3 gives an overview of explanations for HHG phenomena based on the quantity introduced in the preceding section.

## 2.1 Spectral characteristics

A typical HHG emission spectrum begins with a strong peak at the laser frequency  $\omega_0$  and a steady decay in intensity for increasing photon energy. Contrary to intuition, the spectrum does not decline further with increasing frequency but exhibits a plateau for higher-order harmonics of the laser frequency  $\omega_0$ . The spectral intensity is approximately equal for a wide range of frequencies and is called the plateau. Following the plateau comes a sharp cutoff at an angular frequency  $\omega_{\text{cutoff}}$  (Figure 2.1). It became apparent that this cutoff frequency depends on the sum of the atomic ionization potential  $I_p$  and the ponderomotive potential energy  $U_p = q^2 E_0^2 / (4m_e \omega_0^2)$  times a constant numerical prefactor  $\eta$ . In a typical single-atom scenario its value is close to  $\eta \approx 3.17$ ,

$$\omega_{\text{cutoff}} = I_p + \eta \cdot U_p \quad \eta \in \mathbb{R}_+ . \quad (2.1)$$

The plateau itself exhibits a more fine-grained structure, namely the pronounced peaks at odd high harmonics  $\omega = (2n + 1)\omega_0$  ( $n \in \mathbb{N}$ ). It has been shown that the emitted high-energetic pulses have a very short pulse-length, being only a fraction of the driving cycle period, e.g., on the attosecond scale for an infrared driving field [16, 17]. A typical spectrogram is shown in Figure 2.1.

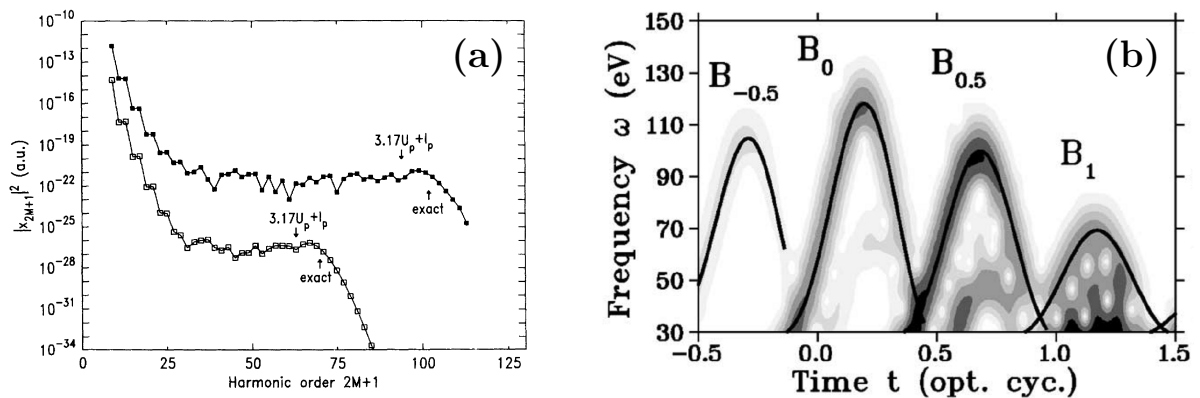


Figure 2.1: (a) A typical HHG spectrum shows a plateau region and a high-frequency cutoff. Reprinted from [18]. (b) A spectrogram of the HHG emission displays the chirped time-dependent emission of different high harmonics. Reprinted from [16].

Even though HHG fundamentals can be described within a single-atom framework, a typical experimental setting involves an ensemble of atoms (e.g., dilute gas) and macroscopic effects have to be taken into account. Such realistic systems have a high complexity and in order to obtain, for example, attosecond pulses or pulse trains, one has to carefully tune experimental parameters to balance the interplay of microscopic and macroscopic responses. Such macroscopic effects include, for example, propagation through a medium, phase-matching, the spatial profile of the laser, the Gouy phase and plasma effects [19].

## 2.2 Semiclassical spectrum

In almost all studies of HHG the emission spectrum is investigated through dipole responses of the atomic system. The radiated electric field is calculated in terms of classical electrodynamics as the emission of a classical dipole moment  $\vec{d} = q\vec{r}$ . The electric charge of the electron is denoted with  $q = -|e|$ . Quantum mechanical effects are incorporated by means of the quantum mechanical expectation value of the dipole operator for an atomic system in state  $|\psi(t)\rangle$  at time  $t$

$$\vec{d}(t) = \langle \psi(t) | q\hat{\vec{r}} | \psi(t) \rangle. \quad (2.2)$$

The emission spectrum is defined by the total radiated energy. It can be expressed as the time- and area-integrated energy flux of the electromagnetic radiation. The flux is known as the Poynting vector

$$\vec{S}(t) \equiv \frac{\vec{E}(t) \times \vec{B}(t)}{\mu_0}. \quad (2.3)$$

The electric and the magnetic fields are denoted by  $\vec{E}$  and  $\vec{B}$ , respectively.  $\mu_0$  is the magnetic constant or vacuum permeability. The total radiated energy  $\mathcal{E}_{\text{SC,em}}$  of an emitting volume  $V$  is given as

$$\mathcal{E}_{\text{SC,em}} = \int_{-\infty}^{\infty} dt \int_{A(V)} d\vec{A} \cdot \vec{S}(t). \quad (2.4)$$

The electric and the magnetic field of an electric dipole moment  $\vec{d}$  in the far field ( $r \gg 1$ ) depend solely on its acceleration  $\vec{a}(t) \equiv \ddot{\vec{d}}(t)$ . At a fixed observation point  $\vec{r}$  they are described [20] by

$$\vec{B}(\vec{r}, t) = \frac{\mu_0}{4\pi cr} \left( \vec{a} \left( t - \frac{r}{c} \right) \times \vec{e}_r \right), \quad (2.5)$$

$$\vec{E}(\vec{r}, t) = c \cdot \vec{B}(\vec{r}, t) \times \vec{e}_r. \quad (2.6)$$

The speed of light in vacuum is denoted by  $c$ . Thus the Poynting vector for the dipole emission in the far field reads

$$\vec{S}(\vec{r}, t) = \frac{\mu_0}{(4\pi)^2 cr^2} \left( \vec{a} \left( t - \frac{r}{c} \right) \times \vec{e}_r \right)^2 \cdot \vec{e}_r. \quad (2.7)$$

The radiated power through a sphere at distance  $r$  from the emitting source is given by

$$\int d\Omega r^2 \vec{e}_r \cdot \vec{S}(\vec{r}, t) = \frac{\mu_0}{(4\pi)^2 c} \int_0^{2\pi} d\varphi \int_0^\pi d\theta \sin \theta \left( \vec{a} \left( t - \frac{r}{c} \right) \times \vec{e}_r \right)^2. \quad (2.8)$$

Neglecting the constant retardation term and using the relations

$$(\vec{a} \times \vec{e}_r)^2 = \vec{a}^2 - (\vec{a} \cdot \vec{e}_r)^2, \quad (2.9)$$

$$\int_0^{2\pi} d\varphi \int_0^\pi d\theta \sin\theta (\vec{a} \cdot \vec{e}_r)^2 = \frac{4\pi}{3} \vec{a}^2, \quad (2.10)$$

the total radiated energy simplifies [21] to

$$\mathcal{E}_{\text{SC,em}} = \frac{2}{3} \frac{\mu_0}{4\pi c} \int_{-\infty}^{\infty} dt |\vec{a}(t)|^2. \quad (2.11)$$

We assume that far in the past and far in the future the acceleration vanishes and is a sufficiently well-behaving function in the space of square-integrable functions. The Plancherel theorem relates this expression to the Fourier transform  $\tilde{\vec{a}}(\omega)$  of the dipole acceleration under these conditions (see Appendix A.1)

$$\mathcal{E}_{\text{SC,em}} = \frac{2}{3} \frac{\mu_0}{4\pi c} \int_{-\infty}^{\infty} d\omega |\tilde{\vec{a}}(\omega)|^2 = \frac{\mu_0}{3\pi c} \int_0^{\infty} d\omega |\tilde{\vec{a}}(\omega)|^2. \quad (2.12)$$

The last relation follows from  $\tilde{\vec{a}}(-\omega) = \tilde{\vec{a}}^*(\omega)$  due to the reality of  $\vec{a}$ . Physically speaking, the total energy of an integrated signal in time or frequency space is the same. This defines the central quantity of HHG, the spectral intensity

$$\boxed{\mathcal{S}(\omega) \equiv |\tilde{\vec{a}}(\omega)|^2}. \quad (2.13)$$

It should be mentioned that the application of the correspondence principle should be applied to the full quantity  $\mathcal{S}(\omega)$  and not just the dipole acceleration because of

$$\langle |\tilde{\vec{a}}(\omega)|^2 \rangle \neq |\langle \tilde{\vec{a}}(\omega) \rangle|^2. \quad (2.14)$$

Lappas [22] showed that the spectral contributions can be split into a coherent part  $|\langle \tilde{\vec{a}}(\omega) \rangle|^2$  and an incoherent part  $\langle |\delta \tilde{\vec{a}}(\omega)|^2 \rangle$ , such that

$$\mathcal{S}(\omega) = |\langle \tilde{\vec{a}}(\omega) \rangle|^2 + \langle |\delta \tilde{\vec{a}}(\omega)|^2 \rangle. \quad (2.15)$$

The fluctuation is defined as the deviation from the expectation value, i.e.,  $\delta \tilde{\vec{a}}(\omega) \equiv \tilde{\vec{a}}(\omega) - \langle \tilde{\vec{a}}(\omega) \rangle$ . The incoherent part is neglected in this thesis and we will work with Equation (2.13).

If the initial and final dipole moment and velocity vanish, Equation (2.13) can be transformed to an expression with the dipole moment or dipole velocity via partial integrations

$$\left| \int dt e^{i\omega t} \ddot{\vec{d}}(t) \right|^2 = \omega^2 \left| \int dt e^{i\omega t} \dot{\vec{d}}(t) \right|^2 = \omega^4 \left| \int dt e^{i\omega t} \vec{d}(t) \right|^2. \quad (2.16)$$

### 2.2.1 Dipole acceleration

The time derivative of the expectation value of an arbitrary operator  $\hat{\mathcal{O}}$  is given by the Ehrenfest theorem (see Appendix A.2)

$$\frac{d}{dt} \langle \hat{\mathcal{O}} \rangle = \frac{i}{\hbar} \langle [\hat{H}, \hat{\mathcal{O}}] \rangle + \left\langle \frac{\partial \hat{\mathcal{O}}}{\partial t} \right\rangle. \quad (2.17)$$

Assuming a 1D Hamiltonian  $\hat{H} = \hat{p}^2/2m + V(\hat{x}, t)$ , this leads to

$$\frac{d}{dt}\langle\hat{p}\rangle = \langle-\partial_x V(x, t)|_{x=\hat{x}}\rangle, \quad (2.18)$$

$$\frac{d}{dt}\langle\hat{x}\rangle = \frac{\langle\hat{p}\rangle}{m}. \quad (2.19)$$

The last line shows that with Equation (2.16) the spectrum can also be formulated in terms of momentum operator expectation values (dipole velocity). Taking the time derivative of the last line and inserting the first line leads to an expression in terms of the potential gradient, i.e., the force operator

$$\boxed{q\frac{d^2}{dt^2}\langle\hat{x}\rangle = -\frac{q}{m}\langle\partial_x V(x, t)|_{x=\hat{x}}\rangle}. \quad (2.20)$$

Although, it should be noted that several authors have advised the use of the dipole velocity instead of the dipole acceleration to determine the spectrum of a microscopic single-atom theory [23, 24].

## 2.3 Origin of spectral characteristics

Many attempts have been made to understand the characteristics of HHG spectra. The methods have ranged from full quantum mechanical numerical simulations to semiclassical and classical analytical approaches. The HHG dynamics is usually described with the Three-Step model [25], in which a neutral atom in the ground state is considered as the initial state. The successive steps of the process are shown in Figure 2.2 and outlined below.

1. Tunnel ionization of the atom, such that a part of the electron wavefunction effectively leaves the core potential; some fraction of the wavefunction remains in the atomic state.
2. Free electron motion in laser field.
3. Eventually the electron returns to the nucleus and has a chance to radiatively recombine with the nucleus.

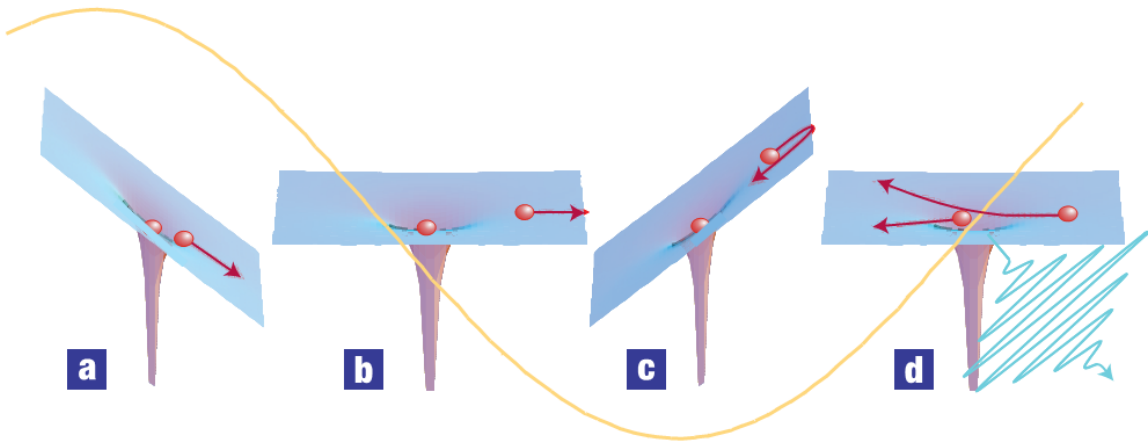


Figure 2.2: The three sequential steps of the HHG process are displayed. The electron tunnels out of the binding potential (a), is accelerated in the electric field (b, c) and a fraction recombines with the parent ion under the emission of one high-energetic photon (d). Reprinted from [26].

All features of the HHG emission spectrum can be explained with a 1D Hamiltonian

$$\hat{H} = \frac{\hat{p}^2}{2m_e} + V(\hat{x}) - q\hat{x}E(t). \quad (2.21)$$

The binding potential  $V$  is assumed to be centered around the origin  $x = 0$ . Here and subsequently, the term  $f(\hat{x})$  is to be understood as a Taylor expansion in terms of polynomials of the operator  $\hat{x}$ . Each of the three main characteristics is explained in the subsequent Sections 2.3.1, 2.3.2 and 2.3.3.

### 2.3.1 Cutoff

As stated in Section 2.1, the cutoff frequency will depend on the kinetic energy the electron can obtain in the laser field. One quasiclassical and two semiclassical approaches for a derivation of the cutoff will be explained below.

1. **Quasiclassical (“recollision picture”)**: This refers to a classical description of the electron motion after quantum mechanically tunneling out of the binding potential under the influence of the laser field. The free electron starts its motion in the vicinity of the core at  $x \approx 0$  with no velocity  $v \approx 0$  and after some time it can eventually recollide with the atom if it returns to  $x \approx 0$ . The radiated energy is then equal to  $E_{\text{kin}} + I_p$ . Hence, the maximal kinetic energy the electron can acquire until recollision depends on the time of ionization  $t_0$ . Different ionization times correspond to different phases of the electric field. However, the recombination with the parent ion is of quantum mechanical nature. The classical equations of motion for (2.21) with  $V = 0$  and a continuous-wave field  $E(t) = E_0 \cos(\omega_0 t)$  are

$$m_e \dot{v}(t) = qE(t), \quad (2.22)$$

$$v(t) = \frac{qE_0}{m_e \omega_0} [\sin(\omega_0 t) - \sin(\omega_0 t_0)], \quad (2.23)$$

$$E_{\text{kin}}(t) = \frac{m_e}{2} v^2(t) = 2U_p [\sin(\omega_0 t) - \sin(\omega_0 t_0)]^2, \quad (2.24)$$

$$x(t) = -\frac{qE_0}{m_e \omega_0^2} [\cos(\omega_0 t) - \cos(\omega_0 t_0) + \sin(\omega_0 t_0)(t - t_0)]. \quad (2.25)$$

Solving for  $x(t_1) = 0$  ( $t_1 > t_0$ ) leads to a transcendental equation but can be tackled numerically. The maximal kinetic energy upon recollision in dependence of the ionization time is shown in Figure 2.3 and its maximum equals approximately 3.17 units of the ponderomotive energy  $U_p$ .

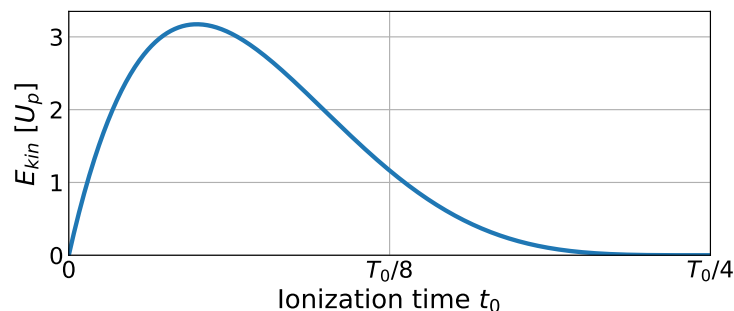


Figure 2.3: The classical kinetic energy upon return to the initial position of a charged particle moving in an oscillatory electric field is shown in dependence on the initial phase of the field, given in units of the laser period  $T_0 = 2\pi/\omega_0$ .

The kinetic energy has maxima for ionization times  $\omega_0 t_0 \approx 17^\circ + n \cdot 180^\circ \approx \pi/10 + n\pi$  ( $n \in \mathbb{N}$ ) and has a maximum value [27] of

$$E_{\text{kin,max}} \approx 3.17U_p. \quad (2.26)$$

2. **Semiclassical:** In the seminal paper by Lewenstein [18] the dipole moment was investigated with the following important assumptions:

- Only a small fraction of the electronic bound states becomes ionized.
- The influence of the binding potential  $V$  on the free motion of the ionized part is negligible.
- The ground state  $|0\rangle$  is the only bound state important for HHG dynamics.

The full wavefunction, in atomic units (Appendix C.1), is written as

$$|\psi(t)\rangle = e^{iI_p t} \left( |0\rangle + \int d^3\vec{p} b(\vec{v}, t) |\vec{v}\rangle \right) \quad (2.27)$$

with the continuum states  $|\vec{v}\rangle$ . The temporal evolution of the continuum coefficients  $b(\vec{v}, t)$  is obtained from the Schrödinger equation with the Hamiltonian (2.21) in 3D. The electric field is linearly polarized in  $x$ -direction. The final expression for the dipole moment reads

$$\begin{aligned} \langle \psi(t) | \hat{x} | \psi(t) \rangle = & \\ & i \int_0^t dt' \int d^3\vec{p} \underbrace{E_0 \cos(\omega_0 t') d_x(\vec{p} - \vec{A}(t'))}_{\text{tunneling}} \underbrace{e^{-iS(\vec{p}, t, t')}}_{\text{motion in laser}} \underbrace{d_x^*(\vec{p} - \vec{A}(t))}_{\text{recombination}} + \text{c.c.} \end{aligned} \quad (2.28)$$

with the transition element  $\vec{d}(\vec{v}) = \langle \vec{v} | \hat{r} | 0 \rangle$  and the quasiclassical action  $S(\vec{p}, t, t')$ . The vector potential of the laser field is denoted by  $\vec{A}$ . The most important contributions in the momentum integral come from the stationary points of  $S$

$$\vec{\nabla}_{\vec{p}} S(\vec{p}, t, t') = \vec{r}(t) - \vec{r}(t') \stackrel{!}{=} 0. \quad (2.29)$$

The solutions to this equation are just the contributions from electrons returning to the vicinity of the nucleus. Without going into detail, the important “trajectories” for high harmonic generation are those born with zero initial velocity, which was one of the assumptions in the quasiclassical picture. Furthermore, they show that for  $I_p \ll U_p$  the saddle-point conditions lead to the dynamical equations of the quasiclassical approach, having a solution of  $3.17U_p$  for the maximal kinetic energy. Higher energetic “trajectories” do not contribute significantly to the integral, the reason being the cancellation of rapidly oscillating action phases. Additionally, they were able to show that only odd harmonics contribute due to symmetry reasons, but this is further explored in Section 2.3.2.

3. **Semiclassical Two-Step model:** The qualitative study of HHG with wavefunctions becomes even simpler if the quantum mechanical tunneling process is assumed to have already taken place. In this context the dynamics is simplified and the following model can be seen as a proxy to investigate HHG dynamics. An electron wavepacket is deployed at initial time  $t = 0$  at some distance away from a bare ionic core [28]. It can be either a fully depleted Hydrogen atom or a larger atom with full single electron ionization within the single-active electron approximation. Contrary to the Three-Step model, the phase of the laser field at which the free motion starts is a free parameter. Nevertheless, it can

qualitatively describe the mechanism behind the cut-off, even though the numerical value of the prefactor of  $U_p$  will be different than 3.17. After the first encounter with the ion a fraction of the wavefunction recombines and the bound state has a non-vanishing probability density, which is important for the high harmonic frequencies to emerge in the dipole spectrum, as can be seen below.

The wavefunction superposition (2.27) can be further reduced by approximation of the continuum part by a semiclassical wavepacket with a quantum mechanical phase  $\Phi_f(t)$ , determined by the classical action in the laser field, namely

$$\psi(x, t) \approx c_b(t)\chi_b(\vec{r})e^{-i\Phi_b(t)/\hbar} + c_f(t)\chi_f(x, t)e^{-i\Phi_f(t)/\hbar}. \quad (2.30)$$

The subscripts indicate the free (f) and bound (b) part of the full wavefunction. This rather strong assumption is justified by the observation of localized dynamics for semiclassical trajectories [29]. It is hereinafter referred to as *wavefunction splitting*. The phase of the bound state  $\Phi_b(t) \approx I_p t \geq 0$  can be approximated to depend only on the binding potential. The phase of the free part is determined by the action of the classical trajectory of an electron in the laser field, namely  $\Phi_f(t) = -U_p(t + \sin(2\omega_0 t)/(2\omega_0)) \leq 0$ . The initial position of the wavepacket center is chosen to be the maximum quiver amplitude and is subsequently driven toward the ion, i.e.,  $x(t) = x_{\max} \cos(\omega_0 t)$  and  $E(t) = E_0 \cos(\omega_0 t)$ . As in the Lewenstein model, the Coulomb potential is assumed to have negligible influence for sufficiently strong fields. The dipole spectrum (2.13) of the full wavefunction (2.30) contains the interference term of both states

$$\mathcal{S}(\omega) \propto \left| \int dt e^{i\omega t} e^{-i(\Phi_b(t) - \Phi_f(t))/\hbar} \cdot c_b^*(t)c_f(t) \int dx (\dots) \right|^2. \quad (2.31)$$

The factor in parenthesis includes wavepacket spreading, temporal change of the coefficients and the movement of the wavepacket center. The last two effects happen on the timescale of the driving period and do not contribute to the plateau frequencies. Diffusion timescales are also negligible if the initial width is not very small, e.g., much smaller than the Bohr radius. Only the stationary phases are important for the Fourier transform and, accordingly, the extremal points are obtained from the phase difference

$$\frac{d}{dt} [\hbar\omega t - (\Phi_b(t) - \Phi_f(t))] = 0, \quad (2.32)$$

$$\hbar\omega - \left[ I_p + U_p \underbrace{(\cos(2\omega_0 t) + 1)}_{=2\cos^2(\omega_0 t)} \right] = 0. \quad (2.33)$$

Thus, the maxima are obtained for stationary points  $\omega_0 t_{\max} = n\pi$  ( $n \in \mathbb{N}$ ) and lead to the maximum frequency

$$\boxed{\hbar\omega_{\max} = I_p + 2U_p}. \quad (2.34)$$

Such high-energetic photons are emitted when the free wavepacket center is in the vicinity of the origin ( $x(t_{\max}) = 0$ ). The minimal obtainable frequency for the stationary phases is  $\hbar\omega_{\min} = I_p$  and marks the lower end of the plateau region. Associated emission times  $\omega_0 t_{\min} = (2n + 1)\pi$  correspond to electron locations furthest away, namely  $x(t_{\min}) = x_{\max}$ . Equation (2.31) reveals also the importance of both states being populated to exhibit high harmonic generation.

### 2.3.2 Odd harmonic peaks

The separation of HHG peaks can be explained within the semiclassical 2-step picture. The phase of the free wavepacket can be rewritten with the Jacobi-Anger expansion

$$e^{iz \sin \theta} = \sum_{k=-\infty}^{\infty} J_k(z) e^{ik\theta}. \quad (2.35)$$

Bessel functions of the first kind are denoted by  $J_k(z)$ . The interference term (2.31) reads then

$$\mathcal{S}(\omega) \propto \left| \int dt e^{i\omega t} \sum_{k=-\infty}^{\infty} J_k\left(\frac{U_p}{2\hbar\omega_0}\right) e^{-i(I_p+U_p+2k\hbar\omega_0)t/\hbar} \cdot c_b^*(t) c_f(t) \int dx (\dots) \right|^2. \quad (2.36)$$

It becomes apparent that a stationary phase analysis leads to a separation of twice the laser frequency between adjacent peaks,  $\Delta\omega = 2\hbar\omega_0$ . The cutoff frequency is now set by the Bessel function and can be derived from its asymptotic form [30]

$$J_k(x) \xrightarrow{|k| \gg 1} \frac{(-1)^k}{\sqrt{2\pi|k|}} \left(\frac{ex}{2|k|}\right)^{|k|}. \quad (2.37)$$

This function declines rapidly for  $|k| \gtrsim x$ . Hence, the lower and upper boundary of the plateau correspond to  $k_{\text{bound}} = \pm \lfloor U_p/(2\hbar\omega_0) \rfloor$  and lead to the same maximum frequency (2.34).

### Generalized parity transformation

Even though this shows the separation of the peaks in the plateau, the semiclassical method cannot explain the lack of even harmonics in the spectrum. An underlying symmetry of the Hamiltonian (2.21) is responsible for odd multiples of the laser frequency [30]. The only other assumption necessary is the even symmetry of the binding potential term under spatial parity transformations,  $V(-x) = V(x)$ . Then the Hamiltonian is not only symmetric under periodic time translations  $\hat{\mathcal{P}}_T : t \rightarrow t + T$  ( $T = 2\pi/\omega_0$ ), but also under the generalized parity transformation

$$\hat{\mathcal{P}}_G : \quad x \rightarrow -x \quad t \rightarrow t + \frac{T}{2}. \quad (2.38)$$

The Floquet theorem states that the general solution to the Schrödinger equation of harmonically driven systems can be written as a superposition

$$\Psi(x, t) = \sum_n c_n e^{-i\epsilon_n t/\hbar} \psi_n(x, t) \quad (2.39)$$

of Floquet states  $\psi_n(x, t)$ . These Floquet states are eigenfunctions of the Floquet operator  $\hat{\mathcal{H}} \equiv \hat{H} - i\hbar\partial_t$ , i.e.,

$$\hat{\mathcal{H}}\psi_n(x, t) = \epsilon_n\psi_n(x, t), \quad (2.40)$$

and have time-periodicity  $\hat{\mathcal{P}}_T\psi_n(x, t) = \psi_n(x, t+T) = \psi_n(x, t)$ . The energy variables  $\epsilon_n$  are called quasienergies. The commutator  $[\hat{\mathcal{P}}_G, \hat{\mathcal{H}}] = 0$  vanishes and a set of simultaneous eigenfunctions exists, which is either even or odd under the generalized parity transformation

$$\hat{\mathcal{P}}_G\psi_n(x, t) = \psi_n(-x, t + T/2) = \pm\psi_n(x, t). \quad (2.41)$$



The eigenvalues can be derived from the relations  $\widehat{\mathcal{P}}_T = \widehat{\mathcal{P}}_G^2$  and  $\lambda_T = 1$  for  $\widehat{\mathcal{P}}_T \psi_n = \lambda_T \psi_n$ , leading to

$$\lambda_T = \lambda_G^2 = 1 \quad \Rightarrow \quad \lambda_G = \pm 1. \quad (2.42)$$

In order to see the effect of the symmetry on the spectrum we consider the Fourier transform of the dipole moment instead of the acceleration form (see Equation (2.16)). In general, the integration limits are finite. However, for simplicity, they shall be minus and plus infinity in the following. Substituting the expansion in Floquet states ( $\omega_n \equiv \epsilon_n/\hbar$ ) gives

$$\int dt e^{i\omega t} \langle x \rangle = \sum_{m,n} c_m^* c_n \int_{-\infty}^{\infty} dt e^{i(\omega - \omega_n + \omega_m)t} \int_{-\infty}^{\infty} dx x \psi_m^*(x, t) \psi_n(x, t). \quad (2.43)$$

Splitting the spatial integral in half and using the symmetry under the generalized parity transformation leads to

$$\int dt e^{i\omega t} \langle x \rangle = \sum_{m,n} c_m^* c_n \int_{-\infty}^{\infty} dt e^{i(\omega - \omega_n + \omega_m)t} \left[ 1 \pm e^{i\pi \left( \frac{\omega - \omega_n + \omega_m}{\omega_0} \right)} \right] \int_0^{\infty} dx x \psi_m^*(x, t) \psi_n(x, t) \quad (2.44)$$

$$\begin{aligned} &= \sum_{m,n \neq m} c_m^* c_n \int_{-\infty}^{\infty} dt e^{i(\omega - \omega_n + \omega_m)t} \left[ 1 \pm e^{i\pi \left( \frac{\omega - \omega_n + \omega_m}{\omega_0} \right)} \right] \int_0^{\infty} dx x \psi_m^*(x, t) \psi_n(x, t) \\ &+ \left[ 1 - e^{i\pi \left( \frac{\omega}{\omega_0} \right)} \right] \cdot \underbrace{\int_{-\infty}^{\infty} dt e^{i\omega t} \sum_n |c_n|^2 \int_0^{\infty} dx x |\psi_n(x, t)|^2}_{\geq 0}. \end{aligned} \quad (2.45)$$

The minus sign corresponds to the dipole elements between Floquet states with equal generalized parity and the plus sign to different generalized parities. The square bracket term in the last line vanishes for even multiples of the laser frequency  $\omega = 2k\omega_0$  and has maxima for odd multiples. In general, the wavefunction is in a superposition of Floquet states and their contributions add up for odd harmonic frequencies. The amplitude maxima of the first line are spread across the spectrum. If the quasienergies are taken to be in the first Brillouin zone,  $-\omega_0/2 \leq \omega_n \leq \omega_0/2$ , the peak frequency can be determined to be between integer multiples of  $\omega_0$ . The first line maximum frequencies are

$$\omega_{\max,1} = \pm \Delta_{mn} + \omega_0 \cdot \begin{cases} 2k & \text{different generalized parity} \\ (2k+1) & \text{same generalized parity} \end{cases}, \quad (k \in \mathbb{Z}). \quad (2.46)$$

The energy difference is defined as  $\Delta_{mn} = \omega_m - \omega_n$ . However, their intensity is smaller compared to odd harmonic frequencies since only single pairs of different Floquet states prompt this emission. Hence, the peaks for odd harmonics are more pronounced than frequencies from interference terms of different Floquet states. A more comprehensive analysis can be performed if the Floquet states are decomposed into discrete Fourier modes [31], but this is beyond the scope of this thesis.

### 2.3.3 Plateau region

The plateau structure originates from the interference term of bound and free parts of the electron wavefunction. That the spectral intensity of different high harmonics is of the same order will be explained with (2.36). The contributions of the Bessel functions for different  $k \in \left( -\frac{U_p}{2\hbar\omega_0}, \frac{U_p}{2\hbar\omega_0} \right)$

within the plateau region is similar in magnitude. Without mathematical proof, we refer to Figure 2.4 and present numerical evidence for  $U_p/(2\hbar\omega_0) = 30$ .

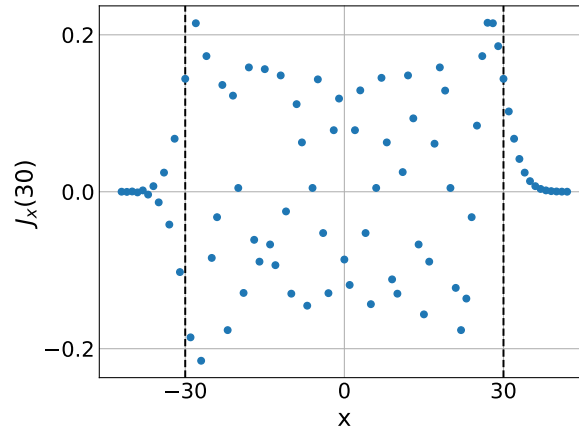


Figure 2.4: The values for different orders  $x$  of Bessel functions  $J_x(z)$  with fixed argument  $z$  are equal in magnitude as long as  $x \leq z$ . The exponential decay, described in Section 2.3.2, occurs for values  $x > z$ .

# 3 Twisted Electrons

In this chapter we will introduce the notion of twisted wavepackets in Section 3.1 and present some of their properties. However, only the most important features will be explained without going too much into detail. Afterwards, we briefly mention two experimental realizations for the generation of twisted electrons in Section 3.2, and finally, a possible construction through the superposition of plane-waves is explained in Section 3.3. This will be an important tool for the treatment of twisted electrons in a strong laser field.

## 3.1 Twisted wavepackets

In 1992 Allen et al. [32] showed that Maxwell's equations admit a free space solution in cylindrical coordinates  $(\rho, \varphi, z)$  in the paraxial approximation describing Laguerre-Gaussian beams with a phase factor of the form

$$\vec{E} \propto \exp(il\varphi + kz), \quad l \in \mathbb{Z}. \quad (3.1)$$

Furthermore, they demonstrate that it accounts for an intrinsic orbital angular momentum (OAM) of  $l\hbar$  per photon. Due to the phase singularity at  $\rho = 0$  it is referred to as “optical vortices” or “twisted light”. Bliokh et al. [6] showed in 2007 that the Schrödinger equation in free space admits a similar solution in the paraxial approximation with

$$\psi_{\text{T}} \propto f(\rho, z) \exp(il\varphi + p_c z / \hbar) \quad (3.2)$$

and some envelope function  $f$ . The momentum  $p_c$  is assumed to be the central momentum of  $\psi_{\text{T}}$  such that  $\langle \hat{p} \rangle = p_c \vec{e}_z$ . Such wavefunctions are called “structured matter waves”, “vortex wavepackets” or “twisted wavepackets”. They will be indicated by a subscript T. Their distinguishing properties result from the aforementioned phase factor. A vortex wavepacket is an eigenfunction of the  $z$ -component of the orbital angular momentum operator  $\hat{L}_z \psi_{\text{T}} = -i\hbar \partial \varphi \psi_{\text{T}} = l\hbar \psi_{\text{T}}$ . Interestingly, this orbital angular momentum does not have a classical counterpart and is an *intrinsic* property of the wavefunction, independent of the chosen coordinate system [33]. In contrast to classical orbital angular momentum, the expectation value of the orbital angular momentum operator

$$\langle \hat{L} \rangle = l\hbar \frac{\langle \hat{p} \rangle}{|\langle \hat{p} \rangle|} \quad (3.3)$$

is *longitudinal* for a twisted wavefunction of form (3.2) with respect to its central momentum. Additionally, it is easily shown that the expectation value of the position operator  $\langle \hat{r} \rangle$  still follows a rectilinear motion along  $\vec{e}_z$ . Hence, the expectation value of the classical orbital angular momentum vanishes, i.e.,

$$\langle \hat{r} \rangle \times \langle \hat{p} \rangle = 0. \quad (3.4)$$

Moreover, the probability current density

$$\vec{j} \propto p_c \vec{e}_z + \frac{l\hbar}{r} \vec{e}_\varphi \quad (3.5)$$

shows the same characteristic behaviour as the Poynting vector in the case of vortex light beams. A definition for this quantity will be given later in Section 5.4.3. The probability current coils around the  $z$ -axis, as shown in Figure 3.1.

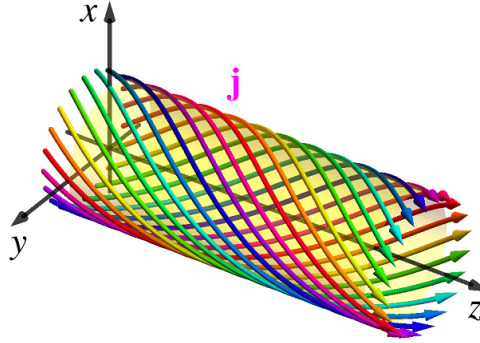


Figure 3.1: The probability current (3.5) vector field is illustrated on a cylindrical surface. Reprinted from [11].

The phase singularity at  $\rho = 0$  is also responsible for a vanishing wavefunction at this point in order to ensure continuity of  $\nabla\psi_T$ . Consequently the probability density also vanishes at the origin of the transverse plane.

More details and properties can be found in the excellent review paper by Bliok et al. [11].

### Radiation from free twisted electron

The probability current (3.5) is twisted in space and might give the impression that some acceleration is involved. From classical electrodynamics it is known that accelerated charges emit radiation and one might expect these wavepackets to radiate. However, the expectation value of the momentum operator is rectilinear and constant in time. Hence, in a semiclassical context, the free twisted electron is not accelerated and does, therefore, not radiate. The same will be true for a full quantum mechanical treatment.

## 3.2 Generation of twisted electrons in experiment

The concept of vortex electron is not only a theoretical construct but has been realized in experiments as well. Two generation schemes, that were already suggested in the first theoretical paper [6], are shown below and more are mentioned in [11].

### 3.2.1 Spiral phase plate

The following method is equivalent to the generation of twisted light beams with spiral phase plates. The propagation of a plane-wave electron beam through a medium adds an additional phase  $\Delta\Phi$  compared to the free space propagation. If the phase plate can be engineered to have a spiral structure such that, depending on the azimuthal angle  $\varphi$ , phase delays of  $[0, 2\pi l]$  can be realized, then an incident plane-wave is transformed to a vortex beam (Figure 3.2). This method was used to experimentally verify the existence of twisted electron beams for the first time [34].

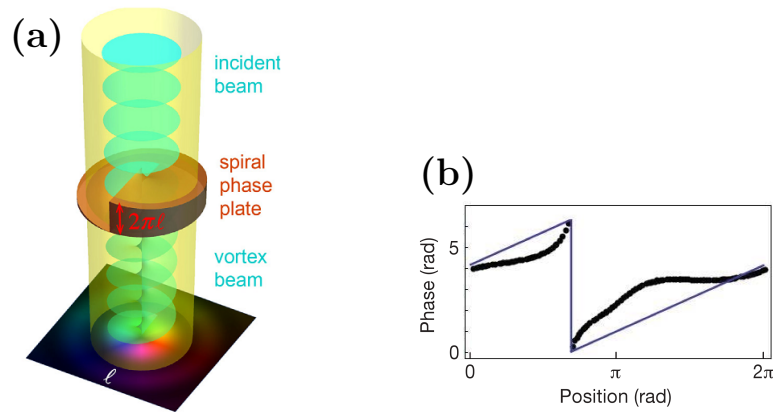


Figure 3.2: The left plot (a) shows a depiction of the transformation of a plane-wave beam to a vortex beam via a spiral phase plate. Reprinted from [11]. The first experimental evidence by means of the measured phase in dependence of the azimuthal angle is shown in the right plot (b). Reprinted from [34].

### 3.2.2 Diffraction grating

The second scheme is also adapted from optics where it has been employed to generate twisted light. The idea behind the mechanism is to generate twisted beams by shining a plane-wave electron onto a structured diffraction grating. A successful implementation has been demonstrated in 2010 [35]. Such a structure is determined from the interference pattern of the incident wavefunction and the target wavefunction. The intensity pattern of a slightly tilted plane-wave and a vortex wavefunction has the form  $\propto [1 + \cos(l\varphi - k_x r \cos \varphi)]$  [11]. It possesses a fork-like pattern and a binarized version can be used to manufacture a grating structure. An illustration is presented in Figure 3.3. The corresponding experimental outcome is shown in Figure 3.4.

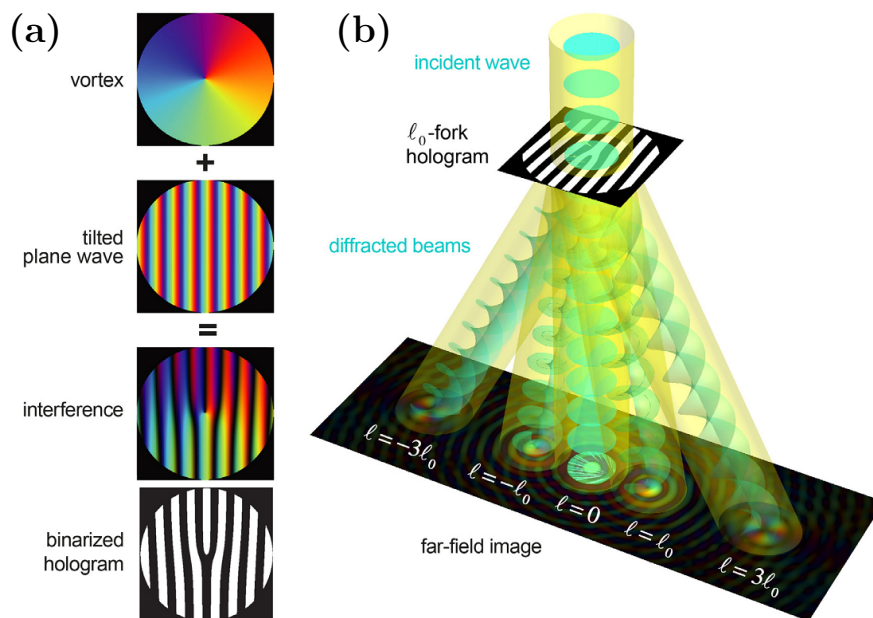


Figure 3.3: (a) The interference pattern of a twisted beam with a tilted plane-wave beam is shown on the left. The binarized form is used for the diffraction grating. (b) The outcome of a plane-wave beam diffracted by this grating is a sum of twisted beams spatially separated depending on their OAM. Reprinted from [11].

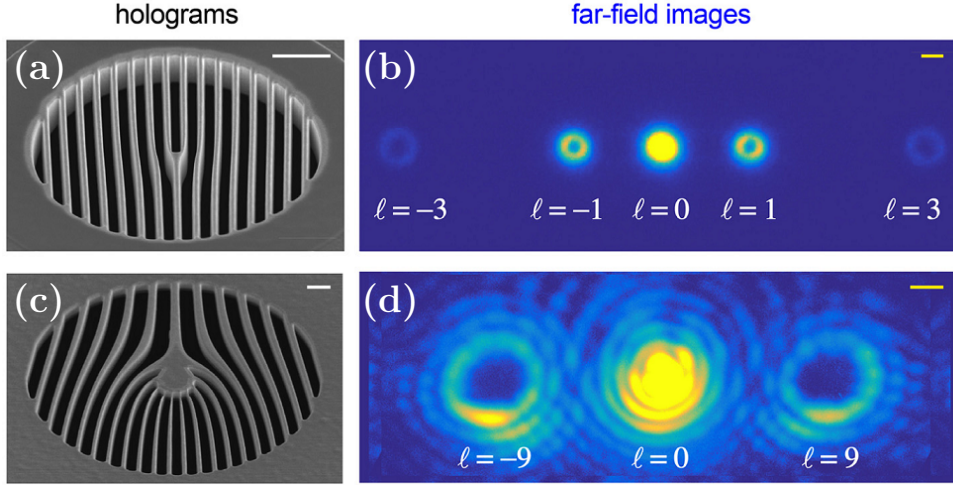


Figure 3.4: The diffraction by a grating allows for a great number of possible outcome shapes. Two viable options are presented. The upper plot corresponds to Figure 3.3 (a) and the outcome modes  $l = 0, \pm 1, \pm 3$  are shown with their intensity distribution (b). A higher order grating shape (c) produces twisted electron beams with larger OAM (d). The lower plots (c), (d) correspond to a production of vortex charge  $l = 9$ . The white scalebars represent  $2 \mu\text{m}$  and the yellow scalebars correspond to  $10 \text{ nm}$  ( $\approx 200$  Bohr radii). Reprinted from [11].

### 3.3 Construction from plane-waves

The wavefunction (3.2) was obtained for the paraxial approximation of the free Schrödinger equation. The question arises if such vortex wavepacket can be constructed from exact solutions, namely the plane-wave momentum eigenfunctions  $\psi_{\vec{p}}(\vec{r})$ . The overlap with a twisted wavepacket

$$\langle \psi_{\vec{p}} | \psi_{\text{T}} \rangle \propto \int d\varphi e^{i\vec{p}\cdot\vec{r}/\hbar} e^{il\varphi} \propto e^{il\phi} \quad (3.6)$$

has a similar characteristic exponential factor but in momentum space  $(p_{\perp}, \phi, p_{\parallel})$  [11]. The integral solution can be found in Appendix B.2. This form allows to construct a general twisted wavepacket that is also a solution of the Schrödinger equation without the need for a paraxial approximation. Additionally, the plane-wave composition makes it possible to construct a finite wavepacket subjected to wavefunction spreading. The mathematical description is further explored here and a solution is sought that fulfills the requirement for a localized and normalizable wavepacket and reduces to a Gaussian wavepacket for  $l = 0$ . We start by assuming a general form for the free twisted wavepacket

$$\psi_{\text{T}} \propto e^{il\varphi} \cdot f(\rho, z) \quad (3.7)$$

in cylindrical coordinates  $(\rho, \varphi, z)$  in position space. As mentioned above, the plane-wave decomposition reveals that the weight in momentum space  $(p_{\perp}, \phi, p_{\parallel})$  has the same exponential factor but with the azimuthal angle in momentum space. Hence, a general form for the weights  $\tilde{\psi}(\vec{p})$  in momentum space is assumed, namely

$$\tilde{\psi}(\vec{p}) = e^{il\phi} f(p_{\parallel}) g(p_{\perp}). \quad (3.8)$$

The twisted wavepacket in position space is constructed by superposition of free plane-waves  $\psi_{\vec{p}}(\vec{r}) \propto \exp [i(\vec{p} \cdot \vec{r} - \vec{r}^2 t/2)/\hbar]$  with the weights (3.8) and reads

$$\psi_{\text{T}}(\vec{r}) \propto \int d^3\vec{p} \tilde{\psi}(\vec{p}) \cdot \psi_{\vec{p}}(\vec{r}) \quad (3.9)$$

$$\propto e^{i\ell\varphi} \cdot \mathcal{FT} \left[ e^{-ip_{\parallel}^2 t/2} f(p_{\parallel}) \right] (z) \cdot \int_0^{\infty} dp_{\perp} p_{\perp} J_l(p_{\perp} \rho) \cdot g(p_{\perp}) e^{-ip_{\perp}^2 t/2} \equiv e^{i\ell\varphi} F(z) G(\rho), \quad (3.10)$$

with new functions  $F$  and  $G$ .  $\mathcal{FT}$  denotes a Fourier transform. The last integral is a Hankel transform of order  $l$ , namely  $\mathcal{H}_l(u) \equiv \int_0^{\infty} dt t J_l(ut) \cdot h(t)$ . It is known that Laguerre-Gaussians (LG)  $\propto (\alpha r)^l e^{-\alpha^2 r^2/2} L_s^l(\alpha^2 r^2)$  are form-invariant under Hankel transforms [36]

$$\int_0^{\infty} dr r (\alpha r)^l J_l(kr) L_s^l(\alpha^2 r^2) e^{-\frac{\alpha^2 r^2}{2}} = (-1)^s \alpha^{-l-2} \left( \frac{k}{\alpha} \right)^l L_s^l \left( \frac{k^2}{\alpha^2} \right) e^{-\frac{k^2}{2\alpha^2}} \quad (l, s \geq 0; l, s \in \mathbb{N}) \quad (3.11)$$

and, hence, allow for a good and simple analytical description of twisted wavepackets. The generalized Laguerre polynomials are denoted by  $L_s^l(x)$ . Without loss of generality, we choose the lowest mode  $L_{s=0}^l(x) = 1$  and utilize the LG function for  $g$ . Similarly, a Gaussian is chosen for  $f$  since it is form-invariant under a Fourier transform. Both choices for  $f$  and  $g$  have the advantage of being localized and vanishing exponentially fast, such that they are square-integrable. The radial part  $G(\rho)$  will then reduce to a normal Gaussian for  $l = 0$ , without the vanishing amplitude at  $\rho = 0$ . Hence, the full wavefunction will reduce to a Gaussian wavepacket in this limit. The weight in momentum space for an arbitrary  $l \in \mathbb{Z}$  reads

$$\tilde{\psi}_{\text{T},\alpha,\beta,\ell}(\vec{p}) \propto e^{i\ell\varphi} \exp \left[ -\frac{\alpha^2 p_{\parallel}^2}{2} \right] p_{\perp}^{|\ell|} \exp \left[ -\frac{\beta^2 p_{\perp}^2}{2} \right] \quad (3.12)$$

and leads to a twisted wavepacket of equal form. An initial momentum in  $z$ -direction can be easily included with  $\tilde{\psi}(\vec{p} - p_0 \vec{e}_z)$ . Having such a decomposition readily available allows to construct a twisted electron wavepacket in a strong laser field with polarization in  $z$ -direction. This is pursued in Chapter 5.





# 4 Model for HHG with Twisted Electrons

Our goal is to give a qualitative description of the high harmonic emission spectrum from atomic systems with vortex electrons. Twisted wavepacket dynamics is inherently three-dimensional and needs to be treated accordingly, since a one-dimensional description is not adequate anymore. In addition, the magnetic field cannot be neglected for intense laser fields [37, 38]. Consequently, magnetic effects will be included with a first order  $1/c$ -expansion of the vector potential [39], additionally to the common dipole approximation. As will be shown in Chapter 5, aforesaid expansion recovers the magnetic field of the full free field expression in the long wavelength limit  $\vec{k} \cdot \vec{r} \ll 1$ . The model Hamiltonian for the atomic system is introduced in Section 4.1. To cope with the complexity of the system and its dynamics, an important approximation of the full wavefunction is stated in Section 4.2, which lies at the heart of this work. Lastly in Section 4.3, the appropriate form of the initial wavefunction is discussed.

## 4.1 Hamiltonian of atomic system

The starting point for our analysis is the Schrödinger equation

$$i\hbar\partial_t\psi(\vec{r},t) = \left[ \frac{(\hat{\vec{p}} - q\vec{A}(\vec{r},t))^2}{2m_e} - \frac{q^2\bar{Z}}{4\pi\epsilon_0 r} \right] \psi(\vec{r},t) \quad (q = -|e|) \quad (4.1)$$

with a Coulomb potential associated with a nucleus of charge  $-q\bar{Z} = \bar{Z}|e|$ . The strong monochromatic laser field  $\vec{A}$  can be described as a classical field with one mode  $\vec{A}(\vec{r},t) = \vec{A}_0(t) \sin(\omega t - \vec{k} \cdot \vec{r})$ , due to the insignificance of quantum effects for vastly populated photonic modes. The prefactor  $\vec{A}_0(t)$  can be a time-varying envelope function, but is taken to be constant and linearly polarized in the  $z$ -direction. The motion of the core will be neglected by virtue of its high inertia compared to the electron ( $m_e \ll m_p$ ). For the remainder of this thesis the atom species is set to be Hydrogen ( $\bar{Z} = 1$ ). The treatment of the magnetic field will be postponed to the next chapter and only the general idea of the model Hamiltonian will be conveyed here. If the typical length scale of the system is shorter than the wavelength of the laser field, the term  $\vec{k} \cdot \vec{r}$  is small and can be treated perturbatively. In zeroth order perturbation, called the dipole approximation  $\vec{A}(\vec{r},t) \approx \vec{A}(t)$ , the Hamiltonian can be recast into its length gauge form

$$i\hbar\partial_t\psi(\vec{r},t) = \left[ \frac{\hat{\vec{p}}^2}{2m} - q\vec{E}(t) \cdot \vec{r} - \frac{q^2}{4\pi\epsilon_0 r} \right] \psi(\vec{r},t). \quad (4.2)$$

This is done via a unitary gauge transformation  $\psi \rightarrow \hat{U}\psi$  with  $\hat{U} = \exp(iq\vec{A}(t) \cdot \vec{r}/\hbar)$ . The spatial dependency of the potential terms show that two distinct regions can be identified, equivalent to the one-dimensional system treated in [29]. In view of this observation we put constraints on the electronic state wavefunction and its dynamics.

## 4.2 Wavefunction splitting

The Coulomb potential will dominate over the laser interaction term for distances close to the origin ( $r \rightarrow 0$ ). On the other hand, for sufficiently large distances,  $r \rightarrow \infty$ , it is the electric field

coupling that exceeds the Coulomb potential, even though it is of long-range nature. Depending on the strength and phase of the field a boundary, at which both potentials equal in magnitude, can be identified. This fact is depicted in Figure 4.1 for a cross section in polarization direction.

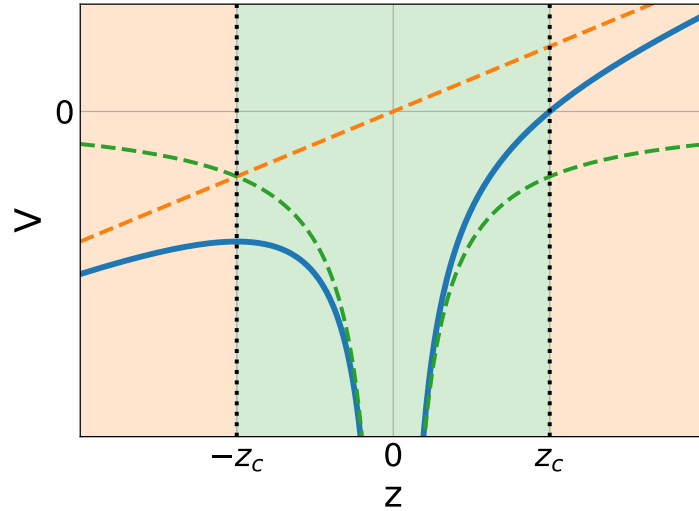


Figure 4.1: For the combination (blue solid line) of Coulomb potential (dashed green line) and laser interaction (dashed orange line) two separate domains emerge in the potential energy landscape of (4.2). The boundary (black dotted lines) lies around the origin and marks the transition from the Coulomb dominated (green filled area) to the laser dominated region (orange filled area).

The classification of regions with dominant interactions suggests a perturbative treatment of the minor potential terms. The simplest approximation is the zeroth order perturbation, in which the smaller terms are neglected. This is of great advantage when the dynamics become separable. Zagoya et al. [40] introduced the concept of Dominant Interaction Hamiltonians for semiclassical trajectories and subdivided the classical phase space accordingly. They investigated HHG dynamics for (2.21) and showed that convergence of the spectrum could be achieved with a total number of trajectories that was two magnitudes smaller than the number needed for propagation under the full potential. Based on this method and the separable dynamics, they were able to calculate an analytical, semiclassical expression for the coefficients of an approximate wavefunction [41], the splitted wavefunction [29] referred to in Section 2.3.1.

The above observations lay ground for the negligible influence of the laser on the quantum mechanical ground state and is one of the assumptions in Lewenstein’s seminal paper [18] mentioned in Section 2.3.1. Additionally, we adopt the conjecture from [18] that only the ground state is important for HHG. If the ionization potential is of similar magnitude than the ponderomotive potential, then it is evident that high-energetic photons in the cutoff region can only be emitted for an electron recombining into the ground state. However, we will estimate the HHG contribution from excited bound states in Chapter 6.

We hypothesize the aforementioned results to hold for the three-dimensional system and approximate the full Hilbert space to be composed of only one free and one bound state. Effectively, this renders the full atomic system a two-level system, namely

$$\boxed{\psi(\vec{r}, t) = c_b(t) \psi_b(\vec{r}, t) + c_T(t) \psi_T(\vec{r}, t)}. \quad (4.3)$$

The twisted electron is then associated with this free part and denoted with a subscript T. Hence, only two Schrödinger equations with reduced Hamiltonians have to be solved. The quantum mechanical solutions of (4.2) for either potential term are exact, namely the Hydrogen eigenstates and Volkov wavefunctions (see Section 5.2).

The issues of this splitting have to be addressed. First, they do not form a complete basis of the Hilbert space and are not even orthogonal, in general. Second, eventually the free Volkov wavepacket will enter the domain of the Coulomb potential to recombine. The validity of using only Volkov solutions breaks down. However, if the mean kinetic energy ( $\propto U_p$ ) of  $\psi_T$  is large upon entering the vicinity of the origin, we expect the region of invalidity to narrow. Third, the exclusion of excited bound states precludes other recombination channels and state transfer from the ground state. The former will be investigated and the latter becomes negligible if the laser frequency  $\omega_0$  is far detuned from the resonance frequency  $(E_1 - E_0)/\hbar$ . Fourth, as shown in Section 2.3.2, the peaks in the HHG spectrum will not be of odd multiple order.

## 4.3 Initial state

The initial conditions for the model at hand still have to be determined. In this work we consider two scenarios in which one takes, at least conceptually, the ionization process into account. This will merely fix the initial coefficients  $c_i(0)$  in (4.3), but corresponds to two distinct physical situations.

### 4.3.1 Ionization process

The usual HHG scenario has an atomic system initially in the ground state and no part of the electronic wavefunction has been ionized before any interaction with the laser field takes place. In order to study HHG with vortex electrons it becomes apparent that the ionized wavefunction must be transformed to a twisted state within the laser pulse length. However, to the best of our knowledge, no such device or potential is available. This presents a serious drawback, but does not prevent us to investigate the HHG spectrum with twisted electrons. We assume that the ionization process and the interaction with this hypothetical potential has already happened. Thus, the initial state is a superposition of the ground state ( $|c_b(0)| \simeq 1$ ) and a small ionized fraction in a twisted state ( $|c_T(0)| \ll 1$ ). This will be referred to as *scenario 1*. The width of the ionized wavepacket is fixed by the laser parameter by means of the ionization rate and is not a free parameter. However, we set it to an arbitrary constant in this work.

### 4.3.2 Laser-assisted scattering

Departing from the traditional approach we include a second, more realistic scenario already mentioned in Sections 2.3.1 [29] and 4.2 [40, 41]. Laser-accelerated electrons ( $c_T(0) = 1$ ) scattered on a positive ion ( $c_b(0) = 0$ ) can show high harmonic emission too. The initial electron momentum is taken to be zero and increases later due to the subsequent acceleration in the laser field. The initial position and the phase of the electric field are tuned to have a vanishing net drift away from the ion, namely  $\vec{A}_0(t) = -A_0\vec{e}_z$  and  $\vec{r} = z_{\max}\vec{e}_z$ . The advantage of this scattering scenario is threefold. First, and most importantly, it does not involve the action of a so far unknown device on the ionized wavefunction. The generation of the twisted electron can happen far away and must not be close to the origin, as in *scenario 1*. Second, the non-recombining fraction of the electron wavefunction, drifting away from the ion, is minimized. If the ionization process is included, then some part of the continuum wavepacket never returns to the parent ion. This can be seen in the numerical simulations in Chapter 7. Third, the width of

the incoming wavepacket represents another available degree of freedom and can be engineered in an unrestricted way, in contrast to *scenario 1*. This connection has not been explored so far and we will designate this approach by *scenario 2* in the following.

The missing element to calculate the dipole acceleration is the analytical description of the twisted electron in the laser field and is derived in the following chapter.

# 5 Twisted Electrons in Strong Laser Field

The general idea of this chapter is to replace the free plane-waves in Section 3.3 with plane-wave Volkov solutions in the superposition. Such Volkov states are exact solutions of a free charged particle moving in a strong, polarized laser field and have the free plane-waves as asymptotic limit for a vanishing field. In general, Volkov wavefunctions are relativistic in nature, but under certain circumstances they can be approximated with a non-relativistic form (Section 5.1). The wavepacket form we seek should fulfill the following limits

$$\text{Twisted electron in laser field} \longrightarrow \begin{cases} \text{Gaussian Volkov wavepacket} & l \rightarrow 0 \\ \text{Free twisted wavepacket} & \vec{A} \rightarrow 0 \\ \text{Free Gaussian wavepacket} & \vec{A} \rightarrow 0, l \rightarrow 0 \end{cases} .$$

First, the appearance of the magnetic field through a Taylor expansion is treated in Section 5.1. The non-relativistic Volkov solutions are introduced in Section 5.2. Finally, the analytical form for the wavefunction is derived in Section 5.3 and its properties are presented in Section 5.4.

## 5.1 First order correction with $1/c$ -expansion

The full-fledged vector potential for an electromagnetic wave in vacuum contains a retardation term  $\omega t - \vec{k} \cdot \vec{r}$  which is of relativistic nature. Such a term causes problems in a non-relativistic theory [42]. Within the dipole approximation this retardation term disappears but the magnetic field  $\vec{B} = \vec{\nabla} \times \vec{A}$  disappears as well. Yet, for sufficiently strong laser fields this contribution becomes important, depending on the velocity ratio  $v/c$  of the electron. The idea to include magnetic fields into the Hamiltonian via a term that is proportional to the inverse speed of light within the dipole approximation was put forward by Reiss in 2000 [39]. He also pointed out the regimes of importance, namely the boundary between a relativistic and a non-relativistic treatment and where the necessity for a magnetic field inclusion occurs (see Figure 5.1).

In 2001 Kylstra et al. [43] showed how an expansion in  $1/c$  of the vector potential includes magnetic field effects and a correction to the electric field within a non-relativistic framework with long laser wavelengths compared to the atomic system size. The correction terms include the magnetic dipole and electric quadrupole interaction [44]. This approach is chosen for this work.

The linearly polarized laser field has the dispersion relation  $c|\vec{k}_0| = \omega_0$ , the propagation direction  $\vec{e}_k$  and the charged particle is assumed to be a spinless electron of mass  $m_e$ . The Schrödinger equation in position representation for  $\vec{A}(\vec{r}, t) = \vec{A}\left(t - \frac{1}{c}(\vec{e}_k \cdot \vec{r})\right)$  and in SI units reads

$$i\hbar\partial_t\psi(\vec{r}, t) = \frac{1}{2m_e} \left[ \hat{\vec{p}} - q\vec{A}\left(t - \frac{1}{c}(\vec{e}_k \cdot \vec{r})\right) \right]^2 \psi(\vec{r}, t). \quad (5.1)$$

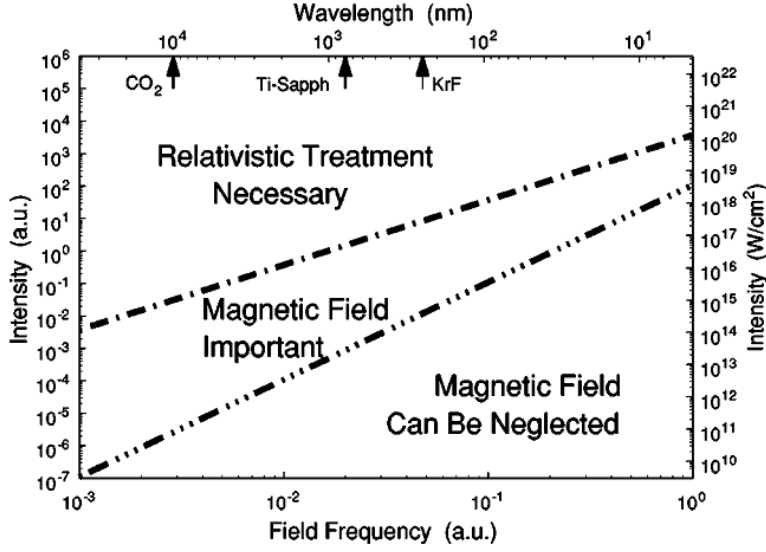


Figure 5.1: The phase space of the two laser parameters, intensity and frequency, is shown in the plot. There is a well-known boundary between relativistic and non-relativistic approaches whenever the velocity approaches the vacuum speed of light. However, an additional intermediate regime exists, requiring magnetic field effects to be included. Reprinted from [39].

We expand the vector potential up to first order in  $1/c$ , i.e.,

$$\vec{A}\left(t - \frac{1}{c}(\vec{e}_k \cdot \vec{r})\right) \approx \vec{A}(t) - \frac{1}{c}(\vec{e}_k \cdot \vec{r}) \underbrace{\frac{d}{dt}\vec{A}(t)}_{=-\vec{E}(t)} \quad (5.2a)$$

$$= \vec{A}(t) + \frac{1}{c}(\vec{e}_k \cdot \vec{r})\vec{E}(t). \quad (5.2b)$$

The resulting electric and magnetic field can be expressed as

$$\vec{E}(\vec{r}, t) = -\partial_t \vec{A}(\vec{r}, t) = \left(1 - \frac{\vec{e}_k \cdot \vec{r}}{c} \partial_t\right) \vec{E}(t), \quad (5.3)$$

$$\vec{B}(\vec{r}, t) = \vec{\nabla} \times \vec{A}(\vec{r}, t) = \frac{\vec{e}_k \times \vec{E}(t)}{c} = \vec{B}(t). \quad (5.4)$$

We expand the square brackets in the Hamiltonian (5.1) and neglect terms proportional to  $\mathcal{O}(c^{-2})$ . Furthermore, we employ the Coulomb gauge ( $\vec{\nabla} \cdot \vec{A} = 0 \Rightarrow \vec{e}_k \cdot \vec{A} = 0$ ). Within this gauge the commutator

$$\left[ \left( \vec{A}(t) \cdot \hat{\vec{p}} \right), \left( \vec{e}_k \cdot \hat{\vec{r}} \right) \right] = 0 \quad (5.5)$$

vanishes. The approximate non-relativistic Hamiltonian in velocity gauge reads

$$\hat{H} = \frac{1}{2m_e} \left\{ \hat{\vec{p}}^2 - 2q\vec{A}(t) \cdot \hat{\vec{p}} + q^2 \vec{A}^2(t) + \frac{2}{c}(\vec{e}_k \cdot \hat{\vec{r}}) \left[ q \left( \frac{d}{dt} \vec{A}(t) \right) \cdot \hat{\vec{p}} - \frac{q^2}{2} \frac{d}{dt} \vec{A}^2(t) \right] \right\}. \quad (5.6)$$

In order to make the wavefunction splitting approximation the Schrödinger equation will be transformed to the length gauge (L) with the gauge transformation

$$\psi(\vec{r}, t) = U_L(\vec{r}) \psi_L(\vec{r}, t) = \exp(iq\vec{A}(t) \cdot \vec{r}/\hbar) \psi_L(\vec{r}, t). \quad (5.7)$$

Physically speaking we perform a transformation to a non-inertial frame with momentum  $q\vec{A}(t)$ . The partial derivatives of the wavefunction are

$$i\hbar\partial_t U_L(\vec{r})\psi_L(\vec{r}, t) = U_L(\vec{r}) \left( i\hbar\partial_t - q\dot{\vec{A}}(t) \cdot \vec{r} \right) \psi_L(\vec{r}, t), \quad (5.8)$$

$$\hat{\vec{p}} U_L(\vec{r})\psi_L(\vec{r}, t) = U_L(\vec{r}) \left( \hat{\vec{p}} + q\vec{A}(t) \right) \psi_L(\vec{r}, t), \quad (5.9)$$

$$\hat{\vec{p}}^2 U_L(\vec{r})\psi_L(\vec{r}, t) = U_L(\vec{r}) \left( \hat{\vec{p}}^2 + 2q\vec{A}(t) \cdot \hat{\vec{p}} + q^2\vec{A}^2(t) \right) \psi_L(\vec{r}, t). \quad (5.10)$$

The transformed Schrödinger equation in length gauge reads

$$\boxed{i\hbar\partial_t\psi_L(\vec{r}, t) = \left\{ \frac{\hat{\vec{p}}^2}{2m_e} - q\vec{E}(t) \cdot \left[ \vec{r} + \frac{(\vec{e}_k \cdot \vec{r})}{m_e c} \hat{\vec{p}} \right] \right\} \psi_L(\vec{r}, t).} \quad (5.11)$$

To obtain the length gauge solutions the Schrödinger equation in velocity gauge (5.6) is solved first and transformed with the inverse transformation  $\psi_L = U_L^\dagger\psi$  afterwards. The solutions are referred to as “non-relativistic Volkov wavefunctions” and reduce to free plane-wave functions in the limit  $\vec{A} \rightarrow 0$ . As Reiss criticizes in his paper [45], these solutions cannot be physical since the long wavelength approximation is only valid in a small region of space, but plane-waves extend infinite in space. He argues that this is only justified if a transition element with a bound state is calculated. These states are spatially confined and, hence, the transition element probes only the bound region. Further below finite twisted wavepackets will be constructed from these plane-wave solution, similar to Gaussian wavepackets constructed from free plane-wave solutions. They extend also over a finite region of space justifying the approximation.

## 5.2 Plane-wave Volkov solutions

The derivation for the solutions of the Schrödinger equation (5.11) can be found in Appendix B.1. The plane-wave Volkov eigenfunctions with first-order correction in length gauge are given by

$$\psi_{L,\vec{p}}(\vec{r}, t) \propto \exp \left[ \frac{i}{\hbar} \left( \vec{\pi}(t) \cdot \vec{r} - \int_{t_0}^t dt' \frac{\vec{\pi}^2(t')}{2m_e} \right) \right]. \quad (5.12)$$

The kinetic momentum is defined as  $\vec{\pi}(t) = \vec{p} - q\vec{A} - \frac{\vec{e}_k}{m_e c} (q\vec{A}(t) \cdot \vec{p} - \frac{q^2}{2}\vec{A}^2(t))$ . They reduce to the usual non-relativistic Volkov wavefunctions in the limit of  $v/c \rightarrow 0$  ( $v \equiv |\vec{p}|/m_e$ ). Furthermore, for  $\vec{A}(t) \rightarrow 0$  the simple free plane-wavefunctions are recovered. Note also that these states are orthogonal. We expand the exponent in order to calculate a superposition with weights  $\tilde{\psi}(\vec{p})$  and neglect terms proportional to  $\mathcal{O}(c^{-2})$ . Then Equation (5.12) reads

$$\begin{aligned} \psi_{L,\vec{p}}(\vec{r}, t) \propto \exp \left[ \frac{i}{\hbar} \left\{ -q\vec{A}(t) \cdot \vec{r} + \vec{p} \cdot \left( \vec{r} - \vec{r}_{\omega_0}(t) \left[ 1 + \frac{\vec{e}_k \cdot \vec{p}}{m_e c} \right] - \frac{\vec{e}_k \cdot \vec{r}}{m_e c} q\vec{A}(t) \right) \right\} \right] \times \\ \exp \left[ \frac{i}{\hbar} \left\{ -\frac{\vec{p}^2}{2m_e} t - S_{\omega_0}(t) \left[ 1 + \frac{\vec{e}_k \cdot \vec{p}}{m_e c} \right] + \frac{\vec{e}_k \cdot \vec{r}}{m_e c} \frac{q^2}{2} \vec{A}^2(t) \right\} \right]. \end{aligned} \quad (5.13)$$

The new definitions

$$\vec{r}_{\omega_0}(t) \equiv -\frac{q}{m_e} \int_{t_0}^t dt' \vec{A}(t'), \quad S_{\omega_0}(t) \equiv \frac{q^2}{2m_e} \int_{t_0}^t dt' \vec{A}^2(t') \geq 0 \quad (5.14)$$

were introduced with dimensions of length and action, respectively. The subscript provides the connection to the laser frequency  $\omega_0$ . The variable  $\vec{r}_{\omega_0}(t)$  corresponds to the classical trajectory

of a charged point particle under the influence of the vector potential  $\vec{A}(t)$ . By inserting the specifications from Chapter 4 the integrations can be carried out and give the expressions

$$\vec{r}_{\omega_0}(t) = -\underbrace{\frac{qA_0}{m_e\omega_0}}_{\equiv z_{\max}} \cos(\omega_0 t) \quad \text{and} \quad S_{\omega_0}(t) = U_p \left( t - \frac{\sin(2\omega_0 t)}{2\omega_0} \right). \quad (5.15)$$

An initial displacement of the center of the wavepacket in  $z$ -direction was included in the definition of  $\vec{r}_{\omega_0}(t)$ .

### 5.3 Twisted wavepacket

The construction of twisted, localized wavepackets can be obtained with a superposition of plane-waves with weights  $\tilde{\psi}(\vec{p}) \propto e^{il\phi}$  and was presented in Section 3.3. Two choices for this superposition stand out in theoretical research of twisted wavepackets. The first uses a single component of the radial momentum  $\delta(p_{\perp} - p_{\perp_0})$  and leads to single Bessel functions for the radial component of the wavefunction, see, for example, references [46, 47, 48]. Due to the singular nature of the radial momentum it is impossible to normalize these wavefunctions in free space and render them unphysical (see Figure 5.2). An additional consequence is the absence of transverse dispersion. A more physical choice can be understood as a superposition of Bessel wavefunctions, i.e., a distribution of radial momentum components with finite width. A natural choice are solutions of Laguerre-Gaussian type which have been used, for example, in references [6, 49, 50, 51]. Moreover, they are subject to the usual wavefunction dispersion. Thus, the latter approach is chosen for this work with a weight function

$$\tilde{\psi}_{\Gamma, \alpha, \beta, l}(\vec{p}) \propto \frac{e^{il\phi}}{2\pi i^l} \exp\left[-\frac{\alpha^2 p_{\parallel}^2}{2\hbar^2}\right] p_{\perp}^l \exp\left[-\frac{\beta^2 p_{\perp}^2}{2\hbar^2}\right] \quad (5.16)$$

analogous to equation (3.12).

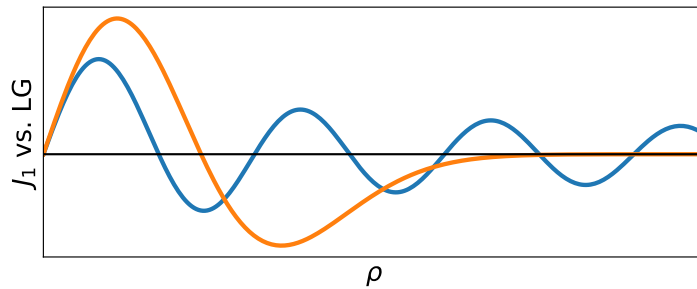


Figure 5.2: The Bessel function of order one (blue) and a Laguerre-Gaussian (orange) with two extrema are shown for arbitrary units. The Bessel function does not decay exponentially like the LG mode and is not normalizable.

It is given in cylindrical coordinates in momentum space  $(p_{\perp}, \phi, p_{\parallel})$  and  $\alpha, \beta \in \mathbb{R}$ ,  $l \in \mathbb{N}$  are free parameters. For simplicity, we set  $s = 0$  ( $L_0^{||l}(x) = 1$ ) in Equation (3.11) because a non-zero value would lead to a multiple ring structure in the transverse plane. For the case at hand, an analytical result would be possible for  $s \neq 0$  as well. Selecting the lowest mode does not change the physics and might be the best choice to have the largest overlap with the hydrogen ground state wavefunction. Another assumption, but no constraint in general, is the positivity of  $l \geq 0$ .



The normalization is not important for now and will be done for the fully constructed twisted wavepacket

$$\psi_{\text{T}}(\vec{r}, t) = \int d^3\vec{p} \tilde{\psi}_{\alpha,\beta,l}(\vec{p}) \psi_{L,\vec{p}}(\vec{r}, t). \quad (5.17)$$

We assume the electric field polarization and the quantization axis of the orbital angular momentum to be collinear in  $z$ -direction and the laser field to propagate in  $y$ -direction, namely

$$\vec{A}(t) = A(t)\vec{e}_z, \quad \vec{r}_{\omega_0}(t) = r_{\omega_0}(t)\vec{e}_z, \quad \vec{e}_k = \vec{e}_y. \quad (5.18)$$

The interaction of relativistic vortex electrons with a few-cycle laser pulse in a “head-on” collision scenario ( $\vec{e}_z = \vec{e}_k$ ) has been explored in [52]. Other configurations are possible but yield very complex equations and we refrain from trying to derive any analytical results. These cases are suitable for numerical integrations. The full integration and the approximations used, including their limitations, can be found in Appendix B.3. The analytical form for a twisted electron wavepacket in a strong laser field with collinear quantization axes reads

$$\boxed{\psi_{\text{T}}^{(c)}(\vec{r}, t) = [1 + F(\vec{r}, t)]\Omega(\varphi)Z(z, t)\Xi(\rho, t) = [1 + F(\vec{r}, t)]\psi_{\text{T}}(\vec{r}, t).} \quad (5.19)$$

and includes the definitions

$$\Omega(\varphi) \equiv \frac{1}{\sqrt{2\pi}} e^{i\ell\varphi}, \quad (5.20)$$

$$Z(z, t) \equiv \frac{1}{\pi^{1/4}\sqrt{\sigma_\alpha(t)}} \exp\left[\frac{i}{\hbar}\left(-qA(t)z - S_{\omega_0}(t)\right)\right] \exp\left[-\frac{(z - r_{\omega_0}(t))^2}{2\sigma_\alpha^2(t)} \cdot (1 - i\tau_\alpha(t))\right], \quad (5.21)$$

$$\Xi(\rho, t) \equiv \sqrt{\frac{2}{l!}} \frac{\rho^l}{\sigma_\beta^{l+1}(t)} \exp\left[-\frac{\rho^2}{2\sigma_\beta^2(t)} \cdot (1 - i\tau_\beta(t))\right], \quad (5.22)$$

$$\tau_j(t) \equiv \frac{\hbar t}{m_e j^2} \quad \text{for } j = \{\alpha, \beta\}, \quad (5.23)$$

$$\sigma_j(t) \equiv j \cdot \sqrt{1 + \tau_j^2(t)} \quad \text{for } j = \{\alpha, \beta\}. \quad (5.24)$$

The superscript (c) stands for the inclusion of  $1/c$ -corrections. The correction term  $F \propto \mathcal{O}(c^{-1})$  is proportional to the inverse speed of light and its definition can be found in the Appendix B.3 as well. The  $\tau$  variables represent the dimensionless time scale of diffusion and the  $\sigma$ 's are the time-dependent widths of the wavepacket. The prefactors are chosen to be

$$\int_0^{2\pi} d\varphi |\Omega(\varphi)|^2 = 1, \quad \int_{-\infty}^{\infty} dz |Z(z, t)|^2 = 1, \quad \int_0^{\infty} d\rho \rho |\Xi(\rho, t)|^2 = 1, \quad (5.25)$$

such that each main component is normalized to one. For  $l \neq 0$  the vortex wavepacket has a ring structure in the  $x$ - $y$ -plane with a peak amplitude at  $\rho_{\text{ring}}(t) = \sqrt{l} \cdot \sigma_\beta(t)$  (Figure 5.3).

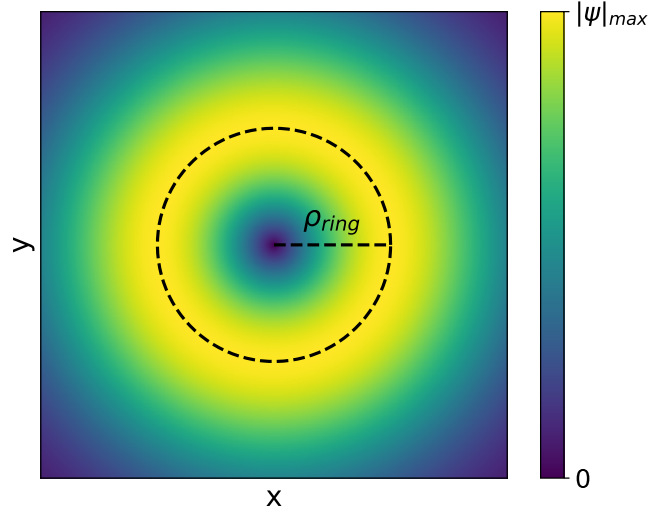


Figure 5.3: The transverse cross section of the modulus of a twisted wavepacket shows a ring structure and vanishing probability density at  $\rho = 0$ .

## 5.4 Properties

In order to understand the HHG dynamics it is important to study the properties of the wavepacket (5.19) presented above.

### 5.4.1 Orbital Angular Momentum

In free space, twisted wavepackets are eigenfunctions of the  $z$ -component of the angular momentum operator. The influence of the electric and the magnetic field on the orbital angular momentum will be derived below. The expectation value reads

$$\langle \hat{L}_z \rangle = \langle \psi_T^{(c)} | \hat{L}_z | \psi_T^{(c)} \rangle = \langle \psi_T | \underbrace{\hat{L}_z}_{=l\hbar} | \psi_T \rangle + 2\Re \langle \psi_T | \hat{F} \underbrace{\hat{L}_z}_{=l\hbar} | \psi_T \rangle + \mathcal{O}(c^{-2}) \quad (5.26)$$

$$= l\hbar + l\hbar \cdot 2\Re \underbrace{\langle \psi_T | \hat{F} | \psi_T \rangle}_{=0} \quad (5.27)$$

$$= l\hbar. \quad (5.28)$$

As expected, due to the collinearity of the quantization and polarization axis of the electric field, the wavepacket is an eigenfunction in the dipole approximation. Surprisingly, the OAM is unchanged under the perturbative influence of the magnetic field. This is ensured by the orthogonality of the correction part  $\hat{F}|\psi_T\rangle$  and  $|\psi_T\rangle$  (see Appendix B.3). The wavepacket is merely shifted in the direction of the laser propagation, see Section 5.4.2. The physical reason is the orthogonality of the magnetic field polarization and the quantization axis of the electron OAM. If the magnetic field has a nonzero collinear component in  $z$ -direction, then a change in the orbital angular momentum would occur as a result of the Lorentz force. It can be understood as an effect similar to Landau eigenstates, which have a similar structure to free space vortex wavepacket, primarily the factor  $e^{im_{\text{Landau}}\varphi}$ . A pictorial representation is shown in Figure 5.4 and an extensive study of the dynamics of twisted electrons in magnetic fields can be found in reference [53]. Additionally, the dipole approximation form  $|\psi_T\rangle$  is orthogonal to any other OAM eigenstate with a different orbital angular momentum. For example, every twisted state with  $l \neq 0$  is orthogonal to the Hydrogen ground state.

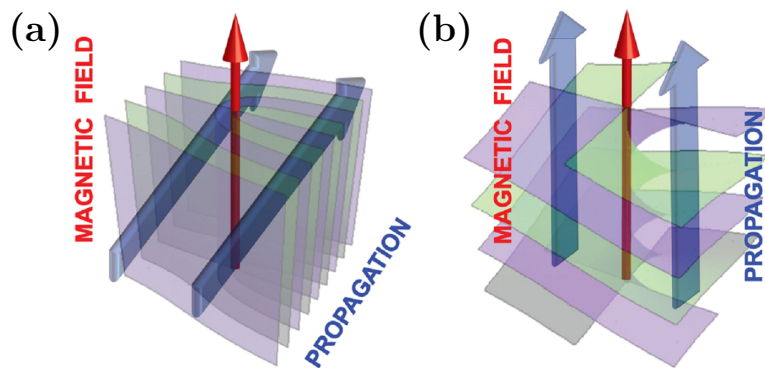


Figure 5.4: The induced changes on plane-wavefunctions depending on the propagation direction relative to the magnetic field direction are shown for an isolated magnetic flux line. The left side (a) shows a propagation orthogonal to the magnetic field and the wavepacket experiences a wavefront dislocation in the direction orthogonal to the magnetic field and the propagation direction. (b) On the contrary, a propagation along the flux line induces a screw dislocation of the wavefront, leading to vortex character. Reprinted from [53].

### 5.4.2 Classical correspondence

The classical dynamics within the  $1/c$ -perturbation shall be explored here and will be compared to the motion of the wavepacket center. We shall, again, make use of the correspondence principle between quantum mechanics and classical mechanics, e.g.,  $\hat{r} \rightarrow \vec{r}$  and  $\hat{p} \rightarrow \vec{p}$ . The classical Hamiltonian is

$$H_{\text{cl}} = \frac{\vec{p}^2}{2m} + q\dot{A}(t) \cdot \left[ \vec{r} + \frac{1}{m_e c} (\vec{e}_k \cdot \vec{r}) \vec{p} \right] = H_0 + V_L. \quad (5.29)$$

The charged particle moves under the force field

$$-\nabla V_L = -q\dot{A}(t) - \frac{q}{m_e c} \left( \dot{A}(t) \cdot \vec{p} \right) \vec{e}_k \quad (5.30)$$

and Hamilton's equation of motions [54] determine the dynamics. The coordinate system is fixed corresponding to equation (5.18) and we assume  $A(t_0) = 0$ . The solution for the momentum vector is

$$\dot{\vec{p}} = -\frac{\partial H_{\text{cl}}}{\partial \vec{r}} = -q\dot{A}(t)\vec{e}_z - \frac{q}{m_e c} \dot{A}(t)p_z \vec{e}_y, \quad (5.31)$$

$$\Rightarrow p_z(t) = p_z(t_0) - qA(t), \quad (5.32)$$

$$\dot{p}_y(t) = \frac{q^2}{2m_e c} \frac{d}{dt} A^2(t) \quad \Rightarrow \quad p_y(t) = p_y(t_0) + \frac{q^2}{2m_e c} A^2(t), \quad (5.33)$$

and we assume that there is no motion in the  $x$ -direction, i.e.,  $p_x(t) = 0$ ,  $x(t) = \text{const}$ . For the position of the classical particle follows

$$\dot{\vec{r}}_{\text{cl}} = \frac{\partial H_{\text{cl}}}{\partial \vec{p}} = \frac{1}{m_e} \vec{p} + \frac{qy_{\text{cl}}(t)}{m_e c} \dot{A}(t) \vec{e}_z, \quad (5.34)$$

$$\Rightarrow y_{\text{cl}}(t) = y_{\text{cl}}(t_0) + \frac{p_y(t_0)}{m_e} (t - t_0) + \frac{q^2}{2m_e^2 c} \int_{t_0}^t dt' A^2(t') = \frac{S_{\omega_0}(t)}{m_e c} + \frac{p_y(t_0)}{m_e} (t - t_0), \quad (5.35)$$

$$\Rightarrow z_{\text{cl}}(t) = z_{\text{cl}}(t_0) + \frac{p_z(t_0)}{m_e} (t - t_0) - \frac{q}{m_e} \int_{t_0}^t dt' A(t') + \mathcal{O}(c^{-2}). \quad (5.36)$$

The non-uniform dynamics occurs only in the  $y$ - $z$ -plane. To compare the dynamics with the quantum wavepacket we assume the same initial parameters, namely  $t_0 = 0$ ,  $y_{\text{cl}}(0) = 0$ ,  $p_z(0) = 0$ ,  $z_{\text{cl}}(0) = z_{\text{max}}$  and the vector potential  $A(t) = -A_0 \sin(\omega_0 t)$ , leading to

$$\Rightarrow \quad z_{\text{cl}}(t) = r_{\omega_0}(t), \quad y_{\text{cl}}(t) = \frac{S_{\omega_0}(t)}{m_e c}. \quad (5.37)$$

This shows that there is a linear motion in  $y$ -direction away from the origin superimposed by a sinusoidal motion with twice the laser frequency, see Equation (5.15). If we were to assume a counter-acting initial momentum  $p_y(0) = -U_p/c$  in  $y$ -direction to cancel the linear motion, the prominent ‘‘Figure-8’’ motion would emerge [55]. The dynamics for both cases is depicted in Figure 5.5.

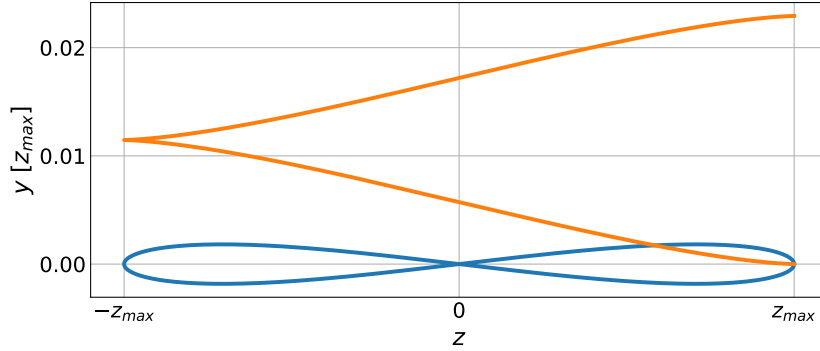


Figure 5.5: The classical motion (5.37) is shown as the orange line in units of the quiver amplitude  $z_{\text{max}}$ . The blue lines corresponds to a finite initial momentum in  $y$ -direction to cancel the linear motion in transverse direction.

The comparison with the expectation value of the position operator  $\langle \vec{r} \rangle = \int dV \vec{r} |\psi|^2$  shows that the bulk motion of the wavepacket equals the classical trajectory

$$\langle x \rangle = 0, \quad \langle y \rangle = \frac{S_{\omega_0}(t)}{m_e c}, \quad \langle z \rangle = r_{\omega_0}(t), \quad (5.38)$$

as expected from the Ehrenfest theorem for potentials with linear or quadratic dependence.

### 5.4.3 Probability current

The probability current of a wavefunction is defined [56] as

$$\vec{j}(\vec{r}, t) \equiv \frac{1}{2m_e} \left[ \psi^*(\vec{r}, t) \hat{p} \psi(\vec{r}, t) - \psi(\vec{r}, t) \hat{p} \psi^*(\vec{r}, t) \right] \quad (5.39)$$

Due to the results of Sections 5.4.1 and 5.4.2, respectively, only the dipole approximation form  $\psi_{\text{T}}(\vec{r}, t)$  is used to calculate the current. The two terms are given by

$$\psi_{\text{T}}^* \hat{p} \psi_{\text{T}} = |\psi_{\text{T}}|^2 \left[ \vec{e}_z \left( -qA + i\hbar \frac{z - r_{\omega_0}}{\sigma_\alpha} (1 - i\tau_\alpha) \right) + \vec{e}_\varphi \frac{\hbar l}{\rho} + \vec{e}_\rho \left( -i \frac{\hbar l}{\rho} + i\hbar \frac{\rho}{\sigma_\beta} (1 - i\tau_\beta) \right) \right], \quad (5.40)$$

$$\psi_{\text{T}} \hat{p} \psi_{\text{T}}^* = |\psi_{\text{T}}|^2 \left[ \vec{e}_z \left( qA + i\hbar \frac{z - r_{\omega_0}}{\sigma_\alpha} (1 + i\tau_\alpha) \right) - \vec{e}_\varphi \cdot \frac{\hbar l}{\rho} + \vec{e}_\rho \left( -i \frac{\hbar l}{\rho} + i\hbar \frac{\rho}{\sigma_\beta} (1 + i\tau_\beta) \right) \right] \quad (5.41)$$

and yield the final expression

$$\vec{j}_T \equiv \frac{|\psi_T|^2}{m_e} \left[ \underbrace{-qA \cdot \vec{e}_z}_{\text{laser}} + \underbrace{\frac{\hbar l}{\rho} \cdot \vec{e}_\varphi}_{\text{twist}} + \underbrace{\frac{(z - r_{\omega_0}) \cdot \hbar \tau_\alpha}{\sigma_\alpha} \cdot \vec{e}_z + \frac{\rho \cdot \hbar \tau_\beta}{\sigma_\beta} \cdot \vec{e}_\rho}_{\text{diffusion}} \right], \quad (5.42)$$

revealing the different current sources. Additionally, the expectation value of the momentum operator

$$\langle \psi_T(t) | \hat{p} | \psi_T(t) \rangle = -qA(t) \vec{e}_z \quad (5.43)$$

follows easily from equation (5.40) and shows only a motion in the polarization direction of the electric field.

## 5.5 Laser and model parameters

Unless stated otherwise, we will use two parameter settings in this thesis. The first one has a quiver amplitude  $z_{\max}$  larger than the twisted wavepacket extension  $\sigma_\alpha(t)$ . Hence, the bound and free part are always well separated for  $r_{\omega_0}(t) = z_{\max}$ . In Chapter 7 we investigate the dynamics with a full three-dimensional quantum simulation with a split-operator method. In order to keep the computational effort at an acceptable level the necessary number of discrete grid points should be minimized. Therefore, a second setting is chosen with a smaller extension and a slightly shorter time scale. However, the separation between both parts of the wavefunction is less than for the first parameter set. A comparative depiction is shown in Figure 5.6 and the numerical parameter values are presented in Table 5.1.

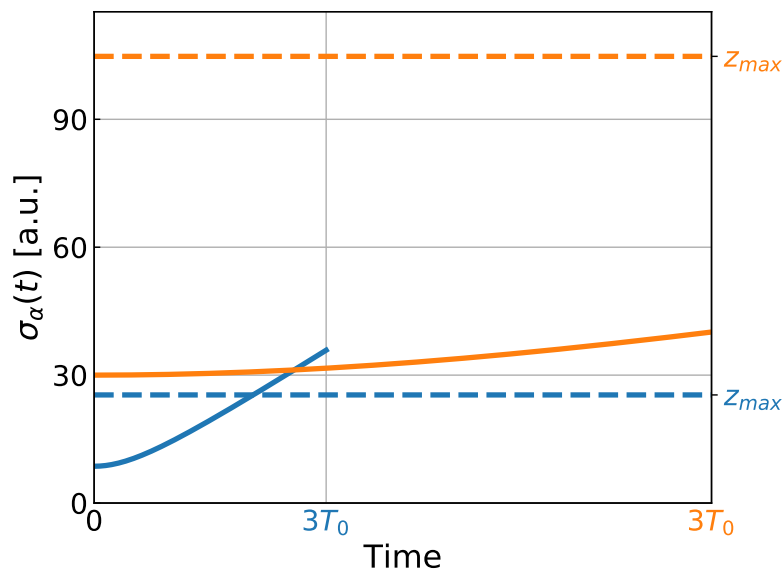


Figure 5.6: The wavepacket extension  $\sigma_\alpha(t)$  over a pulse length of three laser periods  $T_0$  is shown for the two parameter settings in Table 5.1. Setting 1 is shown in orange and setting 2 in blue. The dashed lines indicate the maximal quiver amplitude due to the electric field. While the width is always smaller than the quiver amplitude in setting 1, there is a crossing for setting 2.

| Setting | $E_0$ [a.u.] | $\omega_0$ [a.u.]         | $\alpha$ [a.u.] | $I_p$ [a.u.] | $U_p$ [a.u.] | $(I_p + 2U_p)/(\hbar\omega_0)$ |
|---------|--------------|---------------------------|-----------------|--------------|--------------|--------------------------------|
| 1       | 0.05835      | 0.0236                    | 30.0            | 0.5          | 1.528        | 150.7                          |
| 2       | 0.1          | $2\pi/100 \approx 0.0628$ | 8.627           | 0.47         | 0.634        | 27.7                           |

Table 5.1: Two parameter settings, given in atomic units (Appendix C.1), are used to analyze the HHG spectrum. Setting 2 has a slightly lower ionization potential  $I_p$  due to a smoothed Coulomb potential in the quantum simulation (see Section 7.2.1).

# 6 Analytical Results

The dipole acceleration for the effective two-level system can be analytically derived. The free part of the wavefunction is approximated with the twisted wavepacket constructed in Chapter 5 and the analytical form for the bound states of Hydrogen are briefly introduced in Section 6.1. The actual calculation can be found in Section 6.2 and, finally, we will give an analytic approximation for the associated spectrum of the dipole acceleration in Section 6.3.

## 6.1 Hydrogen atom

The bound states are taken to be eigenstates of Hydrogen ( $\bar{Z} = 1$ ), neglecting the influence of the laser field which is expected to be weak around the origin. The eigenstates in spherical coordinates are [56]

$$\psi_{nlm}(\vec{r}, t) = R_{nl}(r)Y_l^m(\theta, \varphi) = C_{nlm}e^{im\varphi}P_l^m(\cos\theta)\left(\frac{2r}{na_0}\right)^l e^{-r/na_0}L_{n-l-1}^{2l+1}\left(\frac{2r}{na_0}\right)e^{-iE_n t/\hbar} \quad (6.1)$$

with eigenenergies

$$E_n = -\frac{\hbar^2}{2m_e a_0^2 n^2} \equiv -\frac{I_p}{n^2} \equiv -I_{p,n}. \quad (6.2)$$

The normalization constant is given by

$$C_{nlm} = \sqrt{\frac{(2l+1)(n-l-1)!(l-m)!}{\pi n^4 a_0^3 (n+l)!(l+m)!}} \quad (6.3)$$

with ground state ionization energy  $I_p > 0$  and the Bohr radius  $a_0 = \frac{4\pi\epsilon_0\hbar^2}{m_e e^2}$ . Furthermore,  $P_l^m(x)$  denotes the associated Legendre polynomials and  $L_l^m(x)$  denotes the associated Laguerre polynomials

$$P_l^m(\mu) = (-1)^m \frac{(1-\mu^2)^{m/2}}{2^l l!} \frac{d^{l+m}}{d\mu^{l+m}} (\mu^2 - 1)^l = (-1)^{m+l} \frac{(1-\mu^2)^{m/2}}{2^l l!} \frac{d^{l+m}}{d\mu^{l+m}} (1-\mu^2)^l, \quad (6.4)$$

$$P_l^{-m}(\mu) = (-1)^m \frac{(l-m)!}{(l+m)!} P_l^m(\mu), \quad (6.5)$$

$$L_l^m(\mu) = \frac{e^\mu \mu^{-m}}{l!} \frac{d^l}{d\mu^l} (\mu^{m+l} e^{-\mu}). \quad (6.6)$$

To distinguish the vortex charge and the quantum number  $l$ , the latter will be primed from now on, i.e.,  $l'$ . The validity of neglecting the laser interaction becomes less justified for higher excited states with higher quantum number  $n$ , since the extension of the state increases with  $n$ . Hence, the influence of the laser will be stronger in the outer regions for these states.

## 6.2 Dipole acceleration

In Section 2.2 we motivated the use of the expectation value of the dipole acceleration to study the emission spectrum. In the following the dipole acceleration form (2.20) is used in combination

with the wavefunction splitting (4.3). Even though the full wavefunction  $\psi_{\text{T}}^{(c)}$  is readily available we focus only on the dipole approximation  $\psi_{\text{T}}$  in this section and investigate the effects of the correction term numerically in Section 7. The derivation of the first order perturbation terms is lengthy and tedious, but can be calculated without additional assumptions or approximations. A further important point to make is that we restrict ourselves to central collisions for the analytical derivation. However, we will address off-axis scattering numerically in Chapter 7. The potential in length gauge is

$$\hat{V} = -q\vec{E} \cdot \hat{\vec{r}} - \frac{q^2}{4\pi\epsilon_0\hat{r}}. \quad (6.7)$$

In the fixed coordinate system (5.18) the dipole acceleration reads

$$\boxed{\vec{a}(t) = \ddot{\vec{d}}(t) = -\frac{q}{m_e} \left[ -qE(t)\vec{e}_z + \frac{q^2}{4\pi\epsilon_0} \cdot \langle \psi(t) | \frac{\hat{\vec{r}}}{\hat{r}^3} | \psi(t) \rangle \right]}. \quad (6.8)$$

Henceforth we will neglect the first term since it gives only one dominant peak at the laser frequency  $\omega_0$  in the emission spectrum. In order to be able to derive analytical results the initial widths of the twisted wavepacket in (5.19)

$$\boxed{\beta = \alpha} \quad \Rightarrow \quad \boxed{\tau_\alpha = \tau_\beta \equiv \tau} \quad \boxed{\sigma_\alpha = \sigma_\beta \equiv \sigma} \quad (6.9)$$

are set to be equal. Due to the spherical symmetry of the Coulomb eigenfunctions it is useful to work in spherical coordinates. For completeness, we give the twisted wavepacket in the coordinates  $(r, \varphi, u = \cos \theta)$ . It is

$$\psi_{\text{T}}(\vec{r}, t) = \mathcal{N}_{\text{T}}(t) \left( r\sqrt{1-u^2} \right)^l e^{il\varphi} e^{-\frac{i}{\hbar}S\omega_0(t)} e^{-\frac{i}{\hbar}qA(t)ru} e^{-\frac{1-i\tau(t)}{2\sigma^2(t)} \cdot (r^2+r\omega_0^2(t)-2rur\omega_0(t))}. \quad (6.10)$$

The normalization constant is given by  $\mathcal{N}_{\text{T}}(t) = \left( \pi^{1/4} \sqrt{l! \pi \sigma(t)} \sigma^{l+1}(t) \right)^{-1}$ .

### 6.2.1 Coulomb force term

In order to analyze different emission contributions the wavefunction (4.3) is plugged into the dipole acceleration equation (6.8) and gives

$$\langle \psi | \frac{\hat{\vec{r}}}{\hat{r}^3} | \psi \rangle = |c_b|^2 \underbrace{\langle \psi_b | \frac{\hat{\vec{r}}}{\hat{r}^3} | \psi_b \rangle}_{\equiv(BB)} + |c_{\text{T}}|^2 \underbrace{\langle \psi_{\text{T}} | \frac{\hat{\vec{r}}}{\hat{r}^3} | \psi_{\text{T}} \rangle}_{\equiv(CC)} + 2\Re c_b^* c_{\text{T}} \underbrace{\langle \psi_b | \frac{\hat{\vec{r}}}{\hat{r}^3} | \psi_{\text{T}} \rangle}_{\equiv(BC)}. \quad (6.11)$$

The three resulting terms will be called bound-bound transitions (BB), continuum-continuum transitions (CC) and bound-continuum transitions (BC).

#### Bound-bound transitions

With the usual coordinate transformation  $u = \cos \theta$ , the expectation value of the dipole acceleration for the bound state reads

$$(BB) \propto \int_0^\infty dr r^{2l'} e^{-2r/na_0} \int_0^{2\pi} d\varphi \int_{-1}^1 du \frac{\vec{r}}{r} \left[ P_{l'}^m(u) L_{n-l'-1}^{2l'+1} \left( \frac{2r}{na_0} \right) \right]^2. \quad (6.12)$$



The unit vector is  $\vec{r}/r = \{\sqrt{1-u^2} \cos \varphi, \sqrt{1-u^2} \sin \varphi, u\}$ . The  $x$ - and  $y$ -component of (BB) vanish due to the integration over the azimuthal angle  $\varphi$ . Likewise, the  $z$ -component vanishes

$$\int_{-1}^1 du u \underbrace{[P_l^m(u)]^2}_{=[P_l^m(-u)]^2} = 0 \quad (6.13)$$

as a result of the antisymmetry of the integrand under  $u \rightarrow -u$  and hence, it follows

$$\boxed{(BB) = 0.} \quad (6.14)$$

In general, this follows from the fact that the Hydrogen eigenfunctions have definite parity  $\widehat{\mathcal{P}}_{\vec{r}}|\psi_b\rangle = \pm|\psi_b\rangle$  under transformations  $\widehat{\mathcal{P}}_{\vec{r}} : \vec{r} \rightarrow -\vec{r}$ . Hence, the expectation value of an operator with odd parity,  $\widehat{\mathcal{P}}_{\vec{r}}\widehat{\mathcal{O}}\widehat{\mathcal{P}}_{\vec{r}}^\dagger = -\widehat{\mathcal{O}}$ , for example  $\widehat{\mathcal{O}} = \vec{r}/\hat{r}^3$ , is

$$\langle \psi_b | \underbrace{\widehat{\mathcal{P}}_{\vec{r}}^\dagger \widehat{\mathcal{P}}_{\vec{r}}}_{=1} \widehat{\mathcal{O}} \underbrace{\widehat{\mathcal{P}}_{\vec{r}} \widehat{\mathcal{P}}_{\vec{r}}^\dagger}_{=1} | \psi_b \rangle = -\langle \psi_b | \widehat{\mathcal{O}} | \psi_b \rangle \Rightarrow \langle \psi_b | \widehat{\mathcal{O}} | \psi_b \rangle = 0. \quad (6.15)$$

### Continuum-continuum transitions

Inserting Equation (6.10) in the second term of (6.11) leads to

$$(CC) = \mathcal{N}_T^2 e^{-\frac{r_{\omega_0}^2}{\sigma^2}} \int_0^\infty dr \int_0^{2\pi} d\varphi \int_{-1}^1 du \begin{pmatrix} \sqrt{1-u^2} \cos \varphi \\ \sqrt{1-u^2} \sin \varphi \\ u \end{pmatrix} (1-u^2)^l r^{2l} e^{-\frac{r^2-2rur\omega_0}{\sigma^2}}. \quad (6.16)$$

The integrals in  $x$ - and  $y$ -direction vanish for the  $\varphi$ -integration and a factor of  $2\pi$  is obtained for the  $z$ -direction. The  $u$ - and  $r$ -integrations are performed with the help of the computer algebra system Wolfram Mathematica [57] and evaluate to

$$\int_{-1}^1 du u (1-u^2)^l e^{\frac{2rur\omega_0}{\sigma^2(t)}} = \frac{\sqrt{\pi} l!}{\Gamma(l+5/2)} \cdot \frac{r_{\omega_0} r}{\sigma^2} \cdot {}_0F_1 \left( l + \frac{5}{2}; \frac{r_{\omega_0}^2 r^2}{\sigma^4} \right). \quad (6.17)$$

Generalized hypergeometric functions are denoted by  ${}_pF_q$  and  $\Gamma(z)$  signifies the Gamma function. The remaining integral solution is

$$\int_0^\infty dr r^{2l} e^{-\frac{r^2}{\sigma^2}} \cdot \frac{r_{\omega_0} r}{\sigma^2} \cdot {}_0F_1 \left( l + \frac{5}{2}; \frac{r_{\omega_0}^2 r^2}{\sigma^4} \right) = \sigma^{2l} r_{\omega_0} \frac{l!}{2} \cdot {}_1F_1 \left( l + 1, l + \frac{5}{2}; \frac{r_{\omega_0}^2}{\sigma^2} \right). \quad (6.18)$$

Finally, the full expression reads

$$\boxed{(CC) = \frac{l! r_{\omega_0}(t)}{\Gamma(l+5/2) \sigma^3(t)} e^{-\frac{r_{\omega_0}^2(t)}{\sigma^2(t)}} \cdot {}_1F_1 \left( l + 1, l + \frac{5}{2}; \frac{r_{\omega_0}^2(t)}{\sigma^2(t)} \right) \vec{e}_z.} \quad (6.19)$$

The fastest time dependence stems from the quiver motion  $r_{\omega_0}(t)$ . It depends on the laser frequency and, therefore, the spectrum of this term will have a large peak at  $\omega_0$ .

### Bound-continuum transitions

For the combined prefactors from both wavefunctions,  $\psi_b$  and  $\psi_T$ , we introduce a new variable

$$\mathcal{N}_{bT}(t) \equiv C_{nl'm} \mathcal{N}_T(t) \exp \left[ -\frac{i}{\hbar} (S_{\omega_0}(t) + I_{p,n} t) \right] \left( \frac{2}{na_0} \right)^l \exp \left[ -\frac{r_{\omega_0}^2(t) \cdot (1-i\tau(t))}{2\sigma^2(t)} \right], \quad (6.20)$$

containing the phase corresponding to the binding energy and the kinetic energy of the electron moving in the laser field. Interference terms between both states are frequently occurring in this work and the evaluation of the integrations over  $r$  and  $u$  is rather tedious. Hence, it will be denoted with  $I(m_r, m_u, n_u, t)$  and its analytical solution is derived in Appendix B.4. All interference terms of the form  $\langle \psi_b | r^{m_r} u^{m_u} \sqrt{1 - u^2}^{n_u} | \psi_T \rangle$  can be formally solved. The approximation involved will be tested numerically in Chapter 7. The contribution to the dipole acceleration reads

$$(BC) = \mathcal{N}_{bT}(t) \begin{pmatrix} I(0,0,1,t) & 0 & 0 \\ 0 & I(0,0,1,t) & 0 \\ 0 & 0 & I(0,1,0,t) \end{pmatrix} \int_0^{2\pi} d\varphi \begin{pmatrix} \cos \varphi \\ \sin \varphi \\ 1 \end{pmatrix} e^{i(l-m)\varphi} \quad (6.21)$$

$$= \pi \mathcal{N}_{bT}(t) \cdot \begin{pmatrix} (\delta_{m,l+1} + \delta_{m,l-1}) \cdot I(0,0,1,t) \\ -i(\delta_{m,l+1} - \delta_{m,l-1}) \cdot I(0,0,1,t) \\ 2\delta_{m,l} \cdot I(0,1,0,t) \end{pmatrix} \quad (6.22)$$

and is either of longitudinal or transverse nature, depending on the vortex charge  $l$  and the magnetic quantum number  $m$ . The  $\delta$ -functions express the conservation rules for angular momentum, i.e.,

$$\boxed{m = l, l \pm 1.} \quad (6.23)$$

In order to get HHG with the ground state ( $m = 0$ ) the incoming wavepacket must be either of Gaussian shape ( $l = 0$ ) or a vortex wavepacket with vortex charge one ( $l = 1$ ). The latter case will be treated for the remainder of this chapter.

### 6.2.2 Dipole dynamics

To study the derived expression for the dipole acceleration it is useful to note that the  $x$ - and  $y$ - component of (6.22) differ only by a phase shift of  $\pm i = e^{\pm i\pi/2}$ . The integral solution  $I$  has no fast oscillation. By taking the real part of (BC) two fast oscillating terms

$$\Re(BC)_x \propto \cos\left(\frac{S_{\omega_0}(t) + I_{p,n}(t)}{\hbar}\right) \quad \Re(BC)_y \propto \sin\left(\frac{S_{\omega_0}(t) + I_{p,n}(t)}{\hbar}\right) \quad (6.24)$$

emerge from  $\mathcal{N}_{bT}(t)$ . A circular motion of the dipole acceleration in the transverse plane results from the fixed phase differences of  $\pi/2$ . This is in contrast to the traditional HHG process ( $l = 0$ ), in which the fast dipole acceleration points only in  $z$ -direction, as can be seen from Equation (6.22). In classical view, the HHG emission pattern will be that of a rotating electric dipole instead of a linear oscillating dipole. As suggested by (6.24), an alternative interpretation is the oscillation of two linear dipoles in phase lying perpendicular to the electric field axis. Moreover, the radiated electric field has a circular polarization along the  $z$ -axis, in contrast to the linear polarization of a linear emitting dipole. The nonzero  $z$ -component of (CC) is due to the acceleration and deceleration of the electron under the Coulomb force and is not related to the recombination process or HHG emission. The characteristic radiation patterns have distinct directions of maximum emission, shown in Figure 6.1. The emission pattern of a linear dipole in  $z$ -direction scales with  $\sin^2 \theta$  [20] and leads to a doughnut-shaped form. The highest intensity radiates perpendicular to the dipole axis. For a dipole rotating in the  $x$ - $y$ -plane, the Poynting vector has its largest contribution forward and backward in  $z$ -direction. Its analytical form is proportional to  $1 + \cos^2 \theta$  [20].

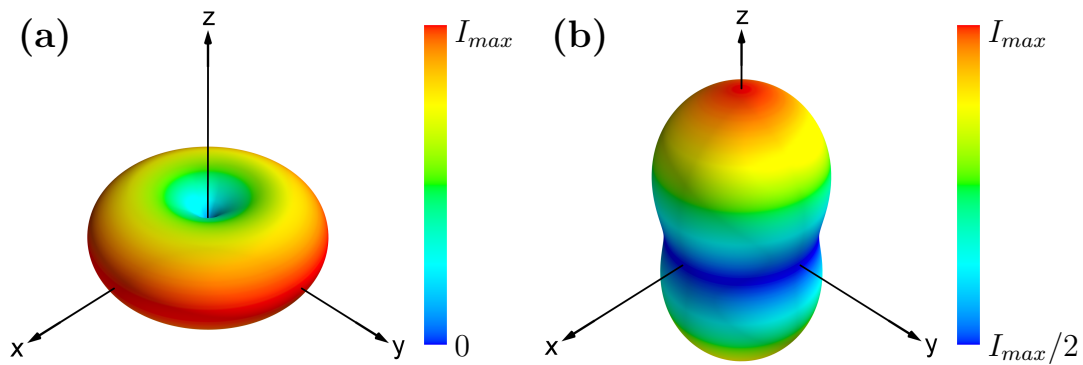


Figure 6.1: The intensity patterns of the emission from a linear dipole in  $z$ -direction (a) and a dipole rotating in the transverse plane (b) are shown. The emission strength is represented by the distance to the origin and is also color-coded.

So far no analytical expression for the coefficients in (4.3) is available. We do not expect them to change rapidly in time and, hence, approximate them in the following to be constant and real with the numerical values  $c_b = \sqrt{0.95}$  and  $c_T = \sqrt{0.05}$ . The temporal evolution of (6.11) is shown in Figure 6.2 for both laser parameter settings and half a laser cycle. This corresponds to a single collision with the ion. The  $x$ - and  $y$ -component exhibit fast oscillations. On the contrary, only slow temporal changes occur for the  $z$ -direction. Both plots show that the maximal amplitude is reached for  $r_{\omega_0}(t) \approx 0$ .

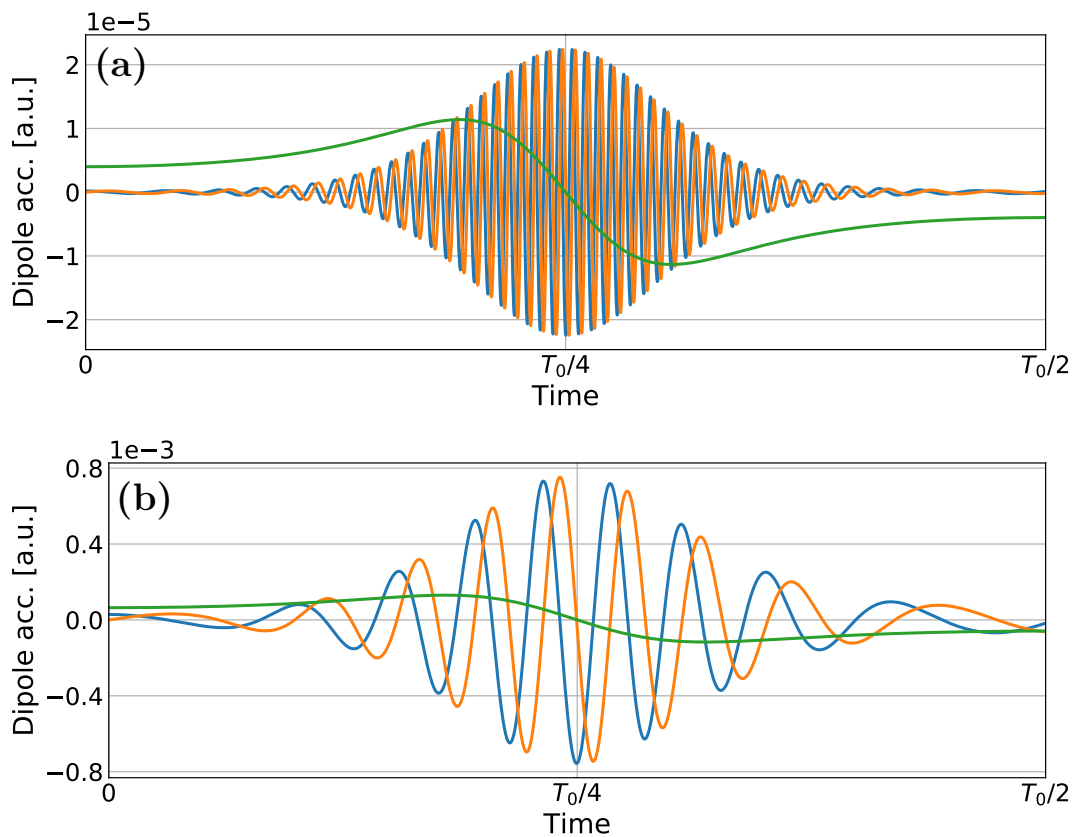


Figure 6.2: The dipole acceleration for a half laser cycle is shown for setting 1 (a) and 2 (b). The  $x$ -,  $y$ - and  $z$ -component are depicted in blue, orange and green, respectively.

### 6.3 Spectrum of interference term

The spectrum of the dipole acceleration can be extracted via Fourier transformation  $\tilde{a}(\omega) = \int dt' e^{i\omega t'} a(t')$ . Here it will depend on a finite length Fourier transformation,  $\tilde{a}(\omega, T_{\max}) \equiv \int_0^{T_{\max}} dt' e^{i\omega t'} a(t')$ , and the corresponding spectrum will be denoted by  $\mathcal{S}(\omega, T_{\max})$ . The main interest lies in the interference term, such that the analysis of the spectrum giving only peaks for the laser frequency are omitted here.

By looking at formula (6.22) for the interference term it becomes clear that only the exponential prefactors, involving the energy of the bound and free part, and the Fourier factor  $e^{i\omega t}$  are fast oscillating. In such a case the Fourier transform can be approximated with the stationary phase approximation (SPA) [30]

$$\frac{1}{\sqrt{2\pi}} \int_{x_1}^{x_2} dx e^{if(x)/\hbar} g(x) \approx \sum_{\{x_0\}} \sqrt{\frac{\hbar i}{f''(x_0)}} e^{if(x_0)/\hbar} g(x_0) \quad f'(x_0) = 0; x_1 < x_0 < x_2. \quad (6.25)$$

There are other exponential factors with complex arguments, but they all involve the timescale for wavepacket diffusion  $\tau$ . If the initial width is not chosen to be very small, they can be safely neglected. Depending on the vector component of the dipole acceleration it will give different amplitudes, but the procedure is the same for each. The SPA analysis will be given for the  $x$ -component of the spectrum. However, the analysis would yield the exact same result for the  $y$ -direction. We omit constant prefactors for now and express the dipole acceleration as

$$\begin{aligned} a_x(t) &\propto 2\Re \langle \psi_b(t) | \frac{\hat{r}}{\hat{r}^3} | \psi_T(t) \rangle \propto 2\Re \left[ \mathcal{N}_{bT}(t) \cdot I(0, 0, 1, t) \right] \\ &\propto \mathcal{N}_T(t) e^{-\frac{r_{\omega_0}^2(t)}{2\sigma^2(t)}} \\ &\quad \cdot \begin{cases} \underbrace{I(0, 0, 1, t)}_{\in \mathbb{R}} \cdot 2\Re \left[ e^{-\frac{i}{\hbar}(S_{\omega_0}(t) + I_{p,n}t)} e^{i\frac{r_{\omega_0}^2(t)\tau(t)}{2\sigma^2(t)}} \right] & \text{for } l' + |m| \text{ even} \\ \underbrace{I(0, 0, 1, t)}_{\in \mathbb{R}} e^{-i\pi/2} \cdot 2\Re \left[ e^{-\frac{i}{\hbar}(S_{\omega_0}(t) + I_{p,n}t)} e^{i\frac{r_{\omega_0}^2(t)\tau(t)}{2\sigma^2(t)}} e^{i\pi/2} \right] & \text{for } l' + |m| \text{ odd.} \end{cases} \end{aligned} \quad (6.26)$$

It was assumed that  $m = l - 1$ ,  $c_b, c_f \in \mathbb{R}$  and that  $I$  is either real or purely imaginary (see end of Appendix B.4). In the SPA only the term with the negative exponent is important and it is not necessary to take the real part, because  $\int dt e^{i\omega t} (e^{-i\bar{\omega}t} + e^{i\bar{\omega}t}) \approx \int dt e^{i\omega t} e^{-i\bar{\omega}t}$  (with positive  $\omega, \bar{\omega}$ ). For the sake of clarity we assume  $l' + |m|$  to be even. In that case the functions in (6.25) are

$$g(t) = \mathcal{N}_T(t) e^{-\frac{r_{\omega_0}^2(t)}{2\sigma^2(t)}} \cdot I(0, 0, 1, t), \quad (6.28)$$

$$f(\omega, t) = \hbar\omega t - \left( I_{p,n}t + S_{\omega_0}(t) \right) + \underbrace{\frac{r_{\omega_0}^2(t)\tau(t)\hbar}{2\sigma^2(t)}}_{\approx 0}, \quad (6.29)$$

$$\dot{f}(\omega, t) = \hbar\omega - \left( I_{p,n} + 2U_p \sin^2(\omega_0 t) \right) - \underbrace{\partial_t \frac{r_{\omega_0}^2(t)\tau(t)\hbar}{2\sigma^2(t)}}_{\approx 0}, \quad (6.30)$$

$$\ddot{f}(\omega, t) \approx -2U_p \omega_0 \sin(2\omega_0 t). \quad (6.31)$$

The stationary points for fixed frequency  $\omega$  have to be determined from  $\dot{f} \stackrel{!}{=} 0$  and give

$$\omega_0 t_{j,\pm}(\omega) = \pm \arcsin \left( \sqrt{\frac{\hbar\omega - I_{p,n}}{2U_p}} \right) + j\pi \quad \omega \in [I_{p,n}, I_{p,n} + 2U_p], j \in \mathbb{Z}, \quad (6.32)$$

$$\Rightarrow \cos(\omega_0 t_{j,\pm}) = (-1)^j \sqrt{\frac{2U_p + I_{p,n} - \hbar\omega}{2U_p}}, \quad (6.33)$$

$$\Rightarrow \sin(\omega_0 t_{j,\pm}) = \pm (-1)^j \sqrt{\frac{\hbar\omega - I_{p,n}}{2U_p}}. \quad (6.34)$$

For the last line the relation  $\cos(\arcsin(x)) = \sqrt{1-x^2}$  was used. The number of stationary points is constraint by the length of the laser pulse. Additionally, stationary points exist only for  $\omega \in [I_{p,n}, I_{p,n} + 2U_p]$ , the plateau region. Let  $T_{\max}$  denote the pulse/integration length and start at  $t_0 = 0$ . Then, only those points contribute that are within this time period, i.e.,

$$0 < t_{j,\pm} < T_{\max}. \quad (6.35)$$

We note also that  $r_{\omega_0}^2(t_{j,\pm}) = 2(2U_p + I_{p,n} - \hbar\omega)/(m_e\omega_0^2)$  has the same value for every stationary point. Furthermore it holds that  $A^2(t_{j,\pm}) = 2m_e(\hbar\omega - I_{p,n})/q^2$  and, hence,  $I(0, 0, 1, t_{j,\pm}) = I(0, 0, 1, t_{0,+})$ . For the stationary points the functions in the SPA evaluate to

$$g(t_{j,\pm}(\omega)) = \mathcal{N}_T(t_{j,\pm}) \cdot I(0, 0, 1, t_{j,\pm}) \exp \left[ -\frac{(2U_p + I_{p,n} - \omega)}{m_e\omega_0^2 \cdot \sigma^2(t_{j,\pm})} \right], \quad (6.36)$$

$$f(t_{j,\pm}(\omega)) = (\hbar\omega - I_{p,n} - U_p) t_{j,\pm} \pm \frac{1}{2\omega_0} \sqrt{(\hbar\omega - I_{p,n})(2U_p + I_{p,n} - \hbar\omega)} \quad (6.37)$$

$$\ddot{f}(t_{j,\pm}(\omega)) = \ddot{f}(t_{0,\pm}(\omega)) = \mp 2\omega_0 \sqrt{(\hbar\omega - I_{p,n})(2U_p + I_{p,n} - \hbar\omega)}. \quad (6.38)$$

Putting everything together gives

$$\begin{aligned} \tilde{a}_x(\omega, T_{\max}) &\approx c_b c_T \pi C_{nl'm} \left( \frac{2}{na_0} \right)^{l'} \frac{\sqrt{\hbar i} \cdot I(0, 0, 1, t_{0,+})}{\sqrt{2\omega_0} ((\hbar\omega - I_{p,n})(2U_p + I_{p,n} - \hbar\omega))^{1/4}} \\ &\quad \times \sum_{\{0 < t_{j,\pm} < T_{\max}\}} \sqrt{\mp 1} \cdot \mathcal{N}_T(t_{j,\pm}) \cdot \exp \left[ -\frac{(2U_p + I_{p,n} - \hbar\omega)}{m_e\omega_0^2 \cdot \sigma^2(t_{j,\pm})} \right] \\ &\quad \times \exp \left[ i \left\{ (\hbar\omega - I_{p,n} - U_p) t_{j,\pm} \pm \frac{1}{2\omega_0} \sqrt{(\hbar\omega - I_{p,n})(2U_p + I_{p,n} - \hbar\omega)} \right\} / \hbar \right]. \end{aligned} \quad (6.39)$$

If the diffusion time  $\tau$  is negligible, the result can be further simplified to

$$\begin{aligned} \tilde{a}_x(\omega, T_{\max}) &\approx c_b c_T \pi C_{nl'm} \left( \frac{2}{na_0} \right)^{l'} \frac{\sqrt{\hbar i} \cdot I(0, 0, 1, t_{0,+})}{\sqrt{2\omega_0} ((\hbar\omega - I_{p,n})(2U_p + I_{p,n} - \hbar\omega))^{1/4}} \\ &\quad \times \mathcal{N}_T(0) \exp \left[ -\frac{(2U_p + I_{p,n} - \hbar\omega)}{m_e\omega_0^2 \cdot \alpha^2} \right] \\ &\quad \times \sum_{\{0 < t_{j,\pm} < T_{\max}\}} \sqrt{\mp 1} \exp \left[ \frac{i}{\hbar} \left\{ (\hbar\omega - I_{p,n} - U_p) t_{j,\pm} \pm \frac{1}{2\omega_0} \sqrt{(\hbar\omega - I_{p,n})(2U_p + I_{p,n} - \hbar\omega)} \right\} \right]. \end{aligned} \quad (6.40)$$

In order to determine the spectrum, the absolute square value of the last line has to be taken. If  $T_{\max}$  is not too small, common factors can be extracted and combined to

$$|\tilde{a}_x(\omega, T_{\max})|^2 \propto \sum_{j,j'} \exp \left[ i \frac{\hbar\omega - I_{p,n} - U_p}{\hbar\omega_0} \cdot \pi(j - j') \right] \quad (6.41)$$

$$\propto \sum_{\Delta j=0}^{j_{\max}} \cos \left( \frac{\hbar\omega - I_{p,n} - U_p}{\hbar\omega_0} \cdot \pi \Delta j \right). \quad (6.42)$$

This expression gives peaks at

$$\boxed{\hbar\omega_{\text{peak},k} = (I_{p,n} + U_p) + 2\hbar\omega_0 \cdot k}, \quad (6.43)$$

equal to the one-dimensional case (see Section 2.3.2). Hence, the cutoff location in frequency space is not changed with twisted electrons, but instead the characteristic emission directions change. The HHG emission is mainly directed along the  $z$ -axis, perpendicular to the laser propagation. This is one of the main results of this thesis.

Equation (6.39) can be tested against a numerically obtained spectrum. The particular case of a twisted wavepacket ( $l = 1$ ) and the ground state ( $m = 0$ ) is treated. We use a Fast Fourier Transform (FFT) [30] to obtain the frequency content of (6.11). The wavefunction coefficients were kept constant ( $c_b = \sqrt{0.95}$ ,  $c_T = \sqrt{0.05}$ ) and the pulse length was three cycle periods. The results for both laser parameter settings are shown in Figure 6.3.

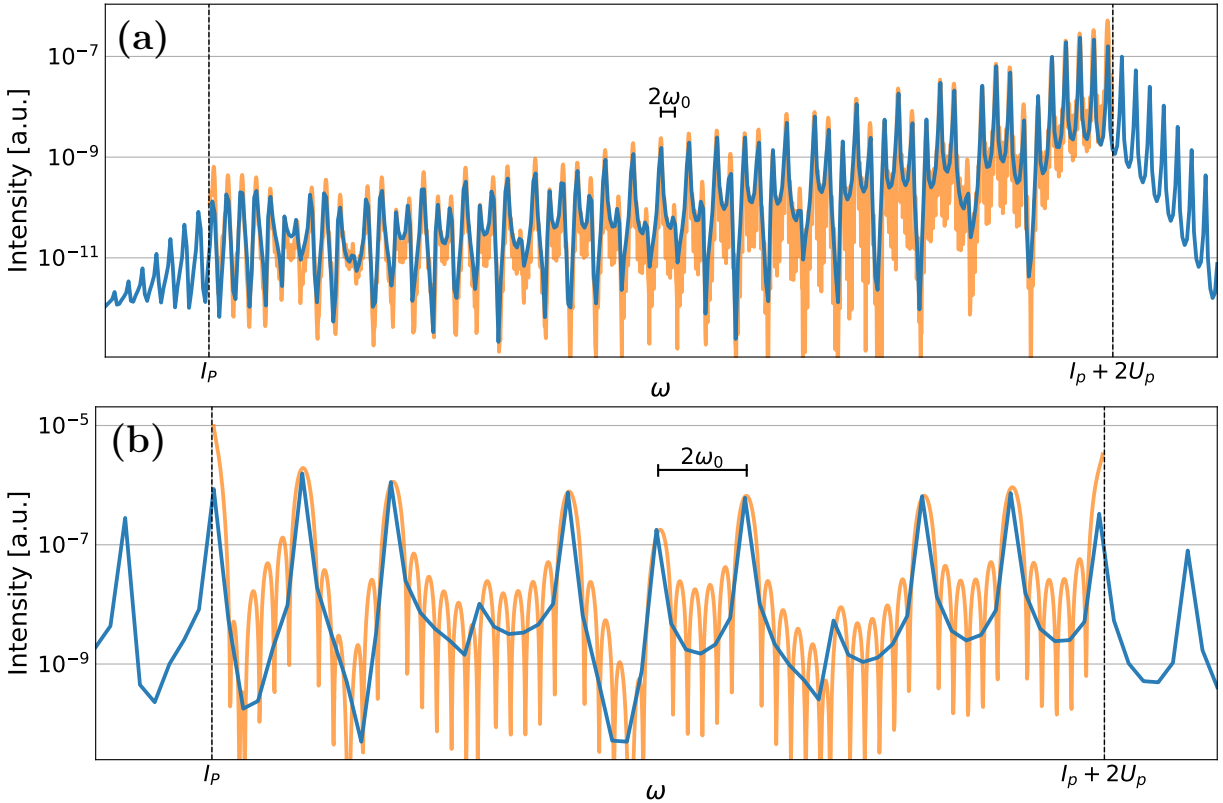


Figure 6.3: The SPA approximation (6.39) (orange) of the plateau region is compared to the numerical spectrum (blue) of the interference term (6.11) in  $x$ -direction. The upper plot shows the results for parameter setting 1 (a) and the lower plot for setting 2 (b). The spacing of  $2\omega_0$  between adjacent peaks is indicated by the vertical black bar.

Both curves are in good agreement around the peak structures and demonstrate a good approximation by the SPA. An additional observation is the intensity difference between both parameter settings. They differ by approximately two orders of magnitude and represent the general trade-off between a high intensity and a high cutoff frequency. Wavepackets with a higher mean kinetic energy will have a shorter interaction time with the binding potential and this results in a smaller recombination probability. Equation (6.40) is an important formula to investigate the influence of the wavepacket width on the spectral intensity. This expression is of a general class describing the HHG spectrum for finite wavepackets. A similar expression would be derived for  $l = 0$  and even in the case of a 1D system with a Gaussian wavepacket. Hence, the findings below will apply to those systems as well.

### 6.3.1 Width dependence

The logarithmic scaling of the spectrum (6.40)

$$\log |\tilde{a}_x(\omega)|^2 \propto \frac{1}{m_e \omega_0^2 \alpha^2} (\hbar\omega - (2U_p + I_{p,n})) \quad (6.44)$$

shows qualitatively the slope of the plateau in frequency space for negligible wavepacket diffusion. This suggests that for smaller  $\alpha$  the lower end of the plateau is suppressed while the frequencies around the cutoff are enhanced. There is a very intuitive explanation for this relationship. The extremal points of the exponent in the SPA (6.25) identify the emission times (6.32) for a specific frequency  $\omega$ . Frequencies around the cutoff are emitted if the free part is very close to the core. On the other hand, lower frequencies in the plateau are emitted if the wavepacket is further away. The smaller the extension of the wavepacket, the higher the overlap for the former and the lower for the latter case. This behaviour is sketched for the ground state in Figure 6.4. For  $r_{\omega_0}(t) \approx 0$  the maxima of the free electron wavepacket will overlap with the maxima of the ground state wavefunction. The overlap is large and we expect the transition probability for recombination to be maximal as well. On the other hand, for  $r_{\omega_0}(t) \approx z_{\max}$ , the wavepacket center is far outside the bound region and the overlap is minimized. If the extension of the free states is smaller than the excursion amplitude of the center, then the transition element will be negligibly small.

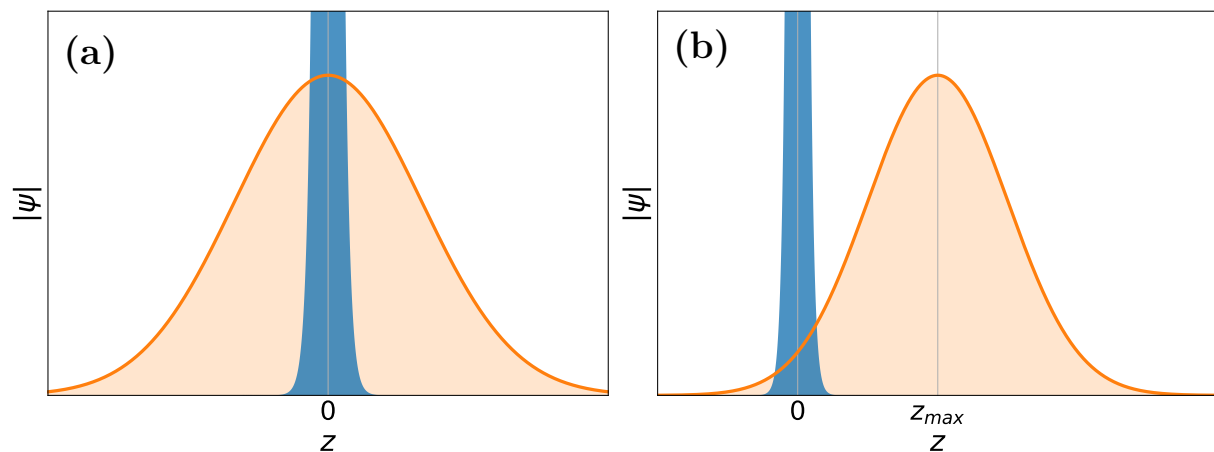


Figure 6.4: The overlap between the bound ground state (blue) and the free electron part (orange) depends on the phase of the laser field. This behavior is shown for  $r_{\omega_0}(t) \approx 0$  in the left plot (a) and for  $r_{\omega_0}(t) \approx z_{\max}$  in the right plot (b).

The relation (6.44) is only true for small  $\tau$ , when wavepacket diffusion can be neglected. If the initial width is small, then the fast expansion of the wavefunction counteracts and will diminish

the spectral intensity. Since the stationary phase approximation performs reasonably well, the dependence of the spectral intensity on the initial width  $\alpha$  is investigated by means of (6.39). The variation of the plateau region is presented in Figure 6.5. The wavefunction coefficients are identical to the ones above ( $c_b = \sqrt{0.95}$ ,  $c_T = \sqrt{0.05}$ ), although the time integration is performed over three cycle periods, i.e.,  $T_{\max} = 3T_0$ , in order to see effects of wavefunction diffusion. For setting 1 we find a minima for the lower frequency end which is absent for setting 2. We suspect it to result from the clear separation of bound and free electron wavefunction at times  $r_{\omega_0}(t) \approx z_{\max}$  for the former, see Section 5.5. Both spectra exhibit a maxima in the highest frequency component marking optimal points for the initial width. At these points the two competing factors, namely wavefunction spreading and recombination probability by means of the wavefunction overlap, are balanced. This is the second important result of this work.

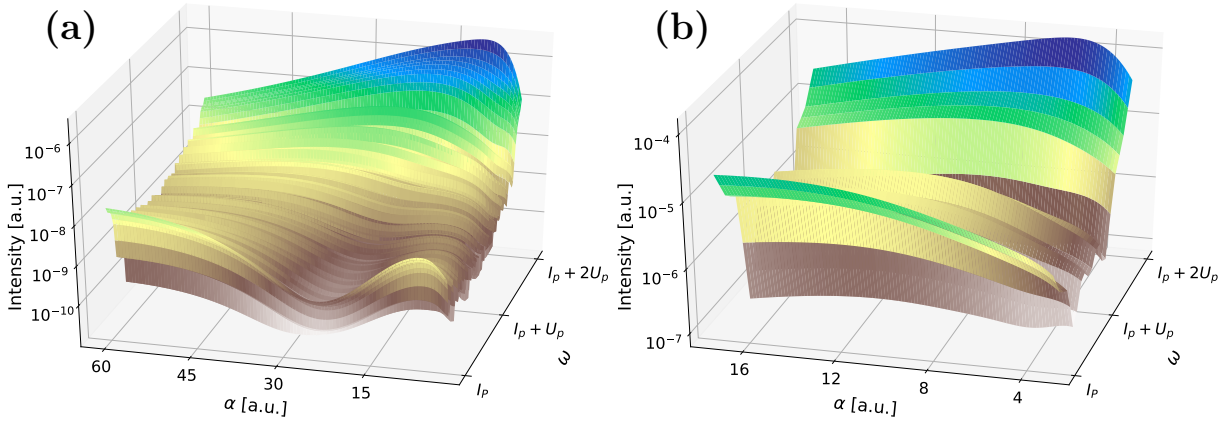


Figure 6.5: The spectra of the SPA (6.39), color-coded as an optical guidance, are shown for a range of initial widths  $\alpha$ . Only the high harmonic peaks are shown for setting 1 (a) and setting 2 (b).

## HHG yield

Another metric to investigate the dependency of the total high harmonic frequency content on the wavepacket width is the HHG yield

$$Y \equiv \int_{I_p/\hbar}^{(I_p+2U_p)/\hbar} d\omega S(\omega), \quad (6.45)$$

which is defined as the spectral integration over the plateau area  $[I_p, I_p + 2U_p]$ . Other yield definitions have been used as well to study scaling properties for HHG [58]. The dependence is shown in Figure 6.6, including the spectral intensity of the highest harmonic for comparison. The pulse length and coefficients for ground state and free twisted wavepacket are the same as above used in Figure 6.5. Both quantities share a similar relationship to  $\alpha$ . The yield has a maximum point which lies close to the intensity maxima for the highest harmonic, indicating an optimal initial width not only for one frequency but the whole plateau region.



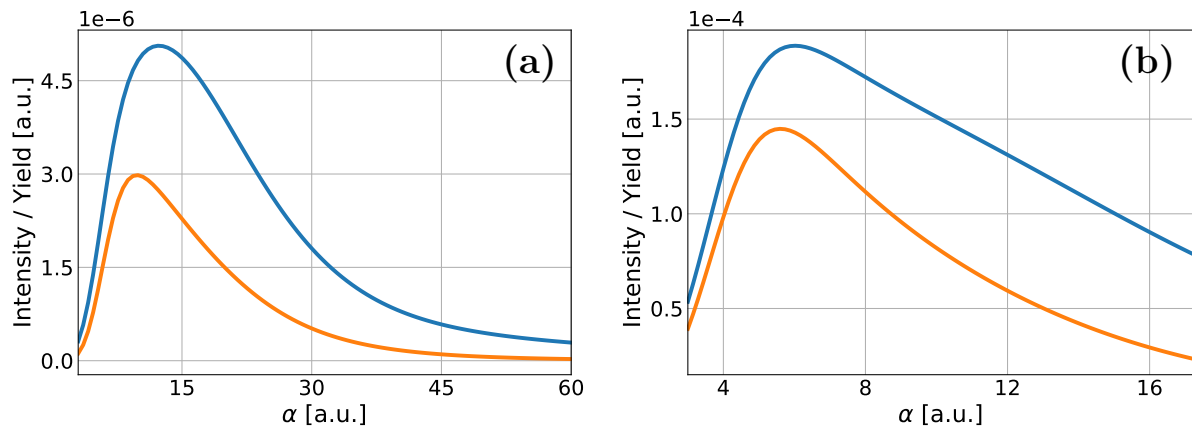


Figure 6.6: The yield  $Y$  (blue) and the intensity of highest harmonic frequency (orange) are compared in dependence of the initial width  $\alpha$  for both laser settings. The left plot corresponds to setting 1 (a) and the right to setting 2 (b).



# 7 Numerical Results

The need for numerical calculations first becomes apparent if one were to try to derive analytical formulas for off-axis scattering scenarios. The calculations become very complex and might not have a satisfactory solution. Even for the central collisions an approximation had to be made (Appendix B.4). Aforesaid approximation of the interference term has to be compared to exact results from numerical integrations, which is done in Section 7.1. Two other issues must be addressed. First, the time evolution of the wavefunction coefficients in (4.3) is unknown and were therefore set to constant values. Second, as explained in Section 4.2, the free part of the electron wavepacket eventually passes through the vicinity of the origin. The approximation that lead to the analytical form of the twisted wavepacket breaks down in aforementioned region and the effect of the Coulomb potential cannot be neglected anymore. For these two reasons, we apply a full three-dimensional quantum simulation to the system and propagate initial wavefunctions under the full Hamiltonian. The simulation method and details are introduced in Section 7.2 and the numerical results are presented in Section 7.3. Throughout this chapter atomic units are employed (Appendix C.1).

## 7.1 Dipole acceleration

We wish to compare the analytical formulas of Section 6.2 to exact numerical results. This can only be done for a specific set of parameters, but allows to obtain results which are hard to solve analytically, for example  $\beta \neq \alpha$  and off-axis scattering with an impact parameter  $b$  (Section 7.1.2). The numerical integration of Equation (6.11) was performed in cylindrical coordinates over a finite, but sufficiently large volume and a Gauss-Legendre quadrature scheme [59] was employed with modified C code from Holoborodko [60]. The number of sampling points is 256 for the  $\rho$ -integration and 22 for the  $\varphi$ -integration. The  $z$ -integration was performed with a varying number of sampling points depending on the strength  $A_0$  of the vector potential and the phase of the laser field. However, the maximum number of nodes is approximately 1000. In general, it could be possible to initially prepare the atom in an excited state, since the mean lifetime in Hydrogen before spontaneous decay happens ( $\tau(2p \rightarrow 1s) \propto 10^{-9}$  s) is much longer than the timescale of the laser interaction ( $T_0 \propto 10^{-15}$  s). Hence, we perform the procedure for different bound states and different vortex charges. It will give an estimate of the HHG strength for recombinations to other states. The combinations used in the following are given in Table 7.1.

| Hydrogen |      |     | Vortex |
|----------|------|-----|--------|
| $n$      | $l'$ | $m$ | $l$    |
| 1        | 0    | 0   | 0      |
| 1        | 0    | 0   | 1      |
| 2        | 0    | 0   | 1      |
| 2        | 1    | 1   | 1      |
| 2        | 1    | 1   | 2      |

Table 7.1: Five different combinations of quantum numbers for the Hydrogen ground state and the twisted wavepacket were used for an evaluation of the analytically obtained result. The first row corresponds to traditional HHG and is included for comparison.

We start with the comparison of the analytical and numerical results within the dipole approximation in Section 7.1.1 before we proceed to off-axis scattering and magnetic corrections in Sections 7.1.2 and 7.1.3, respectively. Analogously to Chapter 6, we use the constant values  $c_b(t) = \sqrt{0.95}$  and  $c_T(t) = \sqrt{0.05}$  for the wavefunction coefficients throughout this section, due to the lack of an analytical formula for their exact expressions.

### 7.1.1 Dipole approximation

The interference term (6.22) shows that HHG dynamics appears either in longitudinal or transverse direction. Hence, for each combination in Table 7.1 and for both parameter settings in Table 5.1 only one component is shown for comparison, i.e., either  $a_x$  or  $a_z$ . The numerical outcomes for both settings are presented in Figures 7.1 and 7.2.

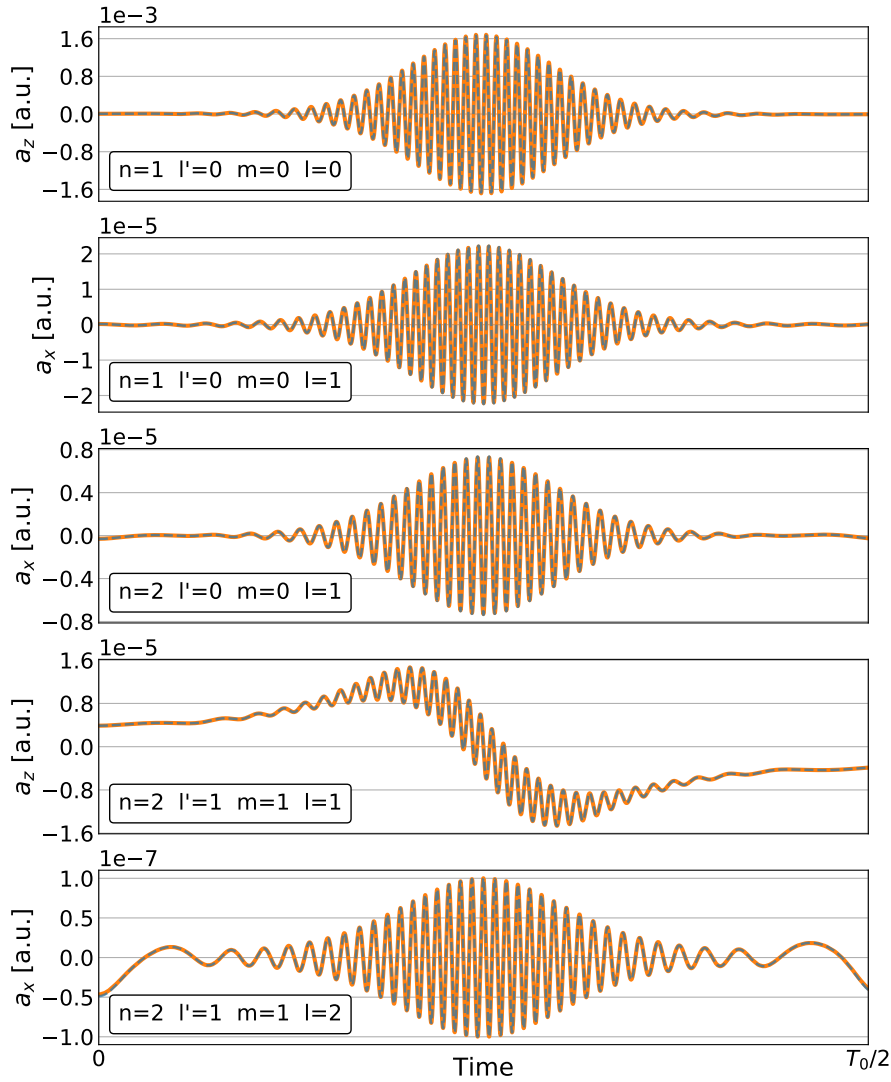


Figure 7.1: The numerically obtained dipole acceleration (orange solid line) is compared to the analytical results (6.11) for  $\vec{a}(t)$  (blue dashed line) in parameter setting 1. The different plots correspond to the different quantum number combinations from Table 7.1 and are shown in each plot. Only one component with the relevant HHG dynamics is shown for each case for half a cycle period. The order of magnitude is given above each subplot.

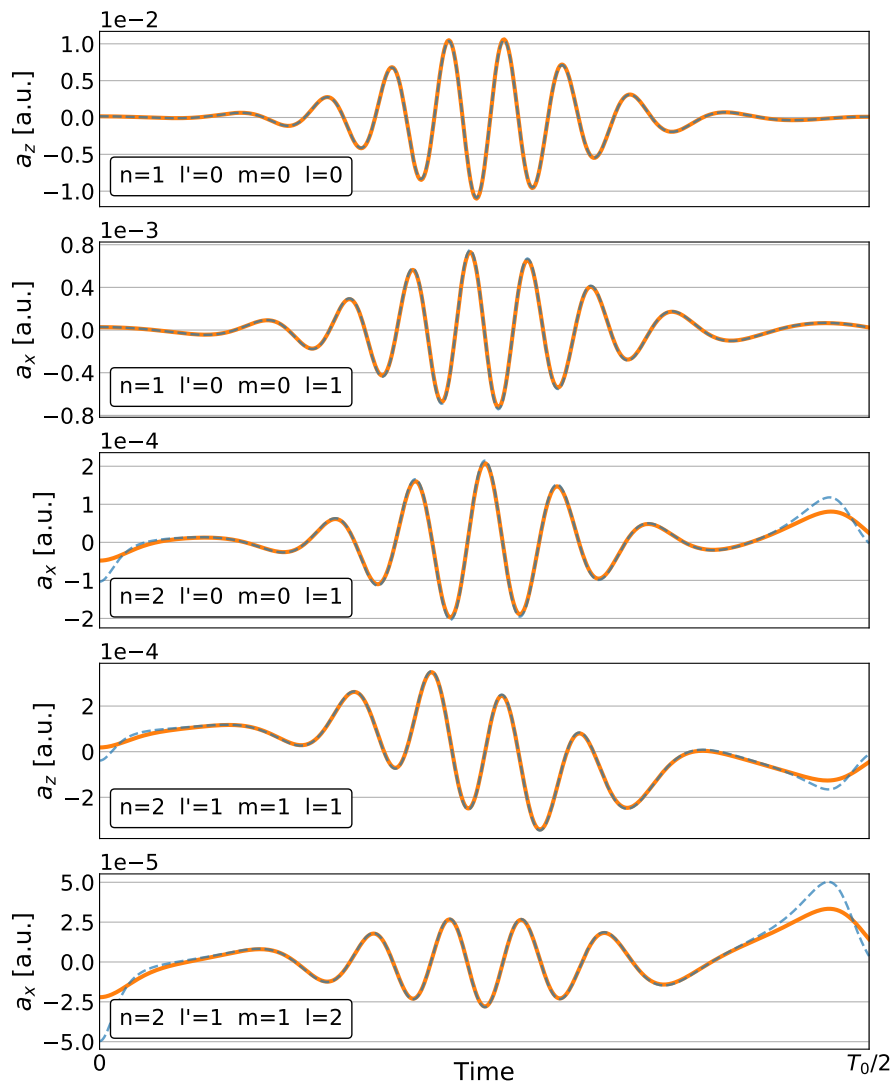


Figure 7.2: The numerically obtained dipole acceleration (orange solid line) is compared to the analytical results (6.11) for  $\vec{a}(t)$  (blue dashed line) in parameter setting 2. The different plots correspond to the different quantum number combinations from Table 7.1 and are shown in each plot. Only one component with the relevant HHG dynamics is shown for each case for half a cycle period. The order of magnitude is given above each subplot.

In conclusion, the analytically derived solutions from Chapter 6 match the numerically calculated dipole accelerations very well. Apparent deviations can be identified only for setting 2 for times  $r_{\omega_0}(t) \approx z_{\max}$ . It implies that the approximation in Appendix B.4 is less reliable when the free wavepacket is furthest away from the binding potential. The approximate solutions seem to overestimate the amplitude in these regions.

Furthermore, the comparison of different recombination possibilities for a twisted wavepacket with  $l = 1$  into either the ground state or two excited states with  $m = 0, 1$  shows that the ground state contribution is always the largest. Their dipole acceleration amplitudes differ by at least a factor of three or four, which in turn leads to a difference of one order of magnitude in the spectrum. Hence, we argue that the approximation of taking only the ground state into account holds for twisted electrons, as long as the main interest lies only on the process with the highest

recombination probability. Due to the small probability density of a twisted wavepacket at  $\rho = 0$  the intensity of HHG emission is smaller than for a Gaussian Volkov wavepacket ( $l = 0$ ).

### 7.1.2 Impact parameter

It is very unlikely to produce a central collision of a twisted wavepacket with an ion in a real experiment. In general, the transverse centers will be displaced by an impact parameter  $b$ . As there is no simple analytical expression available, we limit our study to numerical results. The HHG dynamics depends on the geometry of the system (Figure 7.3) and will change with varying  $b$ . The rotational symmetry of the system is broken for this off-axis scattering. Hence, we expect the two transverse components of the dipole acceleration to experience changes depending on the direction relative to the offset. In the following the impact parameter is incorporated through a shift in  $x$ -direction by  $b$  (not shown in Figure 7.3).

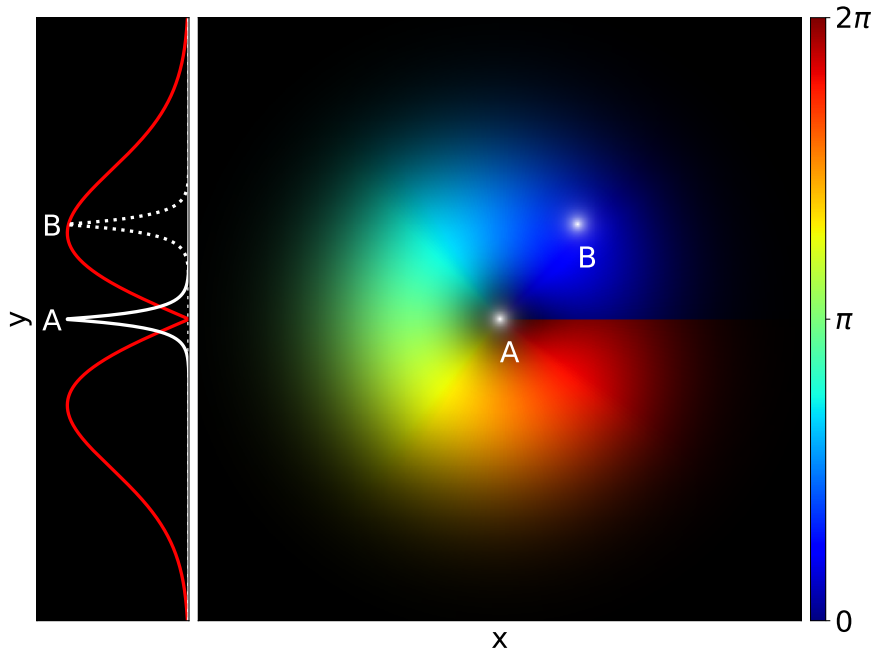


Figure 7.3: A schematic representation of the overlap between Hydrogen ground state (white) and twisted electron wavepacket (colored) with  $l = 1$  in the transverse plan is shown for  $r_{\omega_0}(t) = 0$ . The wavefunction moduli  $|\psi_i|$  are represented with the transparency. The phase information is color-coded and the transverse modulus distributions are shown in the left plot. The central collision scenario ( $b = 0$ ) is indicated by A and the off-axis scattering ( $b \neq 0$ ) by B.

Since the number of possible quantum number combinations and  $b$  values is large, we will focus only on the recombination of a vortex wavepacket with  $l = 1$  into the ground state. The changes due to the transverse shift are demonstrated by one exemplary set of parameters ( $b = 7$ , setting 2) in Figure 7.4. It is representative for all other cases. Furthermore, we show the dipole acceleration only up to half a laser cycle to keep the effect of wavefunction spreading at a minimum. However, the spectrum is obtained for two cycle periods. Each dipole acceleration component is changed due to a nonzero impact parameter and several essential differences occur.  $a_x$  and  $a_y$  experience a different reduction in amplitude. There is also a clear phase-shift for the  $x$ -component, while the  $y$ -component experiences only a very small phase-shift. However, their peak frequencies are unchanged, in contrast to the spectral intensity of  $a_z$ . Due to the symmetry

breaking, the HHG contribution in  $z$ -direction does not vanish anymore and shows the typical fast oscillations on top of the slowly varying curve from the (CC) term in (6.11). In addition, the harmonic peak emission frequencies differ by exactly one laser frequency  $\omega_0$  compared to the transverse components. The intensity around the cutoff is also two orders of magnitude larger than for the transverse dipole acceleration. The behavior of  $a_z$  can be explained by an exceeding contribution from a small range of phases. The overlap of both wavefunctions is higher for this range than for all other phase contributions. Therefore, they do not cancel out anymore, see Figure 7.3. However, we were not able to identify the cause of the differing transverse amplitude reductions and of the occurrence of ‘even’ harmonics for  $S_z$ . It should be further investigated. Every component has HHG oscillations and the direction of strongest emission will depend on the relative phase and the amplitude of each component.

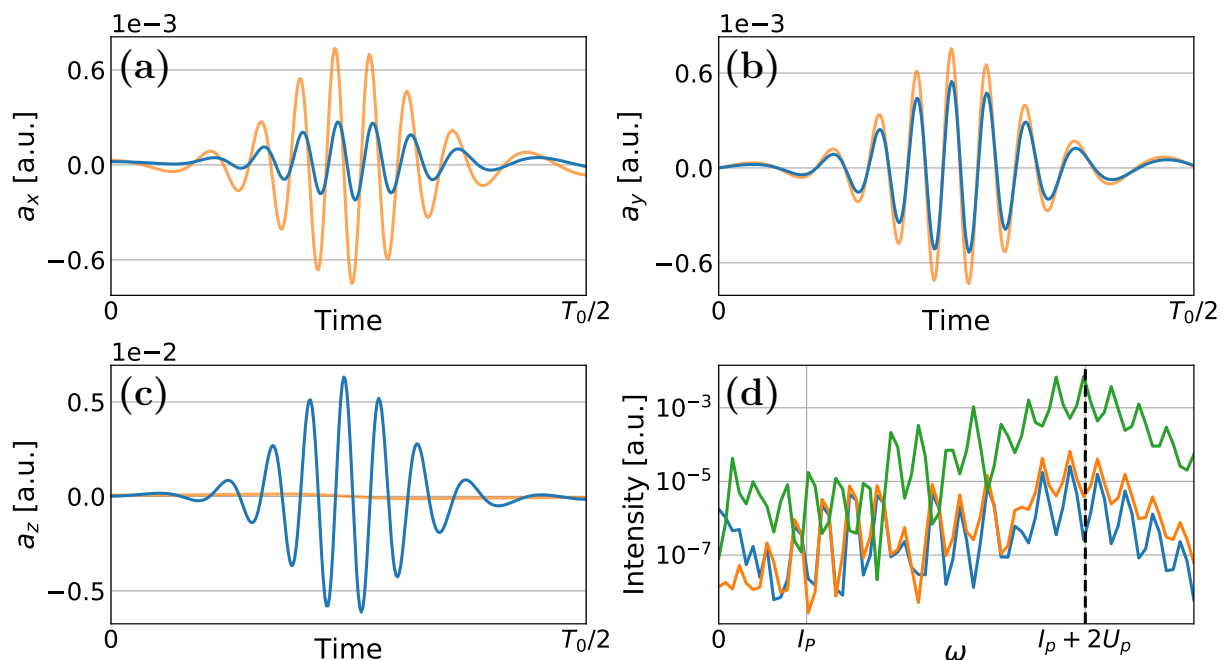


Figure 7.4: The dipole acceleration components (a), (b), (c) and its spectrum (d) are shown for parameter setting 2 with an impact parameter of  $b = 7$ . The blue lines in the dipole acceleration plots correspond to the off-axis scattering and the orange lines to the associated central collision scenario  $b = 0$ . The spectral components  $S_x$ ,  $S_y$  and  $S_z$  are represented by blue, orange and green lines, respectively. The dashed line indicates the theoretical cutoff frequency.

Motivated by these striking observations, it is imperative to investigate the change of these deviations with varying impact parameter. We estimate the phase-shift of the dipole acceleration in  $x$ - and  $y$ -component by means of a lagged Pearson correlation analysis. Therein we shift the analytical solutions by a phase  $e^{i\varphi_0}$  before taking the real part and calculate the correlation coefficient with the numerical dipole acceleration. The lagged correlation will be maximal for the phase-shift realized by the impact parameter. The integration time was chosen to be one cycle period and the results are presented in Figure 7.5. It becomes apparent that both transverse components experience a phase shift. The phase-shift on  $a_x$  equals exactly  $\pi/2$  for  $b = \alpha$  if the position shift of the wavefunction maxima, due to diffusion, can be neglected. The slight deviation for setting 2 results from wavefunction spreading. The rate of change for the phase-shift  $\partial\Delta\varphi/\partial b$  is also largest around this value. For  $b > \alpha$  both changes in the phase-shift happen with approximately the same rate, i.e.,  $\partial\Delta\varphi_x/\partial b \approx \partial\Delta\varphi_y/\partial b$ .

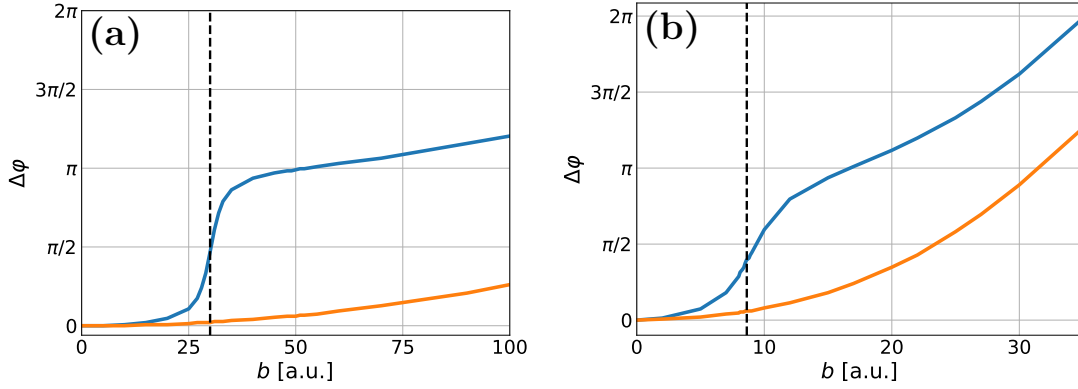


Figure 7.5: The phase-shifts on the transverse dipole acceleration components for  $b \neq 0$  compared to the  $b = 0$  result are shown for setting 1 (a) and setting 2 (b). The blue curve represents the phase-shift for  $a_x$  and the orange curve for  $a_y$ . For both settings the initial width  $\alpha$  is indicated by the black dashed line.

The second important quantity to examine further is the dependence of the spectral intensity of the highest harmonics. Again, the integration time was chosen to be one cycle period. The spectral intensities are presented in Figure 7.6 and show pronounced features for  $b = \alpha$  as well.

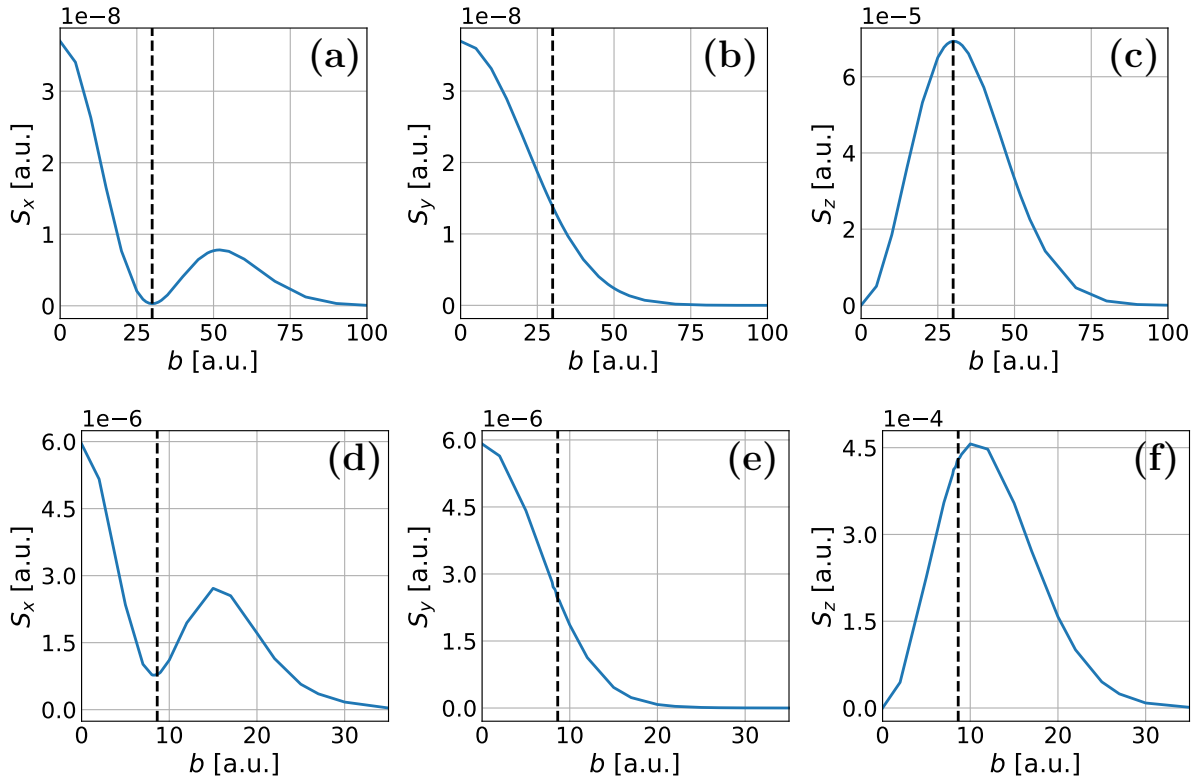


Figure 7.6: The first row of plots (a), (b) and (c) represents the spectral intensity components (2.13) of setting 1 for changing impact parameter. The second row of plots (d), (e) and (f) corresponds to the same observables in setting 2. The left, middle and right columns of plots show the spectra for the  $x$ -,  $y$ - and  $z$ -components of the dipole acceleration in successive order. The black dashed lines indicate the initial width of the twisted wavepacket.



The  $y$ -components show monotonically decreasing curves without additional structure. However, the  $x$ - and  $z$ -components exhibit local extrema at  $b = \alpha$ , namely a minimum for  $a_x$  and a maximum for  $a_z$ . In addition, the local minima are followed by a local maxima for  $b > \alpha$  while the other two components display only steady decline at these points. For setting 2 the maximum in the  $S_z$ -curve is slightly shifted to the right due to wavefunction diffusion. The maxima for  $S_z$  can be argued to stem from the maximal overlap between both wavefunctions for a small region of  $\varphi$ -values. In addition, the intensity of this component can reach values up to two or three orders of magnitude larger than the transverse components. Unfortunately, the origin of the occurring local extrema in  $S_x$  is still unknown to us. The yield analysis (see definition in Section 6.3.1) gives similar results and is therefore not shown.

### 7.1.3 Magnetic field contributions

In Chapter 5 we examined the influence of the magnetic field from the laser on the twisted wavepacket and derived an analytical expression for the wavefunction. However, we did not calculate the dipole acceleration with the correction  $F$  from Equation (5.19). Hence,  $\vec{a}(t)$  is obtained numerically in this section and its dynamics can be understood in the light of the classical correspondence described in Section 5.4.2. As in Section 7.1.2, we investigate only recombination of a  $l = 1$  vortex state into the ground state and show the dipole acceleration for one half cycle but integrate over two laser periods for the spectrum. The effects of the magnetic field on the dipole acceleration with setting 2 and zero impact parameter are shown in Figure 7.7 for one particular set of parameters.

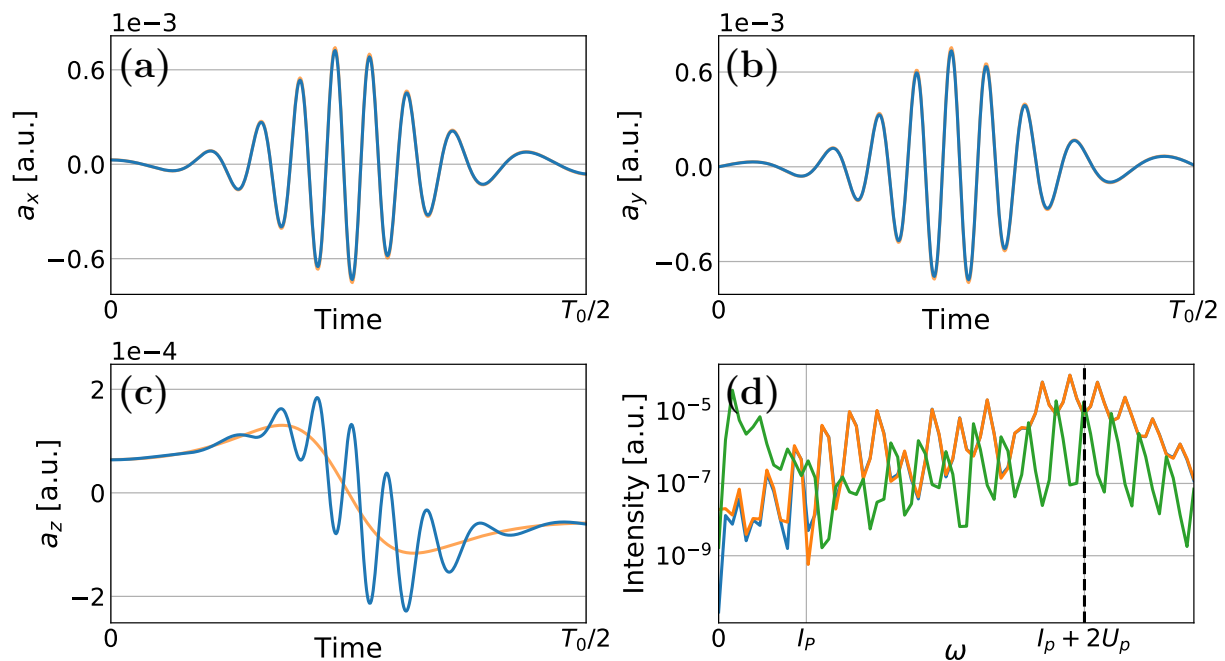


Figure 7.7: The numerically acquired dipole acceleration  $\vec{a}(t)$  and its spectrum for a nonzero magnetic field from the laser are presented. For (a), (b) and (c) the blue lines indicate the calculated dipole acceleration and the orange line represents the corresponding computation without the correction term. The associated spectrum for each component is shown in the lower right plot (d).  $S_x$ ,  $S_y$  and  $S_z$  are represented by blue, orange and green lines, respectively. The dashed line indicates the theoretical cutoff frequency  $I_p + 2U_p$ .

We recognize the outcome to be equal to a nonzero impact parameter and attribute this behavior to the continuous shift of the wavepacket center in the direction of the laser propagation, as calculated in Section 5.4.2. Since the magnetic field does not change the orbital angular momentum of the twisted wavepacket in first order perturbation, no other effects are expected by us.

## 7.2 Full quantum simulation

In order to perform a full quantum simulation we introduce the technical details of the implementation in this section. We use a split-operator method for the three-dimensional quantum simulations with a symmetric second order approximation for the time evolution operator [61]. This approximation leads for time-independent Hamiltonians to a cubic scaling for the error, i.e.,  $\propto \mathcal{O}(\Delta t^3)$  [62, 30]. The propagation with a time-dependent Hamiltonian does not pose a problem as long as the change of the potential per time step  $\Delta t$  is small, i.e.,  $\frac{dV}{dt}\Delta t \ll V$ . However, the error scaling becomes quadratic in  $\Delta t$  in this case [63]. The numerical solver was built with self-written C code and an implementation of FFTW [64]. The two major computation steps are the Fourier transform and matrix multiplication. Both tasks are suited for parallelization and yield a major speed up. Imaginary quadratic potentials were employed as absorbing boundaries to avoid reflections [65]. More sophisticated methods are available but for our purposes it works sufficiently well. For numerical stability we ensure that the time increment is below a certain value

$$\Delta t < \frac{\hbar\pi}{3V_{\max}}, \quad (7.1)$$

depending on the maximal potential energy [62]. We work with a Hamiltonian in length gauge without the  $1/c$ -corrections, but a possible implementation of magnetic fields for the split-operator method is given in [66] and in Appendix B.1. The physical parameters are chosen according to setting 2 in Table 5.1. The wavefunction propagation will advance with  $\Delta t = 0.1$  a.u. and the grid parameters are summarized in Table 7.2. For all results a simulated time of three laser periods was used.

| Direction | Grid points | Min [a.u.] | Max [a.u.]       | Stepsize $\Delta$ [a.u.] |
|-----------|-------------|------------|------------------|--------------------------|
| x         | 384         | -40        | $40 - \Delta x$  | 0.208                    |
| y         | 384         | -40        | $40 - \Delta y$  | 0.208                    |
| z         | 1152        | -100       | $100 - \Delta z$ | 0.174                    |

Table 7.2: The cartesian grid parameters are given for each direction. The resulting resolutions are approximately equal to the soft-core length scale  $r_0$  from Section 7.2.1. The total number of grid points is approximately  $1.7 \times 10^8 \approx 1.3 \times 2^{27}$ .

### 7.2.1 Coulomb potential

The Coulomb potential has a singularity at  $r = 0$  and poses a problem in numerical applications due to this divergence. Therefore, smoothed potentials (or “soft-core” potentials) are used that converge to a finite value for  $r \rightarrow 0$ . The potential form used for this work reads

$$V_c(r) = -\frac{1}{(r^4 + r_0^4)^{1/4}} \quad (7.2)$$

and has a finite value at  $r = 0$ , namely  $V_c(0) = -1/r_0$ .

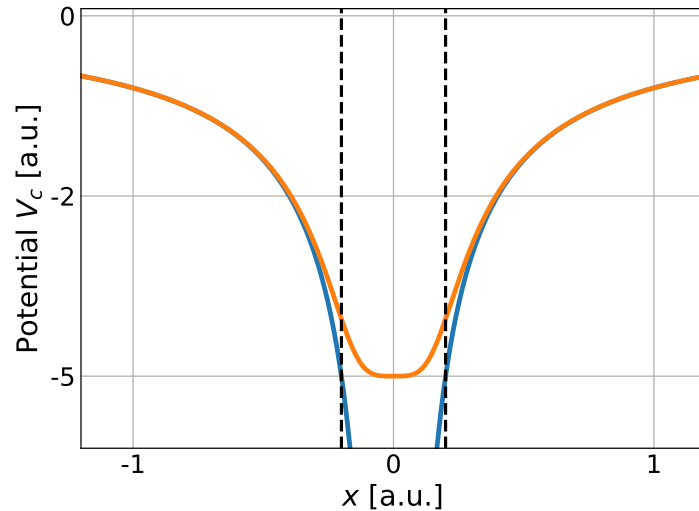


Figure 7.8: A smoothed potential (orange) is compared to the real Coulomb potential (blue) for length parameter  $r_0 = 0.2$  a.u., indicated by the vertical dashed lines. They are in good agreement for distances  $r \geq r_0$ .

The grid resolutions sets an upper bound for the length scale  $r_0$  under the condition of having only a minimal number of grid points with a potential significantly deviating from the real Coulomb potential. For  $r_0 \approx \Delta x_i$  and a grid involving the origin ( $x = 0, y = 0, z = 0$ ) this number is exactly one. A value of  $r_0 = 0.2$  is used for all simulations and is of the order of the spatial step size in each direction.

The ground state wavefunction and energy is estimated with the variational principle [67] under the use of the Hydrogen ground state wavefunction  $\psi_g = \exp(iI_{p,\text{eff}} t) \exp(-r/a_{\text{eff}})/(\pi a_{\text{eff}}^3)^{1/2}$  with tunable width  $a_{\text{eff}} \xrightarrow{r_0 \rightarrow 0} a_0 = 1$  a.u. as an ansatz wavefunction. The estimated upper bound for the ground state energy is  $I_{p,\text{eff}} \approx -0.47$  a.u. and has an associated width of  $a_{\text{eff}} \approx 1.086$  a.u. for the trial wavefunction. For the purpose of confirming our analytical results it is sufficiently close to the real Coulomb potential.

## 7.3 Results of simulation

The first half of this section examines the dynamics for initial wavepackets without orbital angular momentum ( $l = 0$ ) in the traditional approach and *scenario 2*. Subsequently, the second half explores the dynamics for *scenario 1* and *scenario 2* with twisted Volkov wavepackets ( $l = 1$ ). For all cases in the following we consider only the ground state  $\psi_g$  as the bound state in the wavefunction (4.3), i.e.,

$$\psi_b \longrightarrow \psi_g. \quad (7.3)$$

It is estimated with the trial wavefunction from Section 7.2.1.

### 7.3.1 Traditional HHG with initially populated ground state

In order to verify the accuracy of the quantum solver the traditional HHG approach with a neutral Hydrogen atom in its ground state ( $c_g(0) = 1$ ) was chosen as the first simulation. Figure 7.9 shows a cross section of the wavepacket in time and the dipole acceleration with its associated

spectrum. The wavefunction modulus  $|\psi|$  shows returning, as well as fully ionized parts of the free part of the electron. The dipole acceleration and the spectrum show only dynamics in the  $z$ -component and the transverse components are zero for all times. A clear HHG signal can be identified with a typical cutoff around  $I_p + 3.17U_p$  and, therefore, the operability of the quantum solver is confirmed.

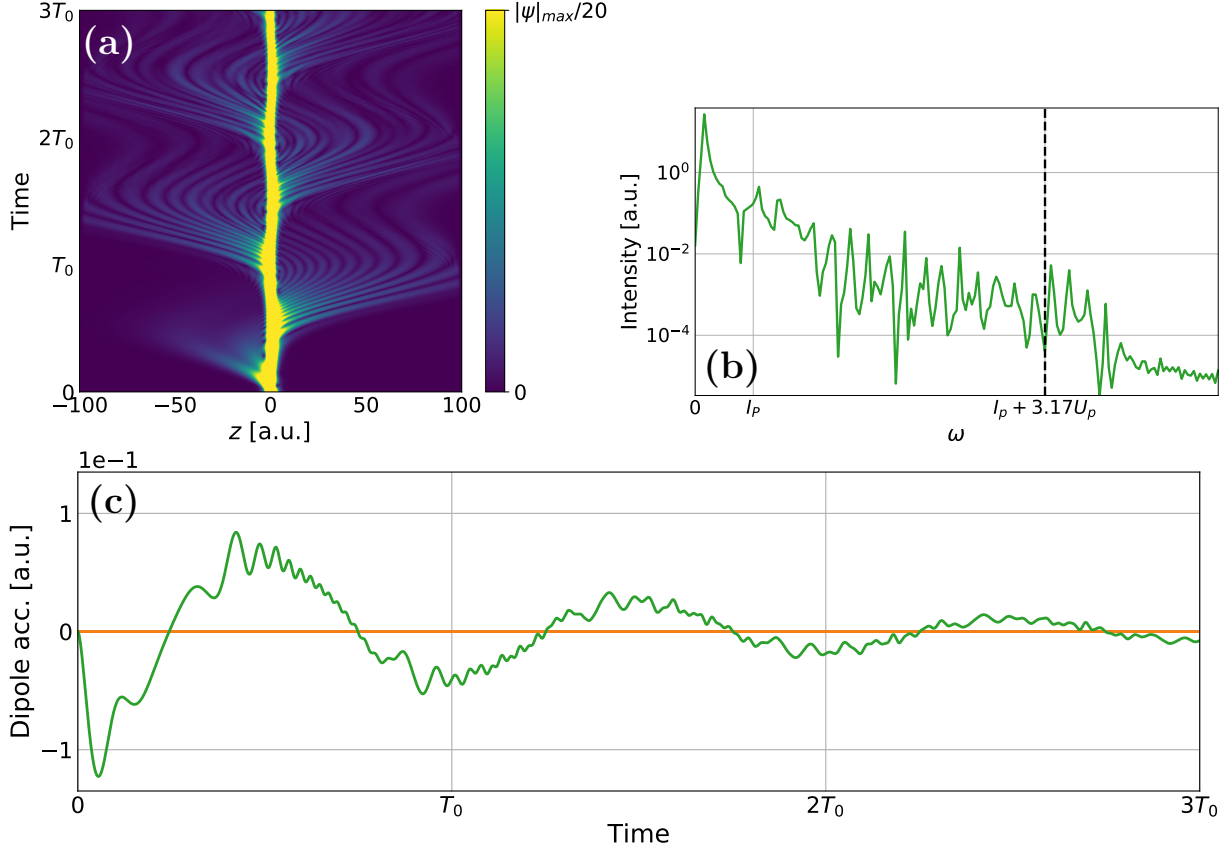


Figure 7.9: The simulation results for the traditional HHG approach are shown in this figure. The wavefunction modulus  $|\psi(0, 0, z, t)|$  is presented in the upper left plot (a). The color-scale is clipped at a fraction (0.05) of the maximum value of the modulus for a better visual contrast. For the spectrum (b) and the dipole acceleration (c) the colors were chosen such that  $x$ -,  $y$ - and  $z$ -components correspond to blue, orange and green, respectively. However, the transverse components are zero and not visible in a semilogarithmic plot (b). The blue line is covered by the orange line in the lower plot (c). The theoretical cutoff  $I_p + 3.17U_p$  is indicated by a black dashed line.

### 7.3.2 HHG with fully ionized atom and Gaussian wavepacket

A free Gaussian Volkov wavepacket and a fully ionized core  $c_g(0) = 0$  correspond to the system investigated in one dimension in reference [29] and is referred to by us as *scenario 2*. Their findings can be qualitatively confirmed for the three-dimensional system and the dipole acceleration and the corresponding spectrum have the same profile (see Figure 7.11). There is only a contribution in the  $z$ -component of the dipole acceleration, similar to the simulation above. The spectrum shows all typical characteristics of a HHG spectrum and has a cutoff at approximately  $I_p + 2U_p$ . Furthermore, the effect of Coulomb focusing on the wavefunction can be seen in Figure 7.10.

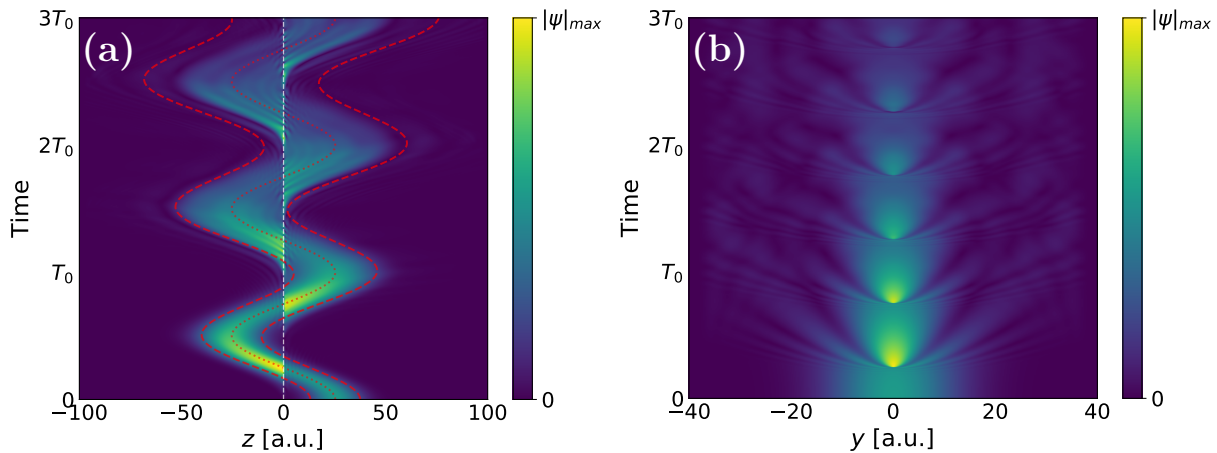


Figure 7.10: The wavefunction evolution in time is shown for  $|\psi(0,0,z,t)|$  on the left (a) and for  $|\psi(0,y,0,t)|$  on the right (b). The red lines correspond to the analytical form of the Gaussian Volkov wavefunction. The dotted line marks the center and the dashed lines show the wavepacket extension. The white dashed line indicates  $z = 0$  and serves as a guide for the eye.

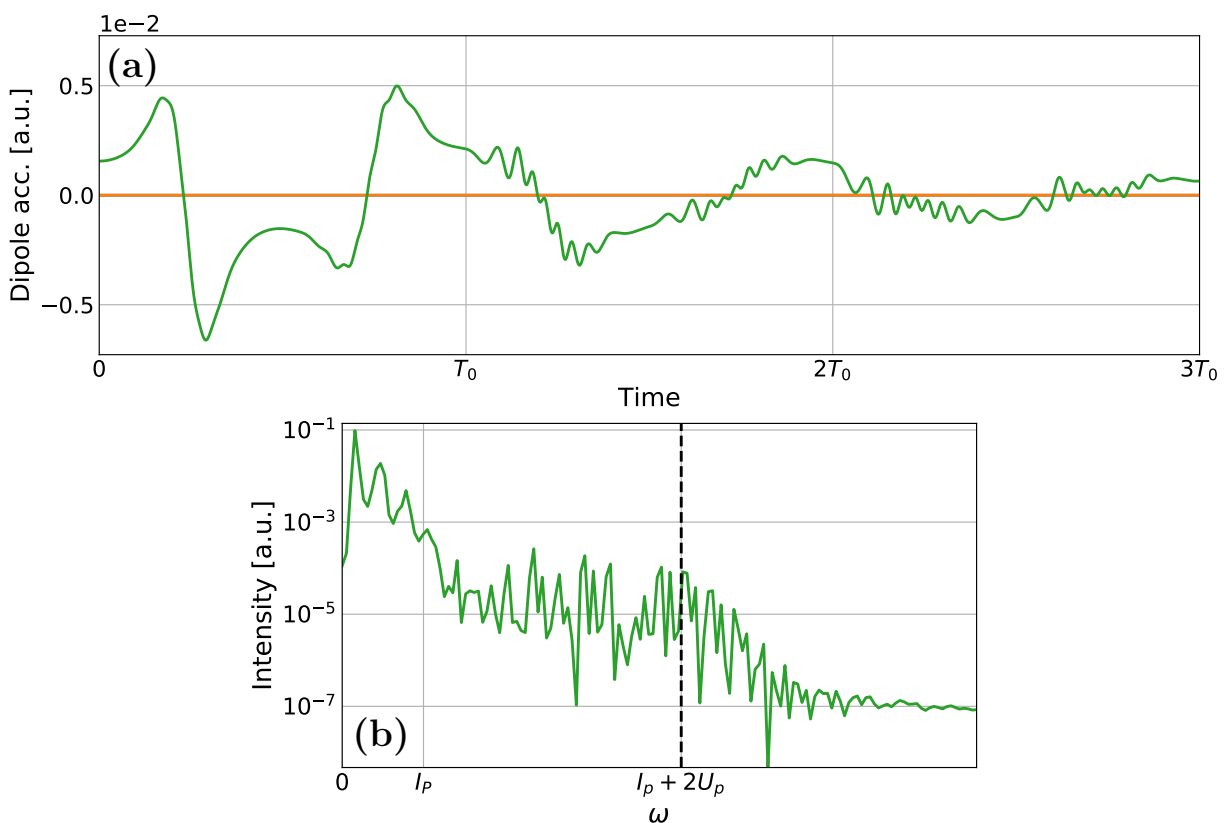


Figure 7.11: The dipole acceleration for the laser-assisted scattering scenario is shown in the upper plot (a) and the lower plot shows the spectrum (b). The theoretical cutoff at  $I_p + 2U_p$  is indicated by the black dashed line. The colors are chosen to be the same as in Figure 7.9. The blue line is covered by the orange line in the upper plot (a). The transverse components are zero and not visible in the semilogarithmic plot of the spectrum (b).

### 7.3.3 Twisted wavepackets

In the following we study the numerical results for twisted wavepackets, depicted in Figure 7.12, for *scenario 1* and *scenario 2*. For the use of twisted wavepackets we have to ensure that the structure is reasonably well resolved by the grid resolution. This corresponds to the factor  $e^{iA(t)z}$  and implies an upper bound for the spacing  $\Delta z < \frac{\pi}{A_0}$  between two grid points in  $z$ -direction.

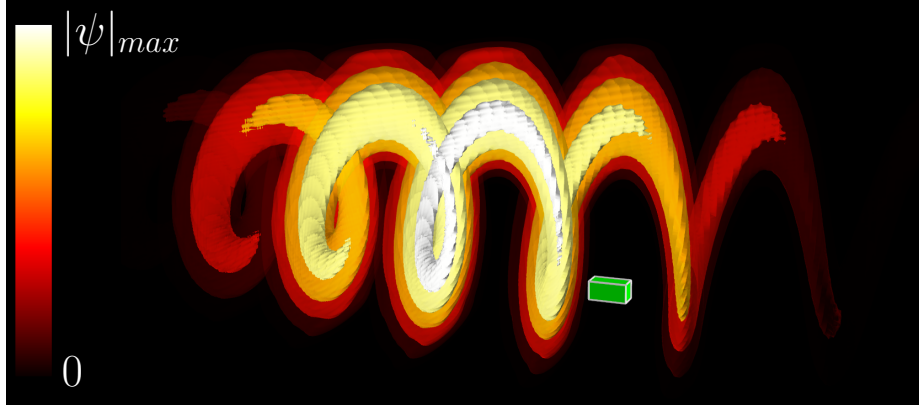


Figure 7.12: The wavefront of a twisted wavepacket extracted from the quantum simulation for  $A(t) = \max$  shows the vortex character. Its transparency scales with the amplitude and is color-coded as well. The green cuboid represents  $10 \times 10 \times 10$  unit cells on the grid and is shown for comparison.

#### Scenario 1

The first simulation with a twisted electron is done for *scenario 1*. The initial coefficients are chosen as  $c_g(0) = \sqrt{0.1}$  and  $c_T(0) = \sqrt{0.9}$ . The cross sections through the wavefunction moving in time is presented in Figure 7.13 and shows the ring like structure in the transverse plane.

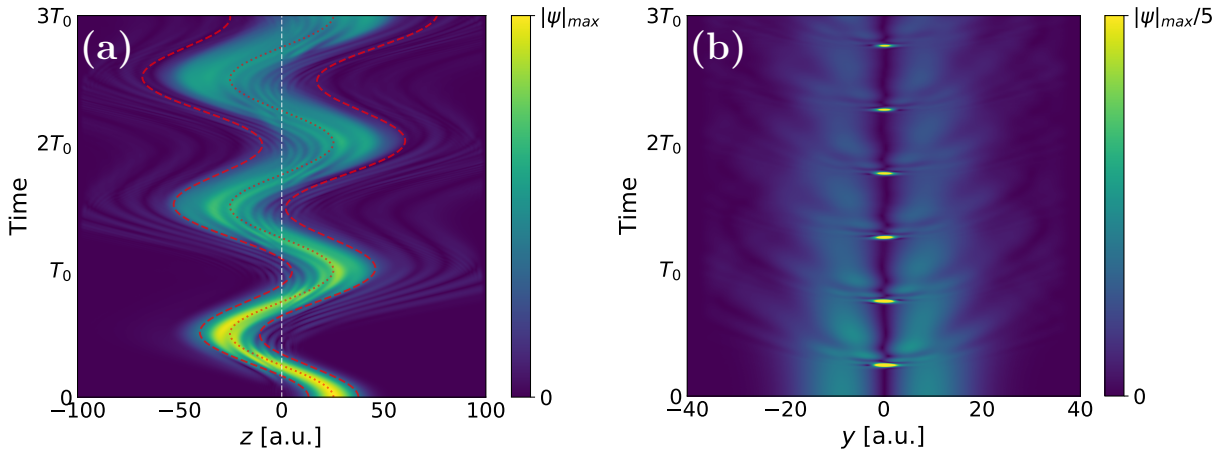


Figure 7.13: The wavefunction evolution in time is shown for  $|\psi(0, \rho_{ring}(0), z, t)|$  on the left (a) and for  $|\psi(0, y, 0, t)|$  on the right (b). In the right plot (b) the color-scale is clipped at a fraction (0.2) of the maximum value of the modulus for a better visual contrast and, hence, shows the vanishing probability density at  $\rho = 0$ . Even though less visible, the left plot (a) exhibits the same shapes as in Figure 7.9. The red lines correspond to the analytical form of the twisted wavepacket. The dotted line marks the center and the dashed lines show the extension. The white dashed line indicates  $z = 0$  and serves as a guide for the eye.

The resulting dipole acceleration and its spectrum is depicted in Figure 7.14. For this case all components of  $\vec{a}(t)$  are nonzero and the transverse acceleration curves can be recognized to be similar in shape to the ones obtained in Section 7.1. The longitudinal component curve is almost identical to the one in Figure 7.9. As the spectral intensity plot confirms, a mixing of HHG dynamics happens due to the nonzero initial ground state occupation probability. The traditional HHG occurs as well and, hence, a cutoff at  $I_p + 3.17U_p$  is observed. More importantly, we see the predicted peaks in the emission spectrum for the transverse components of the dipole acceleration and the expected cutoff at  $I_p + 2U_p$ .

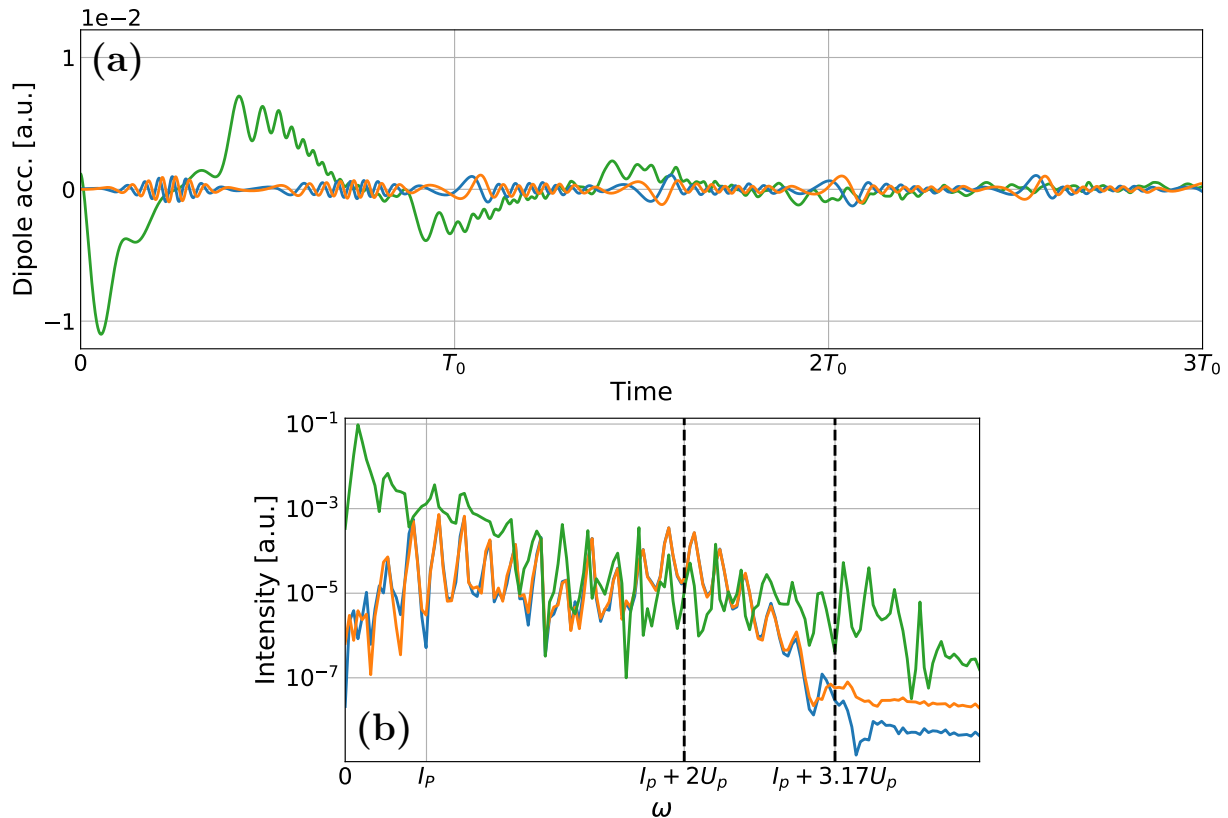


Figure 7.14: The dipole acceleration is shown in the upper plot (a) and the lower plot shows the spectrum (b). The transverse components are blue and orange for the  $x$ - and  $y$ -direction, respectively, while the longitudinal component is green. Furthermore, two dashed black lines in the spectrum indicate the two theoretical cutoff frequencies  $I_p + 2U_p$  and  $I_p + 3.17U_p$ .

### Scenario 1 with impact parameter $b$

Next, the effect of a nonzero impact parameter is simulated. We chose the transverse shift to be  $b = 5$  in  $y$ -direction. The initial coefficients are the same as above, namely  $c_g(0) = \sqrt{0.1}$  and  $c_T(0) = \sqrt{0.9}$ . The evolution of the wavepacket in time is shown in Figure 7.15. The motion in  $z$ -direction is similar to its counterpart in Figure 7.13, but the vortex center moves in  $y$ -direction due to the focusing effect of the Coulomb potential. We further support this finding with the expectation value of the position operator  $\langle \hat{r} \rangle(t)$  in Figure 7.16. The  $y$ -component shows the initial offset by an impact parameter  $b = 5$ . Subsequently, the wavepacket experiences the Coulomb force and is drawn toward the center in the transverse plane and eventually the center position has even negative values for  $\langle \hat{y} \rangle$ . Additionally, the  $x$ -component shows a displacement from the center as well. This behavior is absent for the equivalent situation with a Gaussian

wavepacket ( $l = 0$ ,  $b = 5$ ), also shown in Figure 7.16. We argue that the transverse shift due to the magnetic field of the laser mode is smaller than this effect and would not have a significant influence on the dynamics if it were included in the simulation.

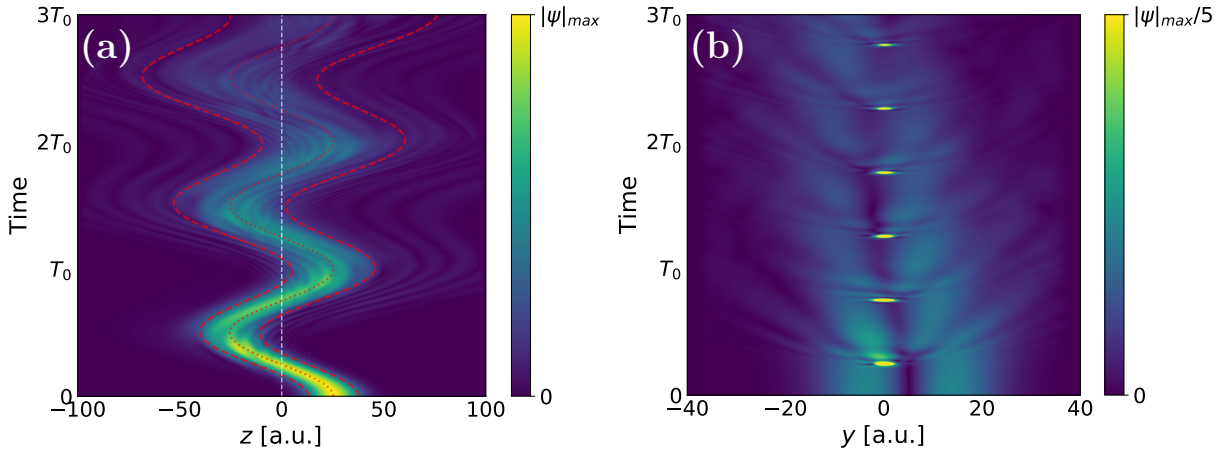


Figure 7.15: The wavefunction evolution in time is shown for  $|\psi(0, \rho_{ring}(0) + b, z, t)|$  on the left (a) and for  $|\psi(0, y, 0, t)|$  on the right (b). In the right plot (b) the color-scale is clipped at a fraction (0.2) of the maximum value of the modulus for a better visual contrast. The impact parameter  $b = 5$  can be identified for  $t = 0$  (b). The red lines correspond to the analytical form of the twisted wavepacket. The dotted line marks the center and the dashed lines show the extension. The white dashed line indicates  $z = 0$  and serves as a guide for the eye.

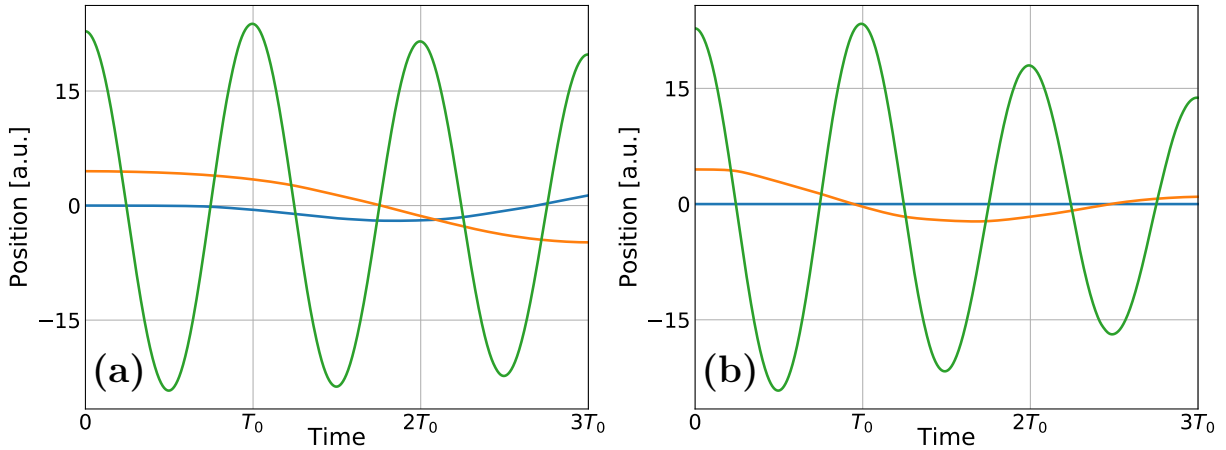


Figure 7.16: The expectation value of the position operator in an off-axis scattering scenario is shown for a twisted wavepacket ( $l = 1$ ) on the left (a) and for a Gaussian wavepacket ( $l = 0$ ) on the right (b). The quiver motion due to the electric field is imprinted in the  $z$ -component (green line) of the expectation value of the position operator. The dynamics in the transverse directions is indicated by the blue and green line for  $\langle \hat{x} \rangle$  and  $\langle \hat{y} \rangle$ , respectively.

Figure 7.17 displays the resulting dipole acceleration and its spectrum. A resemblance to the results in Figure 7.4 can be seen. The  $z$ -component exhibits large oscillations at the same time as the transverse components. Moreover, for  $t < T_0/2$ , the amplitudes of the transverse oscillations are slightly different. Again, mixing of different HHG dynamics occurs in the spectrum and  $S_z$



displays two cutoffs at  $I_p + 2U_p$  and  $I_p + 3.17U_p$ . The latter cutoff is due to the initial finite ground state population probability. The plateau region associated with the smaller cutoff is due to the broken symmetry of the system. The occurrence of  $\omega_0$ -shifted peak frequencies around the smaller cutoff, presented in Section 7.1, is reproduced as well. However, due to the mixing of HHG spectra from the traditional approach and the laser-assisted scattering scenario, the peak structure in the lower frequency part of the plateau is less pronounced.

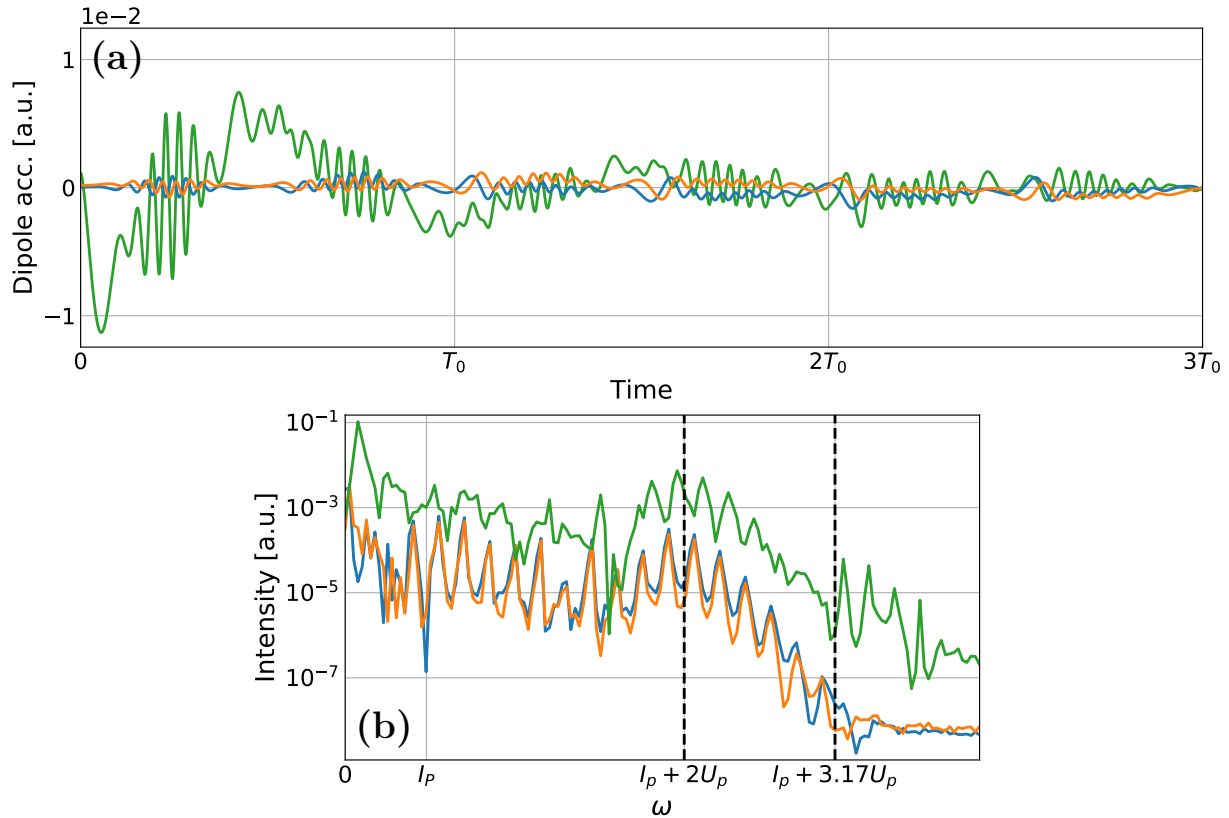


Figure 7.17: The dipole acceleration is shown in the upper plot (a) and the lower plot shows the spectrum for the simulated off-axis scattering of a twisted electron (b). The transverse components are blue and orange for the  $x$ - and  $y$ -direction, respectively, while the longitudinal component is green. Furthermore, two dashed black lines in the spectrum indicate the two theoretical cutoff frequencies  $I_p + 2U_p$  and  $I_p + 3.17U_p$ .

### Scenario 2

The next simulation for the twisted electron is the equivalent of the HHG with a fully ionized ion in Section 7.3.2 with  $c_T(0) = 1$ . The results are shown in Figures 7.18 and 7.19.

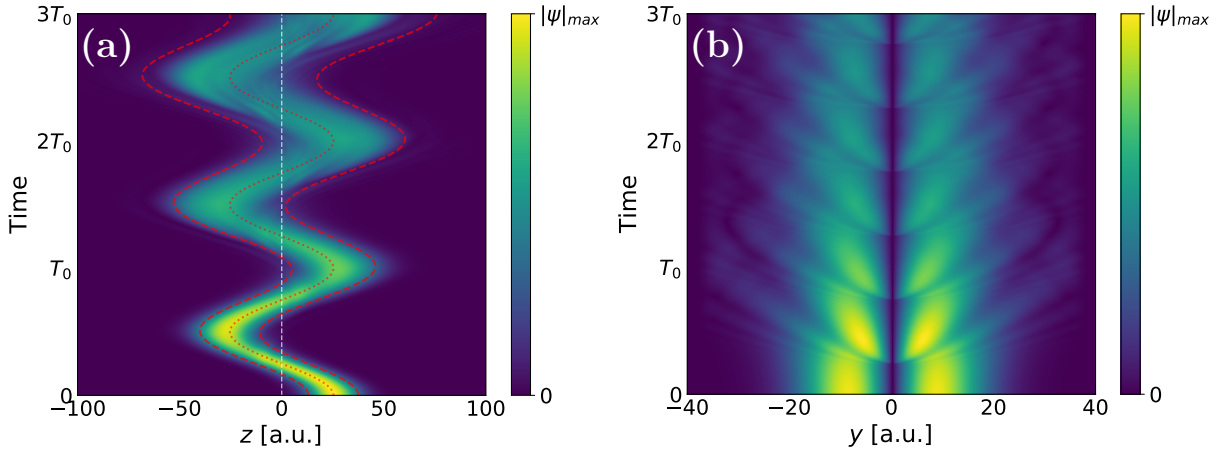


Figure 7.18: The wavefunction evolution in time is shown for  $|\psi(0, \rho_{ring}(0), z, t)|$  on the left and for  $|\psi(0, y, 0, t)|$  on the right. The red lines correspond to the analytical form of the twisted wavepacket. The dotted line marks the center and the dashed lines show the extension. The white dashed line indicates  $z = 0$  and serves as a guide for the eye.

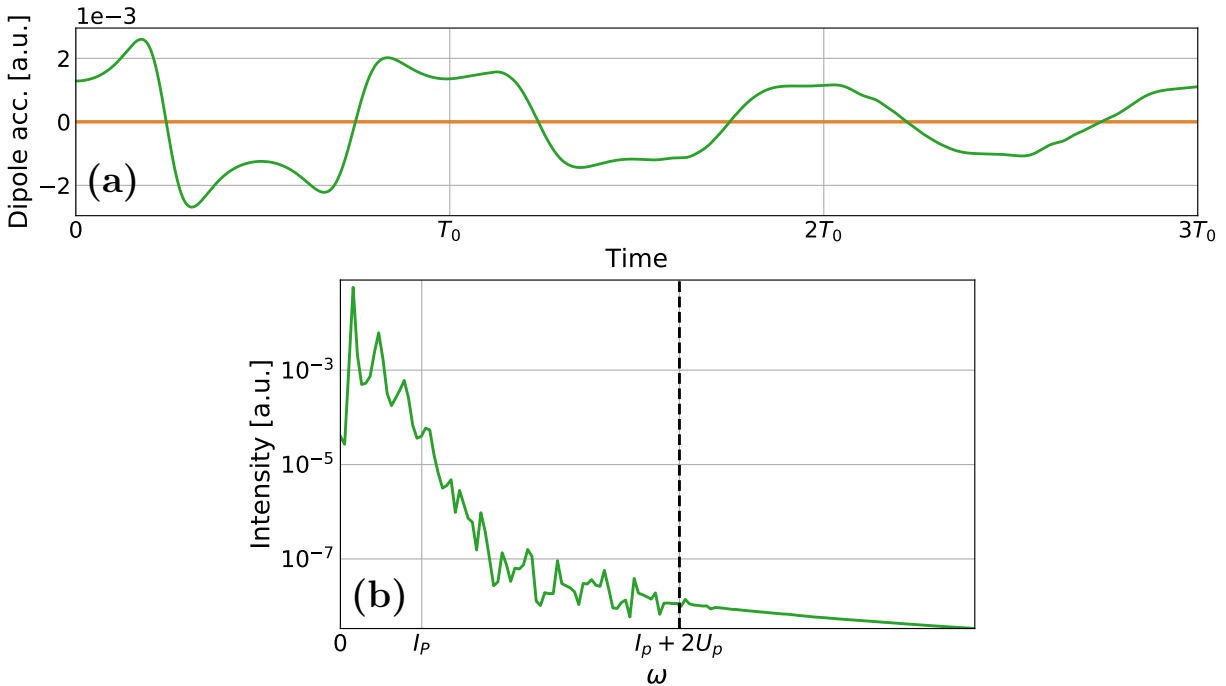


Figure 7.19: The dipole acceleration is shown in the upper plot (a) and the lower plot shows the spectrum (b). The transverse components are blue and orange for the  $x$ - and  $y$ -direction, respectively, while the longitudinal component is green. The blue line is covered by the orange line in the upper plot (a). The transverse components are zero and not visible in a semilogarithmic plot (b). The dashed black line in the spectrum indicates the theoretical cutoff frequency  $I_p + 2U_p$ .

Surprisingly and in contrast to *scenario 1*, high harmonic generation does not appear in the spectrum for the transverse components. Also the  $z$ -component of the dipole acceleration does not exhibit the oscillations expected from Figure 7.19. Additionally, the cross section of the full wavefunction in Figure 7.18 shows that the wavefunction modulus at  $r = 0$  is always zero, in other words, there is no ground state population at all. Both observations reveal deficiencies of the dipole acceleration formalism and the usage of a Hamiltonian without the coupling to the quantized radiation field.

### 7.3.4 Discussion

The dipole acceleration with wavefunction splitting (6.11) shows that there can only be high harmonics as long as both states are populated. Regardless of the degree of atomic ionization, the HHG recombination process is a spontaneous emission of one high-energetic photon upon first recollision. Higher-order processes have a lower probability to occur. Spontaneous emission is a purely quantum mechanical process [68] and has no classical analogue. The semiclassical approach (2.2) is not adequate in the limit of vanishing occupation of one state. Not only the limiting behavior is incorrect, but also the magnitude of the emission is only correctly given if the population of the state, in which is recombined to, is close to unity [69]. According to reference [69] the ratio of the semiclassical (SC) and quantum electrodynamical (QED) emission intensity

$$\frac{I_{\text{SC}}}{I_{\text{QED}}} = |c_b^2| \xrightarrow{|c_b|^2 \rightarrow 0} 0 \quad (7.4)$$

is linearly related to the occupation probability. In the work of Bogatskaya et al. it is furthermore stressed that continuum-continuum transitions in the semiclassical dipole formalism do not represent the physical reality of Bremsstrahlung, at least when no laser field is present. However, we shall only be concerned with bound-continuum transitions in this work. The qualitative structure in the emission spectrum is still conserved as long as bound and continuum states are populated. Yet, quantitative results should be taken with a grain of salt.

The detuning of the laser field from the high harmonic transitions is very large and, effectively, its interaction does not induce any transfer to bound states. Hence, the only physical mechanism to change the state population is via spontaneous recombination. Yet, some of the full quantum simulations seem to emulate this behavior even though no couplings to quantized electromagnetic field modes are present in the Hamiltonian of Equation (4.2). The subtle reason is the choice of the initial state. The smoothed Coulomb potential is of long-range nature and, thus, without the knowledge of the exact eigenstates, an arbitrary initial state will most likely contain components of bound states in its superposition. The situation becomes more complex with a time-dependent driving potential, but we argue hand-wavily that the capture of the wavefunction at the binding potential is due to the same reason. The total wavefunction will not be orthogonal to the ground state in that case

$$\langle \psi_g(t) | \psi(t) \rangle \neq 0, \quad (7.5)$$

for example for a Gaussian wavepacket at  $t = 0$ . The situation is different if the initial state is twisted with a quantization axis pointing directly toward the center of the cylindrical symmetric binding potential. Here, the laser field formally breaks the spherical symmetry of the Coulomb potential. In such a case both, the Hamiltonian and the full wavefunction, are cylindrical symmetric, in the sense that they are invariant under a rotation around the quantization axis of the

vortex [49]. A global phase transformation does not change the physical state of the system. Hence, the propagated wavefunction  $\psi(\vec{r}, t)$  will always have vortex character. Mathematically, the Hamiltonian and the angular momentum operator in  $z$ -direction commute,  $[\hat{H}, \hat{L}_z] = 0$ . This commutation relation ensures that the wavepacket will always be an eigenstate of  $\hat{L}_z$  with the same quantum number  $l$  for all times if the state was initially in an eigenstate with the same orbital angular momentum. The Hamiltonian is block diagonal in the basis of  $\hat{L}_z$ -eigenstates and therefore does not couple subspaces of different orbital quantum number. We will quickly prove that the ground state of the binding potential must be a state with zero orbital angular momentum along the symmetry axis.

For the following we assume that the potential has at least one (quasi-)bound eigenstate. This will be approximately true if the ionization time in the electric field is very long or the numerical grid does not extend to regions where the combined potential energy is lower than the binding energy. It can be shown that the ground state must be real (up to some global phase) and positive everywhere [70]. This also renders the ground state non-degenerate. Due to the symmetry of the Hamiltonian it must be a simultaneous eigenstate of the rotation operator under which the system is invariant and must have a factor  $e^{im\varphi}$ . The ground state can only be real for  $m = 0$ . Physically speaking, angular momentum gives an additional contribution to the kinetic energy and is unfavorable for a minimal energy state. It follows that the ground state and the propagated twisted wavefunction must be orthogonal for all times, i.e.,

$$\langle \psi_g(t) | \psi_T(t) \rangle = 0. \quad (7.6)$$

The vortex wavepacket is not only orthogonal to the ground state, but to every state with any other orbital quantum number than  $l$ . Though, it is exactly these states with  $m = l \pm 1$  that give the interesting dynamics for the  $x$  and  $y$  component of the dipole acceleration. Due to non-population of such states the dipole acceleration will always be zero in the transverse direction. Only for excited bound states  $\psi_b \propto e^{im\varphi}$  with azimuthal quantum number  $m = l$  an overlap can happen. All  $m \neq 0$  states have a vanishing probability at  $r = 0$ , as it is the case in the simulation (Figure 7.18). Another implication is that the ground state can only be populated if the initial wavepacket has components with zero orbital angular momentum  $l = 0$  in its superposition, for example the Gaussian wavepacket (Figure 7.10). The situation is different, of course, for non-central collisions, since the rotational symmetry of the system around the  $z$ -axis is broken. This is the third major result of this work.

The full quantum simulation can accurately reflect tunneling, but is unreliable when spontaneous emission processes are important for the dynamics. Furthermore, the angular momentum transfer of one quantum  $\hbar$  to the emitted photon cannot be emulated. Bogatskaya et al. performed numerical simulations with a discrete set of quantized field modes coupled to the atomic system in order to investigate several strong-field scenarios and compared them to the dipole formalism [71, 72, 73]. Qualitative differences and limitations of the semiclassical approach were pointed out.

# 8 Quantum Electrodynamical Approach

The arguments at the end of the preceding chapter suggest that a better treatment of the process must involve the theory of quantum electrodynamics (QED). The coupling of the atomic system to the electromagnetic vacuum will be treated in first-order perturbation theory. It is this interaction that gives rise to couplings between subspaces of different orbital quantum number. The necessary foundations to describe spontaneous recombination are the field quantization and the resulting coupling term in the Hamiltonian for the electron. They will be introduced in Section 8.1. The dynamics of spontaneous emission processes is treated in first-order perturbation theory in Section 8.2. These concepts are then applied to derive an analytical approximation for the recombination probability for twisted electrons in Section 8.3. This quantity allows to obtain the associated emission spectrum, which we compare to the semiclassical formalism. The comparison is presented in Section 8.4 and the numerical results for the quantum electrodynamical spectrum are given in Section 8.5. We conclude this chapter with a possible application of this concept to the numerical quantum simulation in Section 8.6.

## 8.1 Theoretical groundwork

In this section we introduce the theoretical basis for a treatment of quantum electrodynamical processes with non-relativistic charged particles. The quantization of the electromagnetic field is briefly introduced in Section 8.1.1 and the interaction term for the coupling to the quantized radiation field is presented in Section 8.1.2. We will follow the canonical quantization procedure in Loudon's book [74].

### 8.1.1 Quantized electromagnetic field

To quantize the electromagnetic field known from classical electrodynamics it will be brought to a form that is already familiar from quantum mechanics, namely harmonic oscillators. This connection forms the basis for a recipe to promote the classical vector potential to an operator in terms of creation and annihilation operators. The procedure starts with the free Maxwell equations without any source terms

$$\vec{\nabla} \times \vec{E} = -\partial_t \vec{B}, \quad (8.1)$$

$$\varepsilon_0 \vec{\nabla} \cdot \vec{E} = 0, \quad (8.2)$$

$$\vec{\nabla} \cdot \vec{B} = 0, \quad (8.3)$$

$$\vec{\nabla} \times \vec{B} = \frac{\partial_t \vec{E}}{c^2}. \quad (8.4)$$

These equations can be reformulated with a scalar and a vector potential, namely  $\Phi$  and  $\vec{A}$  [75]. The electric and the magnetic field

$$\vec{E} = -\vec{\nabla}\Phi - \partial_t \vec{A}, \quad (8.5)$$

$$\vec{B} = \vec{\nabla} \times \vec{A} \quad (8.6)$$

are derivatives of these potentials. However, we chose the Coulomb gauge  $\vec{\nabla} \cdot \vec{A} = 0$  and see that the scalar potential can be set to zero ( $\Phi = 0$ ). From Equation (8.4) follows the wave equation

for the vector potential in free space

$$\vec{\nabla}^2 \vec{A} - \frac{1}{c^2} \partial_t^2 \vec{A} = 0. \quad (8.7)$$

A very large cubic volume with periodic boundary conditions and with length  $L$  is assumed. The vector potential is now expanded in possible Fourier modes

$$\vec{A}(\vec{r}, t) = \sum_{\vec{k}} \sum_{\lambda=1,2} \vec{\epsilon}_{\vec{k},\lambda} A_{\vec{k},\lambda}(\vec{r}, t), \quad (8.8)$$

where each component reads

$$A_{\vec{k},\lambda}(\vec{r}, t) = A_{\vec{k},\lambda}(t) e^{i\vec{k}\cdot\vec{r}} + A_{\vec{k},\lambda}^*(t) e^{-i\vec{k}\cdot\vec{r}}. \quad (8.9)$$

The wavevectors  $\vec{k}$  are determined by the length of each side of the volume and their components are

$$k_i = \frac{2\pi n_i}{L} \quad \text{for } i \in \{x, y, z\} \quad \text{and } n_i \in \mathbb{Z}. \quad (8.10)$$

The polarization vectors  $\vec{\epsilon}_{\vec{k},\lambda}$  are orthogonal for fixed  $\vec{k}$  and have unit length. The Coulomb gauge leads to the orthogonality to the wavevector

$$\vec{k} \cdot \vec{\epsilon}_{\vec{k},\lambda} = 0. \quad (8.11)$$

The governing equation for the time-dependent factors  $A_{\vec{k},\lambda}(t)$  follows from the insertion of (8.8) into (8.7), yielding

$$c^2 |\vec{k}|^2 A_{\vec{k},\lambda}(t) + \partial_t^2 A_{\vec{k},\lambda}(t) = 0. \quad (8.12)$$

It has the simple solution

$$A_{\vec{k},\lambda}(t) = A_{\vec{k},\lambda} e^{i\omega t} \quad (8.13)$$

with the dispersion relation  $\omega \equiv c|\vec{k}|$ . In order to make the connection to harmonic oscillators the total energy of the electric and the magnetic field

$$\mathcal{E} = \frac{1}{2} \int_{V=L^3} dV \left[ \varepsilon_0 \vec{E}^2 + \frac{1}{\mu_0} \vec{B}^2 \right] \quad (8.14)$$

is considered. These fields can be expressed in terms of the vector potential (8.8). We refer to reference [74] for the detailed calculation and just give the energy

$$\mathcal{E} = \sum_{\vec{k},\lambda} \varepsilon_0 V \omega^2 \left( A_{\vec{k},\lambda} A_{\vec{k},\lambda}^* + A_{\vec{k},\lambda}^* A_{\vec{k},\lambda} \right) \quad (8.15)$$

in terms of  $A_{\vec{k},\lambda}$ . Thus, the individual modes of the field are decoupled and each individual contribution is summed up to give the total energy. We compare Equation (8.15) with the Hamiltonian of a single harmonic oscillator

$$\hat{\mathcal{H}}_{osc} = \frac{1}{2} \hbar \omega \left( \hat{a} \hat{a}^\dagger + \hat{a}^\dagger \hat{a} \right). \quad (8.16)$$

The resemblance between (8.15) and (8.16) suggests that we can associate the complex coefficients  $A_{\vec{k},\lambda}$  and their complex conjugates with annihilation and creation operators, respectively, and express the total electromagnetic energy

$$\hat{H}_{em} = \frac{1}{2} \sum_{\vec{k},\lambda} \hbar\omega \left( \hat{a}_{\vec{k},\lambda} \hat{a}_{\vec{k},\lambda}^\dagger + \hat{a}_{\vec{k},\lambda}^\dagger \hat{a}_{\vec{k},\lambda} \right) \quad (8.17)$$

as the sum of uncoupled quantum harmonical oscillators. By comparison we can derive the appropriate scaling for the promotion to quantum mechanical operators, giving

$$A_{\vec{k},\lambda} \longrightarrow \sqrt{\frac{\hbar}{2\varepsilon_0 V \omega}} \hat{a}_{\vec{k},\lambda}. \quad (8.18)$$

The associated eigenstates will be denoted by  $|n_{\vec{k},\lambda}\rangle$  ( $n \in \mathbb{N}$ ) equivalent to the eigenstates of the harmonic oscillator. The lowest state is  $|0_{\vec{k},\lambda}\rangle$  and corresponds to zero photons in this particular mode. Finally, the quantized electromagnetic vector potential operator reads

$$\hat{A}(\vec{r}, t) = \sum_{\vec{k},\lambda} \underbrace{\sqrt{\frac{\hbar}{2\varepsilon_0 V \omega}} \left[ \hat{a}_{\vec{k},\lambda} e^{i(\vec{k}\cdot\vec{r}-\omega t)} + \hat{a}_{\vec{k},\lambda}^\dagger e^{-i(\vec{k}\cdot\vec{r}-\omega t)} \right]}_{\equiv \hat{A}_{\vec{k},\lambda}} \cdot \vec{\epsilon}_{\vec{k},\lambda}. \quad (8.19)$$

### 8.1.2 Interaction with charged particle

The coupling of a non-relativistic free (spinless) charged particle to the quantized radiation field is done via minimal coupling [74, 76]

$$\hat{H} = \frac{1}{2m_e} \left( \hat{\vec{p}} - q\hat{A} \right)^2. \quad (8.20)$$

Expanding the brackets and choosing the Coulomb gauge leads to two terms in the interaction Hamiltonian

$$\hat{H}_{\text{int}} = -\frac{q}{m_e} \hat{A} \cdot \hat{\vec{p}} + \frac{q^2}{2m_e} \hat{A}^2. \quad (8.21)$$

## 8.2 Spontaneous emission process

We follow reference [68] for the treatment of the spontaneous emission process. Consider a composite system of an atom and one radiation field mode with frequency  $\omega$  and polarization  $\vec{\epsilon}$ , which is initially in the vacuum state  $|0\rangle$ , i.e., no photons are present. A very fundamental process is the transition of excited atomic state  $|B\rangle$  to state  $|A\rangle$  under the emission of one photon

$$|B\rangle \otimes |0\rangle \longrightarrow |A\rangle \otimes |1\rangle. \quad (8.22)$$

The combined state is written as the direct product and is an element of the composite Hilbert space  $\mathcal{H}_{\text{atom}} \otimes \mathcal{H}_{\text{em}}$ . It is of perturbative nature, because the coupling is relatively weak, and thus we will neglect the quadratic term in  $\hat{H}_{\text{int}}$  and consider only one-photon processes in the following. This is equivalent to a first-order perturbation approach. In fact, neglecting the quadratic term is not an approximation for a one-photon transition, as it involves only products of creation and annihilation operators and can only induce changes in the photon number of zero or  $\pm 2$ .

In the context of atomic spectra the “dipole approximation” is referred to the expansion of the exponential factor  $e^{i\vec{k}\cdot\vec{r}}$  in the interaction Hamiltonian with the quantized electromagnetic field. For wavelengths larger than the Bohr radius  $a_0$  ( $c/\omega \gg a_0$ ) it can be safely approximated to be one, i.e.,  $e^{i\vec{k}\cdot\vec{r}} \approx 1$ . The critical frequency at which the approximation breaks down is

$$\hbar\omega_{\text{crit}} = \frac{\hbar c}{a_0} = \frac{m_e c^2}{137.0} = \frac{511 \text{ keV}}{137} \approx 3.7 \text{ keV} = 137.0 \text{ a.u.} \quad (8.23)$$

In this work all relevant frequencies are far away from this limit. Hence, the dipole approximation is employed here and the interaction Hamiltonian is

$$\hat{H}_{\text{int}}(t) = -\frac{q}{m_e} \sqrt{\frac{\hbar}{2\varepsilon_0\omega V}} \left[ \hat{a} e^{-i\omega t} + \hat{a}^\dagger e^{i\omega t} \right] \cdot (\hat{\vec{p}} \cdot \vec{\epsilon}). \quad (8.24)$$

The transition element for the emission of one photon with energy  $\hbar\omega$  and polarization  $\alpha$  for the transition from state  $|B\rangle$  to state  $|A\rangle$  can be written as

$$\left( \langle A| \otimes \langle 1| \right) \hat{H}_{\text{int}} \left( |B\rangle \otimes |0\rangle \right) = -\frac{q}{m_e} \sqrt{\frac{\hbar}{2\varepsilon_0\omega V}} \cdot \underbrace{\langle 1|\hat{a}^\dagger|0\rangle}_{=1} \cdot \langle A| e^{i\omega t} (\vec{\epsilon} \cdot \hat{\vec{p}}) |B\rangle \quad (8.25)$$

$$= -\frac{q}{m_e} \sqrt{\frac{\hbar}{2\varepsilon_0\omega V}} e^{i\omega t} \vec{\epsilon} \cdot \langle A|\hat{\vec{p}}|B\rangle. \quad (8.26)$$

### 8.2.1 Time-dependent perturbation theory - Time evolution of coefficients

In order to describe the dynamics of radiative recombination through spontaneous emission a treatment of the Schrödinger equation with the time-dependent coupling to the quantized radiation field is needed. Therefore we will introduce the first-order time-dependent perturbation theory [56]. We assume a full Hamiltonian given by

$$\hat{H} = \hat{H}_0 + \hat{H}_{\text{int}}. \quad (8.27)$$

The unperturbed eigenstates  $|\psi_n(t)\rangle$  of  $\hat{H}_0$  form a basis in Hilbert space and the general wavefunction can be written as a superposition of these eigenstates

$$|\Psi(t)\rangle = \sum_n c_n(t) |\psi_n(t)\rangle \quad (8.28)$$

with time-dependent coefficients  $c_n(t)$ . The Schrödinger equation leads to a system of coupled differential equations for the coefficients

$$\left( \hat{H}_0 + \hat{H}_{\text{int}} \right) |\Psi(t)\rangle = i\hbar\partial_t |\Psi(t)\rangle = \sum_n \left( i\hbar\dot{c}_n(t) |\psi_n(t)\rangle + c_n(t) \cdot i\hbar\partial_t |\psi_n(t)\rangle \right) \quad (8.29)$$

$$= \sum_n \left( i\hbar\dot{c}_n(t) |\psi_n(t)\rangle + \underbrace{c_n(t) \cdot \hat{H}_0}_{= \hat{H}_0 |\Psi(t)\rangle} |\psi_n(t)\rangle \right), \quad (8.30)$$

$$\Rightarrow \sum_n c_n(t) \hat{H}_{\text{int}} |\psi_n(t)\rangle = i\hbar \sum_n \dot{c}_n(t) |\psi_n(t)\rangle. \quad (8.31)$$

Assuming non-degeneracy, the differential equation for one particular coefficient can be obtained with a projection onto an eigenstate  $|\psi_m(t)\rangle$ , leading to

$$\dot{c}_m(t) = \frac{1}{i\hbar} \sum_n c_n(t) \langle \psi_m(t) | \hat{H}_{\text{int}} | \psi_n(t) \rangle. \quad (8.32)$$



For a given set of initial conditions, the full dynamics can be derived from the solution to these coupled equations. The situation at the beginning of this section can now be described analytically. In the following we assume that the atomic system has only two states and that there can only be one quantum of light at most. The coupled equations read

$$\dot{c}_{A,1}(t) = \frac{1}{i\hbar} c_{B,0}(t) \cdot \left(-\frac{q}{m_e}\right) \sqrt{\frac{\hbar}{2\varepsilon_0\omega V}} e^{i\omega t} \vec{\epsilon} \cdot \langle A|\hat{p}|B\rangle, \quad (8.33)$$

$$\dot{c}_{B,0}(t) = \frac{1}{i\hbar} c_{A,1}(t) \cdot \left(-\frac{q}{m_e}\right) \sqrt{\frac{\hbar}{2\varepsilon_0\omega V}} e^{-i\omega t} \vec{\epsilon} \cdot \langle B|\hat{p}|A\rangle, \quad (8.34)$$

and describe the absorption and emission process. Note that the interaction Hamiltonian for the absorption is the complex conjugate of (8.26). If the system is initially in the combined state of B and the electromagnetic vacuum, namely  $c_{B,0}(0) = 1$  and  $c_{A,1}(0) = 0$ , then for short times an approximation of  $c_{B,0} \simeq 1$  to be constant will be valid. The equations decouple in this case and the probability to find the system in state A with one photon present is given by

$$|c_{A,1}(t)|^2 \approx \frac{q^2}{2\hbar m_e^2 \varepsilon_0 \omega V} \left| \vec{\epsilon} \cdot \int_0^t dt' e^{i\omega t'} \langle A|\hat{p}|B\rangle \right|^2. \quad (8.35)$$

### 8.3 Radiative recombination

In general, the electromagnetic environment has not only one, but an infinite number of modes and all possible transitions have to be taken into account. In the case of the strongly driven twisted electron one mode is already populated with an exceedingly large number of photons, namely the laser mode. The creation of a photon in a field mode that is not in the vacuum state is called stimulated emission. However, we will neglect it in the following for three reasons. First, the laser frequency is far away from the HHG plateau and emission in this mode is not of interest. Second, the laser frequency is far detuned ( $\omega_0 \ll I_p$ ) and does not give a significant contribution. Last, the transition element vanishes for central collisions of twisted electrons with the ground state  $\psi_g$

$$\vec{\epsilon}_z \cdot \langle \psi_g|\hat{p}|\psi_T\rangle \propto \int d\varphi e^{il\varphi} = 0, \quad \text{for } l \neq 0. \quad (8.36)$$

In the following this particular mode will be excluded from summations or integrations over all field modes. For the sake of convenience the combined index  $\mathbf{k} \equiv \{\vec{k}, \lambda\}$  is introduced.

The wavefunction splitting approach in this thesis makes the atomic system effectively a two-level system. The drawbacks of this approach, the possible non-orthogonality and non-completeness already mentioned in Section 4.2, might seem unfavorable in the light of the derivation of the preceding section. Nonetheless, with a leap of faith we assume the formalism to hold approximately and to yield better results than the semiclassical dipole formalism. Now the full wavefunction reads

$$|\psi\rangle = c_{T,0}(|\psi_T\rangle \otimes |0\rangle) + \sum_{\mathbf{k}} c_{b,\mathbf{k}}(|\psi_b\rangle \otimes |1_{\mathbf{k}}\rangle). \quad (8.37)$$

The result of Equation (5.40) can be used to express the transition element as

$$\begin{aligned} \langle \psi_b|\hat{p}|\psi_T\rangle &= \int dV \psi_b^* \psi_T \left[ \vec{\epsilon}_z \left( -qA + i\hbar \frac{z - r_{\omega_0}}{\sigma_\alpha} \cdot (1 - i\tau_\alpha) \right) \right. \\ &\quad \left. + \vec{\epsilon}_\varphi \cdot \frac{\hbar l}{\rho} + \vec{\epsilon}_\rho \left( -i \frac{\hbar l}{\rho} + i\hbar \frac{\rho}{\sigma_\beta} \cdot (1 - i\tau_\beta) \right) \right]. \end{aligned} \quad (8.38)$$

Its evaluation can be readily performed with the integral formula  $I$  (Appendix B.4). The calculation becomes even easier if both wavefunctions are known in momentum space. In order to obtain the spectral intensity for one particular frequency the individual transition probabilities have to be summed over all emission directions  $\vec{e}_k$  and polarizations  $\vec{e}_{\vec{k},\lambda}$  ( $\lambda = 1, 2$ ). This leads to the probability

$$P_{b,\omega}(t) \equiv \int d\Omega_k \sum_{\lambda} |c_{b,k}(t)|^2 = \frac{q^2}{2\hbar m_e^2 \varepsilon_0 \omega V} \int d\Omega_k \sum_{\lambda} \left| \vec{e}_{\vec{k},\lambda} \cdot \int_0^t dt' e^{i\omega t'} c_{T,0} \langle \psi_b | \hat{p} | \psi_T \rangle \right|^2 \quad (8.39)$$

$$= \frac{4\pi q^2}{3\hbar m_e^2 \varepsilon_0 \omega V} \left| \int_0^t dt' e^{i\omega t'} c_{T,0} \langle \psi_b | \hat{p} | \psi_T \rangle \right|^2 \quad (8.40)$$

of having a photon with frequency  $\omega$ . We formally kept the coefficient  $c_{T,0}(t)$  and assumed  $c_{b,k}(0) = 0$ . The integration and summation give a geometrical factor of  $8\pi/3$ , which is calculated in Appendix B.5.

## 8.4 Connection to dipole acceleration formalism

The total radiated energy (2.12) in dipole velocity form and with  $\varepsilon_0 \mu_0 c^2 = 1$  reads

$$\begin{aligned} \mathcal{E}_{\text{SC,em}} &= \frac{q^2}{3\pi \varepsilon_0 c^3 m_e^2} \int_0^\infty d\omega \omega^2 |\tilde{p}(\omega)|^2 \\ &\stackrel{\text{SPA}}{\approx} \frac{q^2}{3\pi \varepsilon_0 c^3 m_e^2} \int_0^\infty d\omega \omega^2 \left| \frac{1}{\sqrt{2\pi}} \int_{-\infty}^\infty dt e^{i\omega t} c_b^*(t) c_T(t) \langle \psi_b(t) | \hat{p} | \psi_T(t) \rangle \right|^2. \end{aligned} \quad (8.41)$$

The dipole velocity was expressed with the momentum operator  $\frac{q}{m_e} \langle \hat{p} \rangle = \frac{d}{dt} \langle q\hat{r} \rangle$ . We neglect the contribution from  $\langle \psi_T | \hat{p} | \psi_T \rangle$  because it does not correspond to the recombination process but to continuum-continuum transitions and will not have any significance for the HHG plateau. The bound state contribution  $\langle \psi_b | \hat{p} | \psi_b \rangle = 0$  is zero (Appendix C.2). We will compare this expression to the total energy amount in the radiation field

$$\mathcal{E}_{\text{QED,em}} \equiv \sum_{\mathbf{k}} \hbar\omega \langle \hat{n}_{\mathbf{k}} \rangle \quad (8.42)$$

without the laser field. Furthermore, we set the origin of the energy scale to the electromagnetic vacuum energy term  $\sum_{\mathbf{k}} \hbar\omega/2$ . The sum in (8.42) can be converted to an integral [74]

$$\sum_{\mathbf{k}} \longrightarrow \frac{V}{(2\pi)^3} \int_0^\infty d\omega \frac{\omega^2}{c^3} \int_{\Omega_{\mathbf{k}}} d\Omega_k \sum_{\lambda}. \quad (8.43)$$

The expectation value of the photon number operator  $\hat{n}_{\mathbf{k}}$  corresponds simply to  $|c_{b,\mathbf{k}}|^2$ . Hence, we can express the total energy as

$$\mathcal{E}_{\text{QED,em}} = \frac{V}{(2\pi)^3} \int_0^\infty d\omega \frac{\omega^2}{c^3} \cdot \hbar\omega \cdot P_{b,\omega} \quad (8.44)$$

$$= \frac{q^2}{3\varepsilon_0 \pi c^3 m_e^2} \int_0^\infty d\omega \omega^2 \left| \frac{1}{\sqrt{2\pi}} \int_{-\infty}^\infty dt e^{i\omega t} c_{T,0}(t) \langle \psi_b(t) | \hat{p} | \psi_T(t) \rangle \right|^2 \quad (8.45)$$

and set the time integration limits in (8.40) to plus and minus infinity. By comparing the last line with Equation (8.41) the linear dependence of the semiclassical intensity on the bound state

population becomes clear. If the coefficients  $c_i$  are approximated to be constant, then the result

$$\frac{\mathcal{E}_{\text{SC,em}}}{\mathcal{E}_{\text{QED,em}}} = |c_b|^2 \quad (8.46)$$

from reference [69] follows. This shows also that full ionization leads to a higher HHG intensity in a single-atom framework. Additionally, the dipole formalism works well for traditional HHG in which the degree of ionization is negligible and  $c_b(t) \approx 1$ . We define the QED spectrum, similar to the semiclassical one, as

$$S_{\text{QED}}(\omega) \equiv \frac{q^2 \cdot \omega^2}{m_e^2} \left| \frac{1}{\sqrt{2\pi}} \int_0^t dt' e^{i\omega t'} c_{\text{T},0} \langle \psi_b | \hat{\vec{p}} | \psi_{\text{T}} \rangle \right|^2. \quad (8.47)$$

### QED dipole acceleration

We wish to come back to the expectation value of the dipole acceleration once more. Since the full wavefunction (8.37) is an element of a larger Hilbert space, the dipole acceleration

$$\vec{a}(t) = -\frac{q}{m_e} \cdot \text{tr}_{\text{atom}} \left( \hat{\rho}_{\text{atom}}(t) \frac{\hat{\vec{r}}}{\hat{r}^3} \right) \quad (8.48)$$

has to be determined from a reduced atomic density operator  $\hat{\rho}_{\text{atom}}(t)$  [77]. It is obtained by taking the partial trace of the full density operator  $\hat{\rho} = |\Psi\rangle\langle\Psi|$  over all photonic states. However,

$$\hat{\rho}_{\text{atom}}(t) = \text{tr}_{\text{em}} \hat{\rho}(t) = \begin{pmatrix} \sum_{\mathbf{k}} |c_{b,\mathbf{k}}(t)|^2 & 0 \\ 0 & |c_{\text{T},0}|^2 \end{pmatrix} \quad (8.49)$$

for state (8.37) shows a mixed state in its matrix representation, as expected from a partial trace over an, in general, entangled state. Interestingly, in this case the dipole acceleration

$$\vec{a}(t) = -\frac{q}{m_e} \left[ \sum_{\mathbf{k}} |c_{b,\mathbf{k}}(t)|^2 \cdot \langle \psi_b | \frac{\hat{\vec{r}}}{\hat{r}^3} | \psi_b \rangle + |c_{\text{T},0}|^2 \cdot \langle \psi_{\text{T}} | \frac{\hat{\vec{r}}}{\hat{r}^3} | \psi_{\text{T}} \rangle \right] \quad (8.50)$$

does not have an interference term and does not indicate high harmonic emission.

## 8.5 Results

We want to derive the emission spectrum (8.47) and the recombination probability with the QED approach for the recombination of a twisted electron ( $l = 1$ ) with the ground state  $\psi_g$ . Furthermore, it is assumed that the interaction time is short enough to approximate the coefficient  $c_{\text{T},0} \simeq 1$  to be one, similar to the procedure in Section 8.2.1. In general the form (8.38) can be used for the transition element to a bound states. However, for the case at hand it is easier to perform the spatial derivative of the momentum operator on the ground state wavefunction  $\psi_g$ , i.e.,

$$\hat{\vec{p}} \psi_g = \frac{i\hbar}{a_0} \frac{\vec{r}}{r} \psi_g \quad \Rightarrow \quad \langle \psi_g | \hat{\vec{p}} | \psi_{\text{T}} \rangle = -\frac{i\hbar}{a_0} \langle \psi_g | \frac{\vec{r}}{r} | \psi_{\text{T}} \rangle. \quad (8.51)$$

The  $z$ -component vanishes due to the  $\varphi$ -integration. The transverse components give

$$\int d\varphi e^{i\varphi} \begin{pmatrix} \cos \varphi \\ \sin \varphi \end{pmatrix} = \pi \begin{pmatrix} 1 \\ i \end{pmatrix}. \quad (8.52)$$

Therefore, the transition element in cartesian coordinates is given by

$$\langle \psi_g | \hat{p} | \psi_T \rangle = -\frac{i\hbar\pi}{a_0} \begin{pmatrix} 1 \\ i \\ 0 \end{pmatrix} \cdot \mathcal{N}_{gT}(t) \cdot I(2, 0, 1, t). \quad (8.53)$$

This shows again the equivalence for both transverse directions and it follows that

$$\left| \int_0^t dt' e^{i\omega t'} \langle \psi_g | \hat{p}_x | \psi_T \rangle \right|^2 = \frac{\pi^2}{a_0^2} \left| \int_0^t dt' e^{i\omega t'} \mathcal{N}_{gT}(t) \cdot I(2, 0, 1, t) \right|^2 \quad (8.54)$$

### 8.5.1 Spectrum

Inserting Equation (8.53) the resulting spectrum for the  $x$ -direction of the transition element reads

$$\mathcal{S}_{\text{QED},x}(\omega) = \frac{q^2\pi}{2a_0^2 m_e^2} \cdot \omega^2 \cdot \left| \int_0^t dt' e^{i\omega t'} \mathcal{N}_{gT}(t) \cdot I(2, 0, 1, t) \right|^2. \quad (8.55)$$

It is worth mentioning that this equation presents a full quantum mechanical, analytical approximation for the HHG spectrum of an effective two-level system in three dimensions without the deficiencies of the semiclassical formalism. Even though, we will not present it, the QED formalism does not restrict to the recombination into one state. It allows to easily include more bound states and to obtain a better estimation of the full HHG spectrum.

In principle, expression (8.55) could be further examined with a stationary phase approximation, similar to Section 6.3, but we will just give the numerical evaluation for both laser parameter settings in Figure 8.1. The integration time was chosen to be three driving periods.

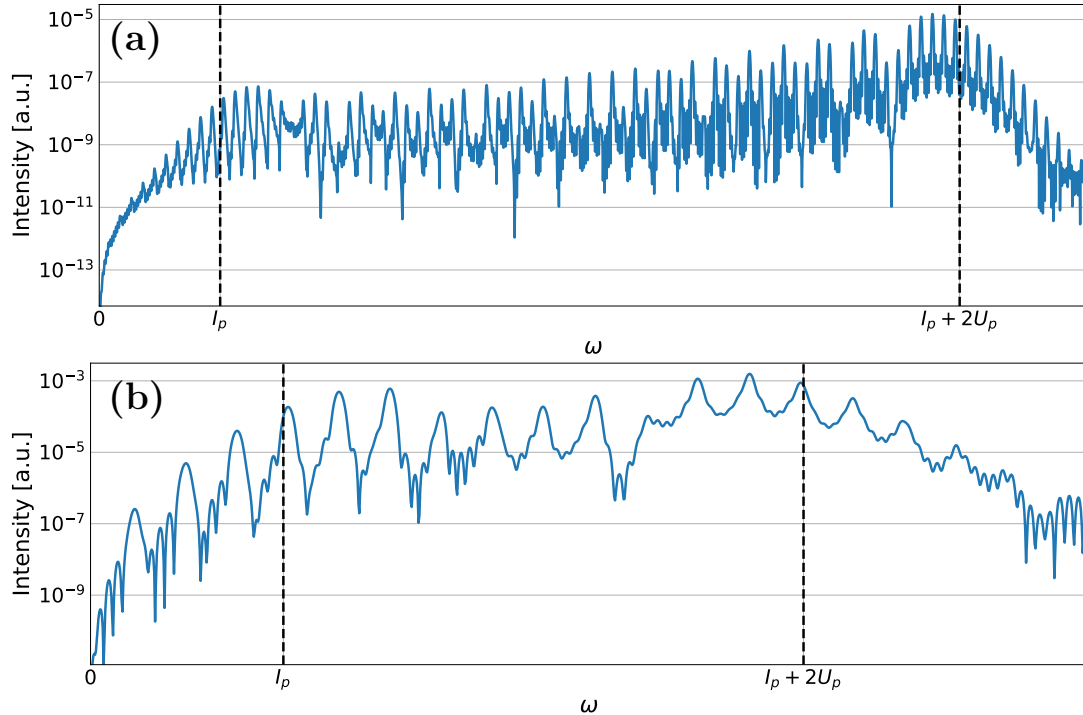


Figure 8.1: The upper plot (a) shows the numerically obtained QED emission spectrum for *scenario 2* in  $x$ -direction with laser parameter setting 1. The result for setting 2 is presented in the lower plot (b). The dashed lines indicate the lower and upper end of the plateau region at  $I_p$  and  $I_p + 2U_p$ , respectively.

In the light of Equation (8.46) we can compare the magnitude of the QED spectra with the semiclassical spectra in Figure 6.3. The difference is due to the chosen prefactors ( $c_b = \sqrt{0.95}$  and  $c_T = \sqrt{0.05}$ ) and is approximately two orders of magnitude ( $c_b^2 c_T^2 = 4.75 \times 10^{-2}$ ).

### 8.5.2 Recombination probability

The probability of recombination into the ground state reads

$$\sum_{\mathbf{k}} |c_{g,\mathbf{k}}(t)|^2 = \frac{V}{(2\pi)^3} \int d\omega \frac{\omega^2}{c^3} \cdot P_{g,\omega}(t) \quad (8.56)$$

$$= \frac{q^2}{3c^3 \hbar m_e^2 a_0^2 \epsilon_0} \int d\omega \omega \left| \int_0^t dt' e^{i\omega t'} \mathcal{N}_{gT}(t) \cdot I(2, 0, 1, t) \right|^2. \quad (8.57)$$

The prefactor can be expressed in terms of the fine-structure constant  $\bar{\alpha} \equiv \frac{q^2}{4\pi\epsilon_0 \hbar c} \approx 1/137$ , which has a bar to distinguish it from the initial width of the twisted wavepacket. This leads to

$$\sum_{\mathbf{k}} |c_{g,\mathbf{k}}(t)|^2 = \frac{4\pi}{3\hbar^2} \bar{\alpha}^3 \int d\omega \omega \left| \int_0^t dt' e^{i\omega t'} \mathcal{N}_{gT}(t) \cdot I(2, 0, 1, t) \right|^2. \quad (8.58)$$

The scaling is due to  $a_0 \propto 1/\bar{\alpha}$  and the fact that the electromagnetic interaction of charged particles with the quantized field scales with  $\sqrt{\bar{\alpha}}$ . The probability of recombination is small because of the cubic scaling. The numerical evaluation of (8.58) is shown in Figure 8.2 for three laser cycles. It confirms that the probability is indeed small and the approximation to set  $c_{T,0}$  to one is justified. We note that the probability has to be multiplied by two to yield the ground state occupation probability due to two transverse directions. The effect of wavefunction diffusion can be seen for setting 2.

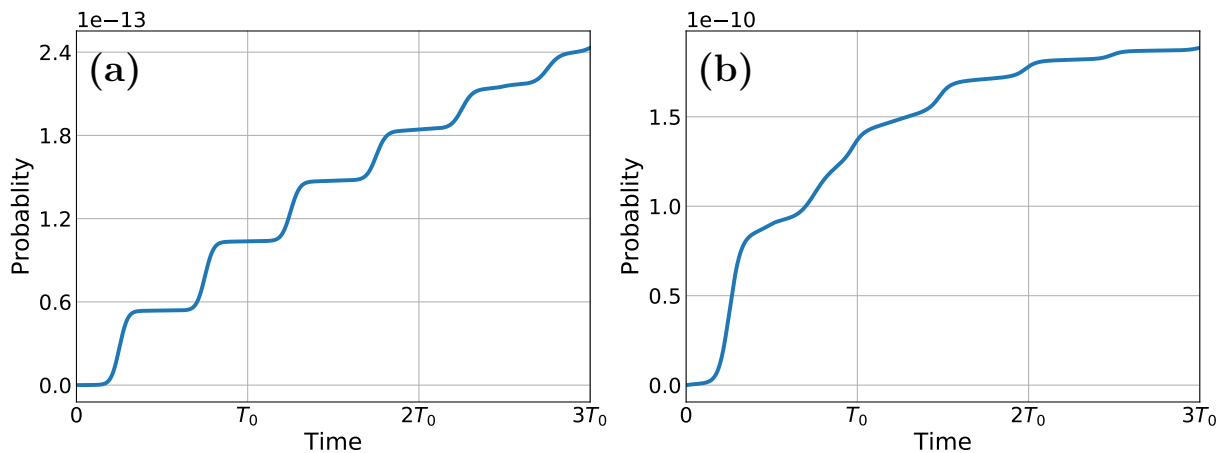


Figure 8.2: The recombination probability (8.58) is shown for three laser cycles. The left plot (a) corresponds to laser parameter setting 1 and the right plot (b) to setting 2.

## 8.6 Application to quantum simulation - hybrid model

Despite the drawback for *scenario 2* from the previous section, the quantum simulation might allow for an improved result over the analytical form from the preceding section. It presents a good opportunity to study the shape of the twisted wavepacket in the combined system of Coulomb potential and laser field. Already the right plot in Figure 7.18 shows the effect of Coulomb focusing. This allows to use a more accurate wavefunction for the numerical calculation

of the QED transition elements. The recombination spectrum can be approximated from the numerically propagated wavefunction  $\psi_{\text{sim}}$  through the transition element

$$\langle \psi_g | \hat{p} | \psi_{\text{sim}} \rangle. \quad (8.59)$$

It easily obtained from an analytical approximation of the ground state or a numerically acquired ground state wavefunction at the instantaneous time  $t$ . Furthermore, the transition element is easily obtained when both wavefunctions are transformed to momentum space. As we mentioned in Chapter 7, some part of the propagated wavefunction might get caught in the smoothed Coulomb potential. However, these contribution will yield only low-frequency components for the transition element and may not matter for the analysis of HHG. The change of  $c_T(t)$  due to recombination is negligibly small and the fraction of bound contributions is also small in the simulation. We perform the spectral evaluation (8.55) with the transition element (8.59) extracted from the simulation for *scenario 2* in Section 7.3.3 and the result is shown in Figure 8.3. The integration time is one laser cycle. The hybrid spectrum is approximately one order of magnitude larger than the theoretically obtained spectrum. We attribute this difference to the effect of Coulomb focusing.

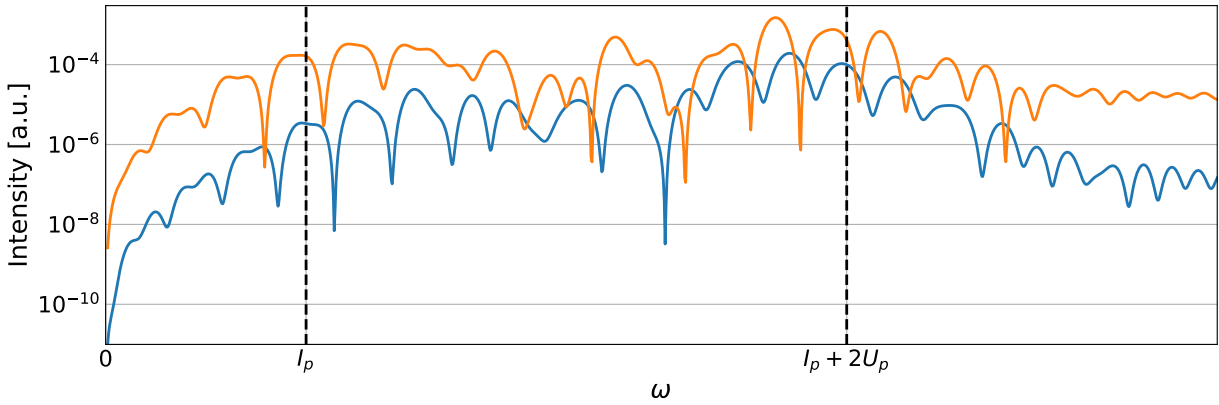


Figure 8.3: The theoretical spectrum (8.55) is compared to the spectrum obtained with the hybrid transition element (8.59). The blue line corresponds to the theoretical result and the orange line to the hybrid model. The dashed black lines indicate the theoretical boundaries of the plateau region.

Based on this result we believe that this method is a good tool to study the interaction of twisted electrons with the Hydrogen ground state even further and that it opens a possibility for future work.

# 9 Conclusion and Outlook

In summary, we were able to qualitatively analyze the emission of high harmonics with twisted electrons in a non-relativistic single-atom framework for the first time. After laying out the fundamental concepts of HHG and of vortex wavepackets we presented the model system for this study including two possible scenarios for the initial conditions. Next, we successfully derived a full analytical form for the twisted electron wavefunction including magnetic contributions from the laser field. For central collisions and neglecting the magnetic field this allowed us to derive an analytical expression for the dipole acceleration of the system with only one approximation in the interference term. The result does not only hold for ground state recombination but is a general formula for all bound states of Hydrogen. The magnetic field can be included with our derivations but the calculations are rather lengthy and are not given in this thesis. The obtained formula brought to light that the emission pattern displays a different characteristic than for traditional HHG, namely that of a rotating electric dipole. This presents the first major result of this thesis. Subsequently, we determined the corresponding spectral intensity by means of a stationary phase approximation and found that the cutoff frequency is unchanged by the use of vortex electrons. If the ionization process is part of the HHG dynamics, then the width of the wavepacket moving under the influence of the laser field is fixed by the ionization rate. However, for the laser-assisted scattering scenario it became clear that the initial width of the wavepacket represents an additional degree of freedom for the dynamics. Hence, we were able to reveal the dependence of the intensity on the initial width on the basis of the SPA result and, furthermore, showed that an optimal width exists for the balance of wavepacket diffusion and recombination probability. It is the second major result of this work and applies not only to HHG with twisted electrons but to HHG dynamics in general. In order to support the analytical findings we performed numerical integrations for the dipole acceleration and found excellent agreement with our analytical results. Furthermore, it showed that the amplitude of the dipole acceleration is at least one order of magnitude smaller than for Gaussian wavepackets due to a smaller wavefunction overlap. Afterwards, we supplemented these findings with numerical results for non-central collisions and examined the result based on the topology of the system and the broken rotational symmetry due to the transverse shift. Additionally, the magnetic field effects were numerically calculated and we found the change in dynamics to originate from the transverse drift due to the magnetic field. To further support our results and to gain additional insights into the dynamics of the twisted wavepackets under the influence of the Coulomb potential, we built a full three-dimensional quantum solver with an approximation scheme for the time evolution operator. Even though we presented a possibility to include the magnetic field contribution we did not implement it and later argued that the magnetic drift is of minor importance due to the strength of the Coulomb potential. The simulation outcomes qualitatively confirmed our analytical and numerical findings. Despite this, it exposed a general flaw of the dipole acceleration formalism and the omission of the quantized electromagnetic field in the model Hamiltonian. Therefore, we derived analytical expressions for the spectrum and the recombination probability within the framework of quantum electrodynamics and compared them to the semiclassical dipole formalism. This presents the third major result of this thesis and constitutes an intricate interplay between a non-perturbative strong field approximation and perturbatively weak electromagnetic couplings to quantized field modes. We concluded our work with a suggestion to combine the quantum electrodynamical formulas with the propagated

wavefunction from the quantum simulation.

Even though the results are already quite satisfactory they open up possible directions for future investigations of HHG dynamics and we want to outline them. The first half will be independent of the intrinsic orbital angular momentum of the recombining wavepacket. The influence of the width of the Volkov wavepacket on the spectral intensity can be further investigated and might lead to a better understanding of scaling properties in HHG scenarios [58, 78] and to pulse engineering for higher efficiency. One of the major challenges for analytical derivations of HHG dynamics is the influence of the Coulomb potential on the Volkov wavepacket. A good approximation would lead to better qualitative and quantitative results. The use of three dimensional quantum simulations might help to reach this goal and support the hitherto existing findings. Attempts to derive Coulomb-Volkov wavefunctions have been undertaken, for example, in references [79, 80, 81]. The use of a classical guiding trajectory method and free time-varying width parameter, similar to the concept in [82], could help to estimate the motion of the wavepacket center and the change of its extension due to the influence of the Coulomb potential. Future work on the QED formalism for HHG might provide insight which form of the dipole operator should be used for finite length time-series in a semiclassical context. In addition, an analysis of the individual quantized field modes and the semiclassically obtained electromagnetic fields could prove quite beneficial for a better understanding of the emission pattern. The following recommendations for future research concern high harmonic generation with twisted electrons. In this work the OAM quantization axis and the electric field polarization were chosen to be collinear. Different non-collinear configurations may lead to dynamics worth investigating. We also believe that it would prove useful to investigate the probability current of the twisted wavepacket in the full quantum simulation with the influence of the Coulomb potential. Furthermore, investigating the dynamics of the vorticity  $\vec{w} = \vec{\nabla} \times \vec{j}_T$  and vortex lines [51] in the simulation, especially in off-axis scattering scenarios, might prove important to disentangle the complexity of the influences of the laser field, the Coulomb potential and the OAM of the electron. Additionally, the propagation of the twisted wavepacket in the quantum simulation, including the magnetic field and neglecting the Coulomb potential, is a possibility to evaluate how long the Taylor expansion in  $1/c$  is valid for the analytical expression of the twisted wavefunction. One significant step forward would be the relativistic treatment of the investigated process for very strong laser fields with the Dirac equation. Finally, an important open question is the realizability of HHG with twisted electrons in a macroscopic setting.



# A Theorems

## A.1 Plancherel theorem

The Fourier transform with symmetric normalization is used to transform the expression

$$\int_{-\infty}^{\infty} dt |a(t)|^2 = \int_{-\infty}^{\infty} dt \left( \frac{1}{\sqrt{2\pi}} \int_{-\infty}^{\infty} d\omega e^{i\omega t} a(\omega) \right) \left( \frac{1}{\sqrt{2\pi}} \int_{-\infty}^{\infty} d\omega' e^{i\omega' t} a(\omega') \right)^* \quad (\text{A.1})$$

$$= \frac{1}{2\pi} \int_{-\infty}^{\infty} d\omega \int_{-\infty}^{\infty} d\omega' \underbrace{\int_{-\infty}^{\infty} dt e^{i(\omega-\omega')t}}_{=2\pi\delta(\omega-\omega')} a(\omega) a^*(\omega') \quad (\text{A.2})$$

$$= \int_{-\infty}^{\infty} d\omega |a(\omega)|^2. \quad (\text{A.3})$$

This is also referred to as Parseval's theorem. Note that for an asymmetric normalization of the Fourier transform and its inverse an additional factor of  $2\pi$  appears.

## A.2 Ehrenfest theorem

The time derivative of the expectation value of an arbitrary operator  $\hat{O}(t)$  in the Schrödinger picture

$$\frac{d}{dt} \langle \psi(t) | \hat{O}(t) | \psi(t) \rangle = \langle \dot{\psi}(t) | \hat{O}(t) | \psi(t) \rangle + \langle \psi(t) | \dot{\hat{O}}(t) | \psi(t) \rangle + \langle \psi(t) | \left( \frac{d\hat{O}(t)}{dt} \right) | \psi(t) \rangle \quad (\text{A.4})$$

can be expanded with the product rule of differentiation. The time argument implies the possibility of explicit time dependence. The time derivative of the bra and ket state can be substituted by the Schrödinger equation

$$|\dot{\psi}(t)\rangle = -\frac{i}{\hbar} \hat{H} |\psi(t)\rangle \quad (\text{A.5})$$

and its complex conjugate

$$\langle \dot{\psi}(t) | = \frac{i}{\hbar} \langle \psi(t) | \hat{H}. \quad (\text{A.6})$$

This gives the final expression for the famous Ehrenfest theorem

$$\frac{d}{dt} \langle \hat{O}(t) \rangle = \frac{i}{\hbar} \langle [\hat{H}, \hat{O}(t)] \rangle + \left\langle \frac{d\hat{O}(t)}{dt} \right\rangle. \quad (\text{A.7})$$



# B Calculations

## B.1 Plane-wave Volkov solutions in velocity and length gauge

The Schrödinger equation with Hamiltonian (5.6) reads

$$i\hbar\psi_V(\vec{r}, t) = \left\{ \frac{\hat{p}^2 - 2q\vec{A}(t) \cdot \hat{p} + q^2\vec{A}^2(t)}{2m_e} + \underbrace{\frac{(\vec{e}_k \cdot \vec{r})}{m_e c} \left[ q \left( \frac{d}{dt} \vec{A}(t) \right) \cdot \hat{p} - \frac{q^2}{2} \frac{d}{dt} \vec{A}^2(t) \right]}_{\equiv \hat{H}_c(\vec{r}, t)} \right\} \psi_V(\vec{r}, t). \quad (\text{B.1})$$

The subscript  $V$  indicates the velocity gauge form and the correction terms have been defined as the Hamiltonian  $\hat{H}_c(\vec{r}, t)$ . For simplicity, we assume that  $\vec{A}(t_0) = 0$  (see Section 4.1) and transform the wavefunction with  $\psi_V = \hat{U}_1 \psi'$ , where  $\hat{U}_1$  is defined as

$$\hat{U}_1(\vec{r}, t) \equiv \exp \left[ -\frac{i}{\hbar} \left( \int_{t_0}^t dt' \hat{H}_c(\vec{r}, t') \right) \right] \quad (\text{B.2})$$

$$= \exp \left[ -\frac{i}{\hbar} \frac{(\vec{e}_k \cdot \vec{r})}{m_e c} \left( q\vec{A}(t) \cdot \hat{p} - \frac{q^2}{2} \vec{A}^2(t) \right) \right]. \quad (\text{B.3})$$

This unitary transformation resembles the form of a Kramers-Henneberger transformation [83, 84], but includes a time-derivative. This close connection will be further explored below.

Whenever the time and position arguments are omitted, the vector potential  $\vec{A}$  is considered to be in its dipole approximation form, namely  $\vec{A}(t)$ . Noting that  $[\hat{H}_c, \hat{U}_1] = 0$  and  $[\vec{A}(t) \cdot \hat{p}, \hat{U}_1] = 0$ , the transformed Schrödinger equation is

$$\hat{U}_1 (i\hbar\partial_t \psi' + \hat{H}_c \psi') = \left( \frac{(\hat{p} - q\vec{A})^2}{2m_e} + \hat{H}_c \right) \hat{U}_1 \psi', \quad (\text{B.4})$$

$$\Rightarrow i\hbar\partial_t \psi' = \hat{U}_1^\dagger \frac{(\hat{p} - q\vec{A})^2}{2m_e} \hat{U}_1 \psi' \quad (\text{B.5})$$

$$= \left( \frac{1}{2m_e} \hat{U}_1^\dagger \hat{p}^2 \hat{U}_1 + \frac{q^2 \vec{A}^2 - 2q\vec{A} \cdot \hat{p}}{2m_e} \right) \psi'. \quad (\text{B.6})$$

The first term can be evaluated with

$$\hat{p}^2 \hat{U}_1 \psi' = \hat{p} \hat{U}_1 \left[ \hat{p} - \frac{\vec{e}_k}{m_e c} \left( q\vec{A} \cdot \hat{p} - \frac{q^2}{2} \vec{A}^2 \right) \right] \psi' \quad (\text{B.7})$$

$$= \hat{U}_1 \left[ \hat{p} - \frac{\vec{e}_k}{m_e c} \left( q\vec{A} \cdot \hat{p} - \frac{q^2}{2} \vec{A}^2 \right) \right]^2 \psi'. \quad (\text{B.8})$$

Plugging this result into (B.6) leads to the Schrödinger equation

$$\boxed{i\hbar\partial_t \psi' = \frac{1}{2m_e} \left[ \hat{p} - q\vec{A} - \frac{\vec{e}_k}{m_e c} \left( q\vec{A} \cdot \hat{p} - \frac{q^2}{2} \vec{A}^2 \right) \right]^2 \psi'}. \quad (\text{B.9})$$

Before proceeding further with the derivation it is interesting to note that in this form the Hamiltonian does not have a position dependence. Hence it makes for an excellent candidate to use in numerical simulations employing a split-operator method since it does not involve products of momentum and position any longer. The advantage was recognized and employed by Brennecke and Lein [66]. One has to check how the transformation  $\hat{U}_1$  acts on a position-dependent potential  $V(\vec{r})$ . Now the connection to a Kramers-Henneberger transformation, mentioned above, comes into play and the transformed operator reads

$$\hat{U}_1^\dagger V(\hat{r}) \hat{U}_1 = \exp \left[ \frac{i}{\hbar} \frac{q(\vec{e}_k \cdot \hat{r})}{m_e c} \vec{A}(t) \cdot \hat{p} \right] V(\hat{r}) \exp \left[ -\frac{i}{\hbar} \frac{q(\vec{e}_k \cdot \hat{r})}{m_e c} \vec{A}(t) \cdot \hat{p} \right]. \quad (\text{B.10})$$

The operator relation, also known as Hadamard's lemma or Baker-Hausdorff lemma,  $e^{\hat{L}} \hat{M} e^{-\hat{L}} = \sum_{n=0}^{\infty} \frac{1}{n!} [\hat{L}, \hat{M}]_n$  with  $[\hat{L}, \hat{M}]_n = [\hat{L}, [\hat{L}, \hat{M}]_{n-1}]$  and  $[\hat{L}, \hat{M}]_0 = \hat{M}$  can be used to simplify this expression [30]. The Coulomb gauge ensures that  $[(\vec{e}_k \cdot \hat{r}), (\vec{A}(t) \cdot \hat{p})] = 0$ , see Section 5.1. The first few terms in the series expansion are

$$\left[ \frac{i}{\hbar} \frac{q(\vec{e}_k \cdot \hat{r})}{m_e c} \vec{A}(t) \cdot \hat{p}, V(\hat{r}) \right]_0 = V(\hat{r}), \quad (\text{B.11})$$

$$\left[ \frac{i}{\hbar} \frac{q(\vec{e}_k \cdot \hat{r})}{m_e c} \vec{A}(t) \cdot \hat{p}, V(\hat{r}) \right]_1 = \frac{i}{\hbar} \frac{q(\vec{e}_k \cdot \hat{r})}{m_e c} \vec{A}(t) \cdot \underbrace{[\hat{p}, V(\hat{r})]}_{=-i\hbar \vec{\nabla} V} = \frac{q(\vec{e}_k \cdot \hat{r})}{m_e c} \vec{A}(t) \cdot \vec{\nabla} V(\vec{r}) \Big|_{\vec{r}=\hat{r}}, \quad (\text{B.12})$$

$$\frac{1}{2} \left[ \frac{i}{\hbar} \frac{q(\vec{e}_k \cdot \hat{r})}{m_e c} \vec{A}(t) \cdot \hat{p}, V(\hat{r}) \right]_2 = \dots = \frac{1}{2} \left[ \frac{q(\vec{e}_k \cdot \hat{r})}{m_e c} \vec{A}(t) \cdot \vec{\nabla} \right]^2 V(\vec{r}) \Big|_{\vec{r}=\hat{r}}. \quad (\text{B.13})$$

These terms can be recognized from the Taylor expansion

$$\sum_{n=0}^{\infty} \frac{1}{n!} \left[ \frac{q(\vec{e}_k \cdot \hat{r})}{m_e c} \vec{A}(t) \cdot \vec{\nabla} \right]^n V(\vec{r}) \Big|_{\vec{r}=\hat{r}} = V \left( \hat{r} + \frac{q(\vec{e}_k \cdot \hat{r})}{m_e c} \vec{A}(t) \right) \quad (\text{B.14})$$

and lead to a shifted potential, known from the Kramers-Henneberger frame. The full Schrödinger equation

$$\boxed{i\hbar \partial_t \psi' = \left[ \frac{1}{2m_e} \left[ \hat{p} - q\vec{A} - \frac{\vec{e}_k}{m_e c} \left( q\vec{A} \cdot \hat{p} - \frac{q^2}{2} \vec{A}^2 \right) \right]^2 + V \left( \vec{r} + \frac{q(\vec{e}_k \cdot \hat{r})}{m_e c} \vec{A} \right) \right] \psi'} \quad (\text{B.15})$$

contains no products of momentum and position. This is the result obtained in [66].

The Volkov solution ( $V = 0$ ) emerges easily by recognizing that equation (B.9) has only momentum operators on the right side and can be solved with a product of a time-dependent function and momentum operator eigenfunctions [61]. The ansatz  $\psi'_p(\vec{r}, t) = f_p(t) \cdot e^{\frac{i}{\hbar} \vec{p} \cdot \vec{r}}$  gives a differential equation for  $f_p$ , i.e.,

$$i\hbar \partial_t f_p(t) = \frac{1}{2m_e} \left[ \underbrace{\vec{p} - q\vec{A} - \frac{\vec{e}_k}{m_e c} \left( q\vec{A}(t) \cdot \vec{p} - \frac{q^2}{2} \vec{A}^2(t) \right)}_{\equiv \vec{\pi}(t)} \right]^2 f_p(t) \quad (\text{B.16})$$

$$\Rightarrow f_p(t) = f_p(t_0) \exp \left[ -\frac{i}{\hbar} \int_{t_0}^t dt' \frac{\vec{\pi}^2(t')}{2m_e} \right], \quad (\text{B.17})$$

which has an exponential solution. For notational economy a new symbol, i.e.,  $\vec{\pi}(t)$ , for the kinetic momentum has been introduced. The full plane-wave Volkov wavefunctions in velocity gauge read

$$\psi_{V,\vec{p}}(\vec{r}, t) = f_{\vec{p}}(t_0) \exp \left[ \frac{i}{\hbar} \left( \vec{r} \cdot \left( \vec{p} - \frac{\vec{e}_k}{m_e c} \left( q \vec{A}(t) \cdot \vec{p} - \frac{q^2}{2} \vec{A}^2(t) \right) \right) - \int_{t_0}^t dt' \frac{\vec{\pi}^2(t')}{2m_e} \right) \right]. \quad (\text{B.18})$$

The transformation to length gauge with  $\psi_{L,\vec{p}}(\vec{r}, t) = \exp \left( -iq \vec{A}(t) \cdot \vec{r} / \hbar \right) \psi_{V,\vec{p}}(\vec{r}, t)$  leads to the elegant form

$$\boxed{\psi_{L,\vec{p}}(\vec{r}, t) = f_{\vec{p}}(t_0) \exp \left[ \frac{i}{\hbar} \left( \vec{\pi}(t) \cdot \vec{r} - \int_{t_0}^t dt' \frac{\vec{\pi}^2(t')}{2m_e} \right) \right]}. \quad (\text{B.19})$$

This is exactly the result given in reference [43]. The normalization shall not be important here.

## B.2 Derivation of $\phi$ -integration in plane-wave decomposition

Using the Jacobi-Anger expansion

$$e^{iz \cos(\theta)} = \sum_{n=-\infty}^{n=\infty} i^n J_n(z) e^{in\theta}$$

allows to derive the analytical result for the integral

$$\begin{aligned} \int_0^{2\pi} d\phi e^{il\phi} e^{i\xi \cos(\phi-\varphi)} &= \sum_{n=-\infty}^{n=\infty} i^n J_n(\xi) \int_0^{2\pi} d\phi e^{il\phi} e^{in(\phi-\varphi)} \\ &= \sum_{n=-\infty}^{n=\infty} i^n J_n(\xi) e^{-in\varphi} \underbrace{\int_0^{2\pi} d\phi e^{i(l+n)\phi}}_{=2\pi\delta_{-l,n}} \\ &= 2\pi e^{il\varphi} i^{-l} \underbrace{J_{-l}(\xi)}_{=i^{2l} J_l(\xi)} \\ &= 2\pi i^l e^{il\varphi} J_l(\xi). \end{aligned}$$

## B.3 Momentum space integration of Volkov wavefunctions

Before performing the actual integration in momentum space it is necessary to expand the exponent in the non-dipole Volkov wavefunctions (5.13)

$$\begin{aligned} \psi_{L,\vec{p}}(\vec{r}, t) &\approx \left[ 1 + iF_1(p_{\parallel}) \right] \left[ 1 + ip_{\perp} \sin \phi F_0(p_{\parallel}) \right] \times \\ &\exp \left[ \frac{i}{\hbar} \left\{ -qA(t)z + p_{\parallel} (z - r_{\omega_0}(t)) + p_{\perp} \rho \cos(\phi - \varphi) - S_{\omega_0}(t) - \frac{(p_{\perp}^2 + p_{\parallel}^2)t}{2m_e} \right\} \right] \end{aligned} \quad (\text{B.20})$$

to first order in  $1/c$ . The auxiliary correction terms

$$F_0(p_{\parallel}) = -\frac{p_{\parallel} r_{\omega_0}(t) + S_{\omega_0}(t)}{\hbar m_e c}, \quad (\text{B.21})$$

$$F_1(p_{\parallel}) = \frac{\rho \sin \varphi}{\hbar m_e c} \left( \frac{q^2}{2} A^2(t) - qA(t)p_{\parallel} \right) \quad (\text{B.22})$$

were introduced. An analysis of the limits of this approximation is given below in Section B.3.2. The normalization constant is neglected for now. First, we examine the  $\varphi$ -integration

$$(5.17) \propto \int_0^{2\pi} d\phi e^{i\phi} e^{i\xi \cos(\phi-\varphi)} \left[ 1 + iF_0(p_{\parallel})p_{\perp} \sin \phi \right] \quad (\text{B.23})$$

$$= \int_0^{2\pi} d\phi e^{i\phi} e^{i\xi \cos(\phi-\varphi)} \left[ 1 + \frac{F_0(p_{\parallel})p_{\perp}}{2} (e^{i\phi} - e^{-i\phi}) \right]. \quad (\text{B.24})$$

For convenience, the variable  $\xi = p_{\perp}\rho/\hbar$  was introduced. The integral can be evaluated with the integral representation for Bessel functions (Appendix B.2) and is a sum of three Bessel functions, namely

$$(5.17) \propto 2\pi i^l e^{il\varphi} \left[ J_l(\xi) + i \frac{F_0(p_{\parallel})p_{\perp}}{2} (e^{i\varphi} J_{l+1}(\xi) + e^{-i\varphi} J_{l-1}(\xi)) \right]. \quad (\text{B.25})$$

The two remaining integrations are

$$\begin{aligned} \psi_{\text{T}}^{(c)}(\vec{r}, t) \propto & \int_{-\infty}^{\infty} dp_{\parallel} e^{-p_{\parallel}^2 \gamma_{\alpha}(t)/2} e^{\frac{i}{\hbar} p_{\parallel} (z - r_{\omega_0}(t))} \left[ 1 + iF_1(p_{\parallel}) \right] \times \\ & \int_0^{\infty} dp_{\perp} p_{\perp}^{l+1} e^{-p_{\perp}^2 \gamma_{\beta}(t)/2} \left[ J_l(p_{\perp}\rho/\hbar) \right. \\ & \left. + i \frac{F_0(p_{\parallel})p_{\perp}}{2} (e^{i\varphi} J_{l+1}(p_{\perp}\rho/\hbar) + e^{-i\varphi} J_{l-1}(p_{\perp}\rho/\hbar)) \right] \end{aligned} \quad (\text{B.26})$$

with the auxiliary variables

$$\gamma_{\alpha}(t) = \left( \frac{\alpha^2}{\hbar^2} + i \frac{t}{m_e \hbar} \right) \equiv \frac{\alpha^2}{\hbar^2} (1 + i\tau_{\alpha}) \quad \text{with} \quad \tau_{\alpha}(t) \equiv \frac{\hbar t}{m_e \alpha^2}, \quad (\text{B.27})$$

$$\gamma_{\beta}(t) = \left( \frac{\beta^2}{\hbar^2} + i \frac{t}{m_e \hbar} \right) \equiv \frac{\beta^2}{\hbar^2} (1 + i\tau_{\beta}) \quad \text{with} \quad \tau_{\beta}(t) \equiv \frac{\hbar t}{m_e \beta^2}. \quad (\text{B.28})$$

The  $\tau_i$  are dimensionless times which correspond to the spreading time scale of the wavepacket in longitudinal and transverse direction.

### Integrals involving Bessel functions

The necessary solutions to these integrals can be found in reference [85]. The relations

$$\int_0^{\infty} dx J_{\nu}(yx) x^{\nu+1} e^{-\sigma x^2/2} = \frac{1}{\sigma^{\nu+1}} y^{\nu} \exp\left(-\frac{y^2}{2\sigma}\right), \quad (\text{B.29})$$

$$\Rightarrow \int_0^{\infty} dx J_{\nu-1}(yx) x^{\nu+2} e^{-\sigma x^2/2} = \frac{2}{\sigma^{\nu+1}} y^{\nu-1} \exp\left(-\frac{y^2}{2\sigma}\right) \underbrace{\left[ \nu - \frac{y^2}{2\sigma} \right]}_{=L_1^{\nu-1}(y^2/2\sigma)} \quad (\text{B.30})$$

hold for  $\Re \sigma > 0$ ,  $\Re \nu > -1$  and  $y > 0$ . The last result was obtained with the help of a derivative with respect to  $\sigma$ . In general, using this procedure further would allow to derive analytical results for higher modes Laguerre-Gaussian modes with more than one local extremum.

Hence, equation (B.26) reduces to

$$(B.26) = \frac{1}{\gamma_\beta^{l+1}} \left( \frac{\rho}{\hbar} \right)^l \exp \left( -\frac{\rho^2}{2\hbar^2\gamma_\beta} \right) \int_{-\infty}^{\infty} dp_{\parallel} e^{-p_{\parallel}^2\gamma_\alpha(t)/2} e^{\frac{i}{\hbar}p_{\parallel}(z-r_{\omega_0}(t))} \left[ 1 + iF_1(p_{\parallel}) \right] \times \left[ 1 + i\frac{F_0(p_{\parallel})}{2} \left\{ e^{i\varphi} \left( \frac{\rho}{\gamma_\beta\hbar} \right) - e^{-i\varphi} \left( \frac{\rho}{\hbar\gamma_\beta} - \frac{2l\hbar}{\rho} \right) \right\} \right]. \quad (B.31)$$

Expanding the squared brackets

$$[1 + iF_1][1 + iF_0(\dots)] \approx 1 + i[F_1 + F_0(\dots)] \equiv 1 + i[F_3 - p_{\parallel}F_2] \quad (B.32)$$

and neglecting terms proportional to  $\mathcal{O}(c^{-2})$  makes the definition of new auxiliary variables desirable. The new variables are

$$F_2 \equiv \frac{1}{\hbar m_e c} [qA \cdot \rho \sin \varphi + F_4 \cdot r_{\omega_0}], \quad (B.33)$$

$$F_3 \equiv \frac{1}{\hbar m_e c} \left[ \rho \sin \varphi \cdot \frac{q^2}{2} A^2 - F_4 \cdot S_{\omega_0} \right], \quad (B.34)$$

$$F_4 \equiv e^{-i\varphi} \frac{l\hbar}{\rho} + i \frac{\rho}{\hbar\gamma_\beta} \sin \varphi. \quad (B.35)$$

The last integral is frequently encountered in physics and has the solution

$$\int_{-\infty}^{\infty} dp_{\parallel} e^{-\gamma_\alpha p_{\parallel}^2/2} e^{\frac{i}{\hbar}p_{\parallel}(z-r_{\omega_0})} \left[ 1 + iF_3 - iF_2 p_{\parallel} \right] = \sqrt{\frac{2\pi}{\gamma_\alpha}} \left[ 1 + iF_3 + \frac{(z-r_{\omega_0})}{\hbar\gamma_\alpha} F_2 \right] e^{-\frac{(z-r_{\omega_0})^2}{2\hbar^2\gamma_\alpha}} \quad (B.36)$$

The final result for the twisted wavefunction, including a normalization constant  $\mathcal{N}_T$ , is

$$\psi_T^{(c)} = [1 + F] \underbrace{\mathcal{N}_T e^{i\varphi} e^{-\frac{i}{\hbar}[qAz + S_{\omega_0}]} \rho^l \exp \left[ -\frac{1}{2} \left( \frac{(z-r_{\omega_0})^2 \cdot (1-i\tau_\alpha)}{\sigma_\alpha^2} + \frac{\rho^2 \cdot (1-i\tau_\beta)}{\sigma_\beta^2} \right) \right]}_{\equiv \psi_T}, \quad (B.37)$$

or

$$|\psi_T^{(c)}\rangle = [1 + \hat{F}] |\psi_T\rangle \quad (B.38)$$

and includes the correction term

$$F \equiv iF_3 + \frac{\hbar(z-r_{\omega_0}) \cdot (1-i\tau_\alpha)}{\sigma_\alpha^2} F_2 \propto \mathcal{O}(c^{-1}) \quad (B.39)$$

and the time-dependent longitudinal and transverse widths

$$\sigma_\alpha(t) \equiv \alpha \sqrt{1 + \tau_\alpha^2(t)}, \quad \sigma_\beta(t) \equiv \beta \sqrt{1 + \tau_\beta^2(t)}. \quad (B.40)$$

### B.3.1 Normalization

The normalization constant  $\mathcal{N}_T$  still has to be determined to get the full wavefunction, fulfilling the normalization condition  $\int dV |\psi_T^{(c)}(\vec{r}, t)|^2 = 1$ . The probability density is given by

$$|\psi_T^{(c)}|^2 = [1 + 2\Re F] \cdot |\psi_T|^2 = \mathcal{N}_T^2 [1 + 2\Re F] \rho^{2l} \exp \left[ -\left( \frac{(z-r_{\omega_0})^2}{\sigma_\alpha^2} + \frac{\rho^2}{\sigma_\beta^2} \right) \right], \quad (B.41)$$

neglecting  $\propto c^{-2}$  terms again. The function arguments are omitted for the sake of simplicity. The integration over  $\mathbb{R}^3$  determines the normalization constant. Since the correction term  $F$  depends on  $\propto \sin \varphi$  and  $\propto \cos \varphi$  terms only, it vanishes for the integration over  $\varphi$ . This means that the correction term

$$\langle \psi_{\text{T}} | \hat{F} | \psi_{\text{T}} \rangle = 0 \quad (\text{B.42})$$

is orthogonal to the dipole approximation form of the twisted wavepacket. The density is otherwise cylindrical symmetric and a factor of  $2\pi$  is obtained for the  $\varphi$ -integration. Performing two standard integrations for  $\rho$  and  $z$  gives the expressions

$$\begin{aligned} \int dV |\psi_{\text{T}}|^2 &= \mathcal{N}_{\text{T}}^2 \cdot 2\pi \underbrace{\int_0^\infty d\rho \rho^{2l+1} \exp\left[-\frac{\rho^2}{\sigma_\beta^2}\right]}_{=\frac{l!}{2}\sigma_\beta^{2(l+1)}} \underbrace{\int_{-\infty}^\infty dz \exp\left[-\frac{(z-r_{\omega_0})^2}{\sigma_\alpha^2}\right]}_{=\sqrt{\pi}\sigma_\alpha} \\ &= \mathcal{N}_{\text{T}}^2 \cdot \pi l! \sigma_\beta^{2(l+1)} \cdot \sqrt{\pi}\sigma_\alpha \stackrel{!}{=} 1, \\ \Rightarrow \mathcal{N}_{\text{T}} &= \left(\pi^{1/4} \sigma_\beta^{l+1} \sqrt{\pi l! \sigma_\alpha}\right)^{-1} \end{aligned}$$

for the normalization.

### B.3.2 Limits of approximations

The expansions of (5.13) can only be valid as long as the two correction terms  $\propto \mathcal{O}(c^{-1})$  are sufficiently small. The first correction term is  $F_1$  (see equation (B.22)) and has to fulfill  $|F_1| \ll 1$ , leading to

$$\left| \rho \sin \varphi \left( \frac{q^2}{2} A^2(t) - qA(t)p_{\parallel} \right) \right| \leq \rho \left( \frac{q^2}{2} A_0^2 + q|p_{\parallel}|A_0 \right) \ll m_e \hbar c. \quad (\text{B.43})$$

We approximate  $\rho$  with the transverse width  $\sigma_\beta(t)$  and  $p_{\parallel}$  with the longitudinal width in momentum space, namely  $\hbar/\sigma_\alpha(t)$ . It has to hold that

$$|q|A_0 \left[ \frac{|q|A_0\sigma_\beta(t)}{2\hbar} + \frac{\sigma_\beta(t)}{\sigma_\alpha(t)} \right] \ll m_e c. \quad (\text{B.44})$$

The quantity  $|q|A_0$  represents the maximal momentum the electron can gain in the laser field. Later the widths will be set to be equal and, therefore,  $\sigma_\beta(t)/\sigma_\alpha(t) = 1$  and is usually smaller than the first term, for sufficiently strong laser fields. The approximation will depend on the length  $T_{\text{max}}$  of the laser pulse. The resulting twisted wavepacket can only be valid up to a certain time  $t_c$ , since  $\sigma_\beta(t)$  is monotonically increasing.

The second approximation concerns the term  $p_{\perp} \sin \phi F_1$ . The quiver motion  $r_{\omega_0}(t)$  is bound by  $|q|A_0/(m_e\omega_0)$  and, hence, the limit reads

$$\left| p_{\perp} \sin \phi \left( p_{\parallel} r_{\omega_0}(t) + S_{\omega_0}(t) \right) \right| \leq p_{\perp} \left( \frac{|q|A_0}{m_e\omega_0} p_{\parallel} + |S_{\omega_0}(t)| \right) \ll m_e \hbar c. \quad (\text{B.45})$$

We will use the time-average of the action  $S_{\omega_0}(t) \approx U_p t = q^2 A_0^2 t / (4m_e)$  and approximate the momenta with the same treatment as above, giving

$$\frac{|q|A_0}{m_e\omega_0\sigma_\beta(t)} \left( \frac{\hbar}{\sigma_\alpha(t)} + \frac{|q|A_0 \cdot \omega_0 t}{4} \right) \ll m_e c. \quad (\text{B.46})$$



The right-hand side is monotonically decreasing and the relation has to be valid at an initial time  $t_0$  to be fulfilled for all times. Additionally, the first term in brackets is usually much smaller for times  $t \gtrsim T_0 = 2\pi/\omega_0$ .

For both parameter settings from Section 5.5 the corresponding limits are shown in Figure B.1. For setting 1 the limit function approaches its break down point. However, the approximation is only less accurate for the outer regions of the twisted wavepacket. These regions are not important for the calculations of transition elements with Hydrogen bound states for small and medium values for the impact parameter. For large impact parameters the Hydrogen bound state will probe the outer regions of the twisted wavepacket, but the characteristic structure of a vortex is not important anymore in this region. In these cases, the overlap of the bound state is calculate from an exponentially decaying wavefunction with an almost constant phase value (see Figure 7.3).

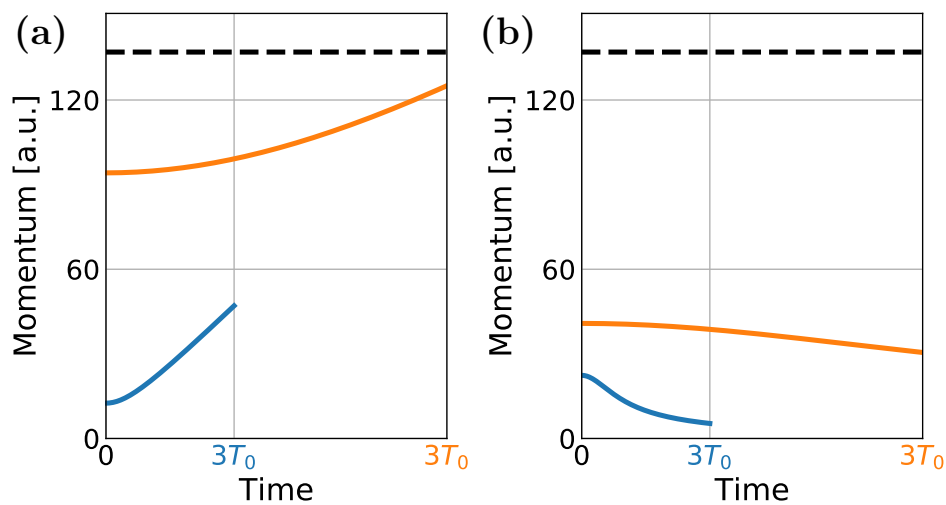


Figure B.1: The functions (B.44) and (B.46) for both parameter settings (see Table 5.1) are shown on the left and the right plot, respectively. Setting 1 is indicated by the orange color and setting 2 by the blue color. The black dashed lines indicate the limiting value  $m_e c$ . The curves are shown for the longest laser pulses length employed in this thesis, namely three laser cycles ( $3T_0$ ). The function values are given in atomic units (Appendix C.1).

## B.4 Main integral

One of the major integrals in this thesis occurs whenever a transition element between the bound and the free part has to be calculated. It will be of the form  $\langle \psi_b | r^{m_r} u^{m_u} \sqrt{1-u^2}^{n_u} | \psi_T \rangle$ . Such terms are proportional to a volume integral and the two-dimensional integration over  $r$  and  $u = \cos \theta$  in spherical coordinates will be considered here. It is defined as

$$I_{l,\Delta n,n,l',m}(m_r, m_u, n_u, t) \equiv \int_0^\infty dr r^{l+l'+m_r} e^{-\frac{r}{na_0}} e^{-\frac{r^2(1-i\tau(t))}{2\sigma^2(t)}} L_{\Delta n}^{2l'+1} \left( \frac{2r}{na_0} \right) \\ \times \int_{-1}^1 du u^{m_u} \sqrt{1-u^2}^{l+n_u} e^{ru \left( \frac{r\omega_0(1-i\tau(t))}{2\sigma^2(t)} - \frac{i}{\hbar} qA \right)} P_l^m(u). \quad (\text{B.47})$$

For the sake of simplicity,  $\Delta n = n - l - 1$  was introduced. In order to solve it analytically the approximation

$$e^{-\frac{r^2(1-i\tau(t))}{2\sigma^2(t)}} e^{-\frac{r}{na_0}} \approx (1 + \dots) \cdot e^{-\frac{r}{na_0}} \quad (\text{B.48})$$

has to be made. This is reasonable as long as  $\sigma(t) \gg na_0$ . Even if the initial width is smaller than  $a_0$ , the wavefunction diffuses very quickly and the width is, again, larger than the atomic state extension when the free part hits the core. This will be true for small enough  $n$ , but since we expect the strong field approximation to break down for higher lying states, it seems a fair approximation. If necessary, higher order terms in the Taylor expansion could be included easily. Now the integral has the form

$$I_{l,\Delta n,n,l',m}(m_r, m_u, n_u) \approx \int_0^\infty dr r^{l+l'+m_r} e^{-\frac{r}{na_0}} L_{\Delta n}^{2l'+1} \left( \frac{2r}{na_0} \right) \times \int_{-1}^1 du u^{m_u} \sqrt{1-u^2}^{l+n_u} e^{iaru} P_l^m(u) \quad (\text{B.49})$$

and can be solved analytically. All time arguments are omitted in the following and a new auxiliary variable  $a \equiv -qA/\hbar - r_{\omega_0}(i + \tau)/\sigma^2$  is introduced for the sake of clarity. In case that  $m = -|m| < 0$ , the property

$$P_l^{-|m|}(x) = (-1)^{|m|} \frac{(l-|m|)!}{(l+|m|)!} P_l^{|m|}(x) \quad (\text{B.50})$$

of the associated Legendre polynomials is used. For the derivation it is assumed that  $m \geq 0$ , but a prefactor  $M_m$  is kept in order to cover this case as well. We define it as

$$M_m = \begin{cases} 1 & m \geq 0 \\ (-1)^{|m|} \frac{(l-|m|)!}{(l+|m|)!} & m < 0 \end{cases}. \quad (\text{B.51})$$

The first integral can be re-expressed as

$$\int_{-1}^1 du u^{m_u} \sqrt{1-u^2}^{l+n_u} P_l^m(u) e^{iaru} = \frac{(-1)^m}{2^l (l')!} \int_{-1}^1 du u^{m_u} \sqrt{1-u^2}^{l+m+n_u} e^{iaru} \partial_u^{m+l'} (u^2-1)^{l'}. \quad (\text{B.52})$$

The polynomial can be further expanded with the help of the binomial formula and gives

$$\partial_u^{m+l'} (u^2-1)^{l'} = \partial_u^{m+l'} \sum_{k=0}^{l'} \binom{l'+\Delta l}{k} (-1)^{l'-k} u^{2k} \quad (\text{B.53})$$

$$= \sum_{k=\lceil \frac{m+l'}{2} \rceil}^{l'} \binom{l'}{k} (-1)^{l'-k} \frac{(2k)!}{(2k-m-l')!} u^{2k-m-l'}. \quad (\text{B.54})$$

The ceiling function is denoted by  $[x]$ . We introduce new auxiliary integer variables  $\gamma = \gamma(k) \equiv 2k - m - l' + m_u$  and  $\nu \equiv l + m + n_u$ . The analytical solution of the integrals depends on the parity of  $\gamma$ . The results

$$\int_{-1}^1 du u^\gamma \sqrt{1-u^2}^\nu e^{iaru} = \Gamma\left(\frac{2+\nu}{2}\right) \begin{cases} \frac{\Gamma(\frac{1+\gamma}{2})}{\Gamma(\frac{3+\nu+\gamma}{2})} \cdot {}_1F_2\left(\frac{1+\gamma}{2}; \frac{1}{2}, \frac{3+\nu+\gamma}{2}; -\frac{a^2 r^2}{4}\right) & \text{for } \gamma \text{ even} \\ iar \frac{\Gamma(\frac{2+\gamma}{2})}{\Gamma(\frac{4+\nu+\gamma}{2})} \cdot {}_1F_2\left(\frac{2+\gamma}{2}; \frac{3}{2}, \frac{4+\nu+\gamma}{2}; -\frac{a^2 r^2}{4}\right) & \text{for } \gamma \text{ odd} \end{cases}$$

(B.55)

are valid for  $\gamma > -1$  and  $\nu > -2$ . Summing up all terms gives the solution

$$\begin{aligned} & \int_{-1}^1 du u^{m_u} \sqrt{1-u^2}^{l+n_u} P_l^m(u) e^{iaru} \\ &= \sum_{k=\lceil \frac{m+l'}{2} \rceil}^{l'} \binom{l'}{k} \frac{(-1)^{m+l'-k} (2k)!}{2^{l'} l'! (2k-m-l')!} \int_{-1}^1 du u^\gamma \sqrt{1-u^2}^\nu e^{iaru} \end{aligned} \quad (\text{B.56})$$

$$\begin{aligned} &= \sum_{k=\lceil \frac{m+l'}{2} \rceil}^{l'} \binom{l'}{k} \frac{(-1)^{m+l'-k} (2k)!}{2^{l'} l'! (2k-m-l')!} \underbrace{\Gamma\left(\frac{2+\nu}{2}\right)}_{\equiv M_k} \\ & \cdot \begin{cases} \frac{\Gamma\left(\frac{1+\gamma}{2}\right)}{\Gamma\left(\frac{3+\nu+\gamma}{2}\right)} \cdot {}_1F_2\left(\frac{1+\gamma}{2}; \frac{1}{2}, \frac{3+\nu+\gamma}{2}; -\frac{a^2 r^2}{4}\right) & \text{for } \gamma(k) \text{ even} \\ iar \frac{\Gamma\left(\frac{2+\gamma}{2}\right)}{\Gamma\left(\frac{4+\nu+\gamma}{2}\right)} \cdot {}_1F_2\left(\frac{2+\gamma}{2}; \frac{3}{2}, \frac{4+\nu+\gamma}{2}; -\frac{a^2 r^2}{4}\right) & \text{for } \gamma(k) \text{ odd.} \end{cases} \end{aligned} \quad (\text{B.57})$$

To tackle the  $r$ -integration it is necessary to expand the generalized Laguerre polynomial

$$L_{\Delta n}^{2l'+1}\left(\frac{2r}{na_0}\right) = \sum_{s=0}^{\Delta n} \left(-\frac{2}{na_0}\right)^s \binom{\Delta n + 2l' + 1}{\Delta n - s} \frac{r^s}{s!}. \quad (\text{B.58})$$

The general solution for the integrals involving the generalized hypergeometric functions is

$$\begin{aligned} & \int_0^\infty dr r^k e^{-\frac{r}{na_0}} \cdot {}_1F_2\left(\frac{n_0}{2}; \frac{n_1}{2}, \frac{n_2}{2}; -\frac{a^2 r^2}{4}\right) \\ &= (na_0)^{k+1} k! {}_3F_2\left(\frac{k+1}{2}, \frac{k+2}{2}, \frac{n_0}{2}; \frac{n_1}{2}, \frac{n_2}{2}; -a^2 n^2 a_0^2\right) \quad (k > -1). \end{aligned} \quad (\text{B.59})$$

With yet another helper variable  $\kappa = \kappa(s) \equiv l + l' + m_r + s$ , the resulting expression reads

$$\begin{aligned} & \int_0^\infty dr r^\kappa e^{-\frac{r}{na_0}} \cdot \begin{cases} \frac{\Gamma\left(\frac{1+\gamma}{2}\right)}{\Gamma\left(\frac{3+\nu+\gamma}{2}\right)} \cdot {}_1F_2\left(\frac{1+\gamma}{2}; \frac{1}{2}, \frac{3+\nu+\gamma}{2}; -\frac{a^2 r^2}{4}\right) & \text{for } \gamma \text{ even} \\ iar \frac{\Gamma\left(\frac{2+\gamma}{2}\right)}{\Gamma\left(\frac{4+\nu+\gamma}{2}\right)} \cdot {}_1F_2\left(\frac{2+\gamma}{2}; \frac{3}{2}, \frac{4+\nu+\gamma}{2}; -\frac{a^2 r^2}{4}\right) & \text{for } \gamma \text{ odd} \end{cases} \\ &= (na_0)^{\kappa+1} \kappa! \cdot \begin{cases} \frac{\Gamma\left(\frac{1+\gamma}{2}\right)}{\Gamma\left(\frac{3+\nu+\gamma}{2}\right)} \cdot {}_3F_2\left(\frac{\kappa+1}{2}, \frac{\kappa+2}{2}, \frac{1+\gamma}{2}; \frac{1}{2}, \frac{3+\nu+\gamma}{2}; -a^2 n^2 a_0^2\right) & \text{for } \gamma \text{ even} \\ iar \frac{\Gamma\left(\frac{2+\gamma}{2}\right)}{\Gamma\left(\frac{4+\nu+\gamma}{2}\right)} \cdot {}_3F_2\left(\frac{\kappa+2}{2}, \frac{\kappa+3}{2}, \frac{2+\gamma}{2}; \frac{3}{2}, \frac{4+\nu+\gamma}{2}; -a^2 n^2 a_0^2\right) & \text{for } \gamma \text{ odd} \end{cases}. \end{aligned} \quad (\text{B.60})$$

$$\begin{aligned} &= (na_0)^{\kappa+1} \kappa! \cdot \begin{cases} \frac{\Gamma\left(\frac{1+\gamma}{2}\right)}{\Gamma\left(\frac{3+\nu+\gamma}{2}\right)} \cdot {}_3F_2\left(\frac{\kappa+1}{2}, \frac{\kappa+2}{2}, \frac{1+\gamma}{2}; \frac{1}{2}, \frac{3+\nu+\gamma}{2}; -a^2 n^2 a_0^2\right) & \text{for } \gamma \text{ even} \\ iar \frac{\Gamma\left(\frac{2+\gamma}{2}\right)}{\Gamma\left(\frac{4+\nu+\gamma}{2}\right)} \cdot {}_3F_2\left(\frac{\kappa+2}{2}, \frac{\kappa+3}{2}, \frac{2+\gamma}{2}; \frac{3}{2}, \frac{4+\nu+\gamma}{2}; -a^2 n^2 a_0^2\right) & \text{for } \gamma \text{ odd} \end{cases}. \end{aligned} \quad (\text{B.61})$$

We define another prefactor

$$M_s \equiv \left(-\frac{2}{na_0}\right)^s \binom{\Delta n + 2l' + 1}{\Delta n - s} \frac{(na_0)^{\kappa(s)+1} \kappa(s)!}{s!} \quad (\text{B.62})$$

$$= \binom{\Delta n + 2l' + 1}{\Delta n - s} \frac{(-2)^s \kappa(s)!}{s!} (na_0)^{l+l'+m_r+1} \quad (\text{B.63})$$

for convenience. The full solution, including  $m < 0$  cases, reads

$$I_{l,\Delta n,n,l',m}(m_r, m_u, n_u, t) = M_m \sum_{s=0}^{\Delta n} M_s \sum_{k=\lceil \frac{|m|+l'}{2} \rceil}^{l'} M_k$$

$$\times \begin{cases} \frac{\Gamma(\frac{1+\gamma(k)}{2})}{\Gamma(\frac{3+\nu+\gamma(k)}{2})} \cdot {}_3F_2\left(\frac{\kappa(s)+1}{2}, \frac{\kappa(s)+2}{2}, \frac{1+\gamma(k)}{2}; \frac{1}{2}, \frac{3+\nu+\gamma(k)}{2}; -a^2(t)n^2a_0^2\right) & \text{for } \gamma(k) \text{ even} \\ ia(t)na_0(\kappa(s)+1)\frac{\Gamma(\frac{2+\gamma(k)}{2})}{\Gamma(\frac{4+\nu+\gamma(k)}{2})} \cdot {}_3F_2\left(\frac{\kappa(s)+2}{2}, \frac{\kappa(s)+3}{2}, \frac{2+\gamma(k)}{2}; \frac{3}{2}, \frac{4+\nu+\gamma(k)}{2}; -a^2(t)n^2a_0^2\right) & \text{for } \gamma(k) \text{ odd} \end{cases}, \quad (\text{B.64})$$

$$\gamma(k) = 2k - |m| - l' + m_u, \quad (\text{B.65})$$

$$\kappa(s) = l + l' + m_r + s, \quad (\text{B.66})$$

$$\nu = l + |m| + n_u. \quad (\text{B.67})$$

Despite not being very elegant, it helps to formally solve all integrals involved in the interference terms. For example, the overlap term can be expressed as

$$\langle \psi_b(t) | \psi_T(t) \rangle \propto I(2, 0, 0, t) \int_0^{2\pi} d\varphi e^{i(l-m)\varphi}. \quad (\text{B.68})$$

For fixed values of the quantum numbers the occurring hypergeometric functions can be expressed in elementary functions, for example  ${}_3F_2\left(\frac{1}{2}, 1, \frac{1}{2}; \frac{1}{2}, \frac{3}{2}; -a^2\right) = \arctan(a)/a$ .

Another approximation can be made to render  $I$  either real or purely imaginary, namely

$$ia \approx -\frac{i}{\hbar} qA, \quad (\text{B.69})$$

since  $r_{\omega_0}(1 - i\tau)/\sigma^2$  is small for  $|r_{\omega_0}| \ll \alpha^2$ . The approximation works well for times when the free wavepacket is close to the core region ( $r_{\omega_0}(t) \approx 0$ ,  $A(t) \approx \max$ ) and decreases in accuracy when the quiver amplitude has its peak ( $r_{\omega_0}(t) \approx \max$ ,  $A(t) \approx 0$ ). Furthermore, the transition elements have a prefactor  $\exp\left[-\frac{r_{\omega_0}^2(t)(1-i\tau(t))}{2\sigma^2(t)}\right]$  additionally suppressing the terms which are not so well approximated.

## B.5 Summation over emission directions

The integration over all possible field mode directions is performed in spherical coordinates

$$\vec{e}_k = \vec{e}_r, \quad \vec{e}_{\vec{k},1} = \vec{e}_{\theta_k}, \quad \vec{e}_{\vec{k},2} = \vec{e}_{\varphi_k} \quad (\text{B.70})$$

The unit vectors can be expressed with their cartesian counterparts

$$\vec{e}_k = \sin \theta_k \cos \varphi_k \vec{e}_x + \sin \theta_k \sin \varphi_k \vec{e}_y + \cos \theta_k \vec{e}_z, \quad (\text{B.71})$$

$$\vec{e}_{\vec{k},1} = \cos \theta_k \cos \varphi_k \vec{e}_x + \cos \theta_k \sin \varphi_k \vec{e}_y - \sin \theta_k \vec{e}_z, \quad (\text{B.72})$$

$$\vec{e}_{\vec{k},2} = -\sin \varphi_k \vec{e}_x + \cos \varphi_k \vec{e}_y. \quad (\text{B.73})$$

We calculate the dot product with an arbitrary complex vector  $\vec{a}$  and its absolute square. The expressions read

$$\vec{\epsilon}_{\vec{k},1} \cdot \vec{a} = \sin \theta_k \cos \varphi_k a_x + \sin \theta_k \sin \varphi_k a_y + \cos \theta_k a_z, \quad (\text{B.74})$$

$$\begin{aligned} \left| \vec{\epsilon}_{\vec{k},1} \cdot \vec{a} \right|^2 &= \sin^2 \theta_k \cos^2 \varphi_k |a_x|^2 + \sin^2 \theta_k \sin^2 \varphi_k |a_y|^2 + \cos^2 \theta_k |a_z|^2 \\ &\quad + 2\Re \left[ \cos^2 \theta_k \cos \varphi_k \sin \varphi_k a_x^* a_y - \sin \theta_k \cos \theta_k \cos \varphi_k a_x^* a_z \right. \\ &\quad \left. - \cos \theta_k \sin \theta_k \sin \varphi_k a_y^* a_z \right], \end{aligned} \quad (\text{B.75})$$

$$\vec{\epsilon}_{\vec{k},2} \cdot \vec{a} = -\sin \varphi_k a_x + \cos \varphi_k a_y, \quad (\text{B.76})$$

$$\left| \vec{\epsilon}_{\vec{k},2} \cdot \vec{a} \right|^2 = \sin^2 \varphi_k |a_x|^2 + \cos^2 \varphi_k |a_y|^2 - 2\Re [\cos \varphi_k \sin \varphi_k a_x^* a_y]. \quad (\text{B.77})$$

The integration over the unit sphere can be carried out

$$\int d\Omega_k \left| \vec{\epsilon}_{\vec{k},1} \cdot \vec{a} \right|^2 = \int_0^{2\pi} d\varphi_k \int_0^\pi d\theta_k \cos \theta_k \left| \vec{\epsilon}_{\vec{k},1} \cdot \vec{a} \right|^2 \quad (\text{B.78})$$

$$= \frac{2\pi}{3} \left[ |a_x|^2 + |a_y|^2 + 4|a_z|^2 \right], \quad (\text{B.79})$$

$$\int d\Omega_k \left| \vec{\epsilon}_{\vec{k},2} \cdot \vec{a} \right|^2 = \frac{2\pi}{3} \left[ 3|a_x|^2 + 3|a_y|^2 \right], \quad (\text{B.80})$$

$$\Rightarrow \int d\Omega_k \sum_\lambda \left| \vec{\epsilon}_{\vec{k},\lambda} \cdot \vec{a} \right|^2 = \frac{8\pi}{3} \left[ |a_x|^2 + |a_y|^2 + |a_z|^2 \right] = \frac{8\pi}{3} |\vec{a}|^2. \quad (\text{B.81})$$

and all real part terms vanish for the  $\varphi_k$  integration.



# C Miscellaneous

## C.1 Atomic units

Atomic units are often employed in atomic physics to simplify the equations and to express physical quantities in units of typical scales of the system. For example, the typical length scale for a Hydrogen atom is the Bohr radius  $a_0$  and is set to unity. All quantities set to unity are listed in Table C.1 alongside with some derived quantities.

| Quantity                          | Atomic units | SI units                   |
|-----------------------------------|--------------|----------------------------|
| Bohr radius $a_0$                 | 1            | $5.29 \times 10^{-11}$ m   |
| Reduced Planck's constant $\hbar$ | 1            | $1.06 \times 10^{-34}$ J   |
| Electron mass $m_e$               | 1            | $9.10 \times 10^{-31}$ kg  |
| Electric charge $ e $             | 1            | $1.60 \times 10^{-16}$ C   |
| Vacuum permittivity $\epsilon_0$  | $1/4\pi$     | $8.85 \times 10^{-12}$ F/m |
| Vacuum speed of light $c$         | 137.0        | $3 \times 10^8$ m/s        |

Table C.1: The physical quantities defining the atomic unit system and two additional constants are presented with their corresponding values in SI units [56].

## C.2 Expectation value of momentum operator for stationary bound eigenstates

For the time-independent Schrödinger equation

$$E_n |n\rangle = \hat{H} |n\rangle = \left[ \frac{\hat{p}^2}{2m_e} + V(\hat{r}) \right] |n\rangle,$$

the expectation value of the momentum operator

$$\langle n | \hat{p} | n \rangle \propto \langle n | \left[ \hat{H}, \hat{r} \right] | n \rangle = \langle n | \underbrace{\left[ E_n, \hat{r} \right]}_{=0} | n \rangle = 0$$

vanishes for energy eigenstates. Physically speaking, a stationary bound state for a time-independent potential must be bound to some region in space. If the expectation value were non-zero, then it would correspond to a bulk motion of the whole wavefunction, namely  $\langle \hat{r} \rangle \neq \text{const.}$  After some time the wavepacket would leave the region it is bound to.





# Bibliography

- [1] F. Krausz and M. Ivanov, *Attosecond Physics*. Reviews of Modern Physics **81**, 163 (2009).
- [2] C. Winterfeldt, C. Spielmann, and G. Gerber, *Colloquium: Optimal Control of High-Harmonic Generation*. Reviews of Modern Physics **80**, 117 (2008).
- [3] A. McPherson *et al.*, *Studies of Multiphoton Production of Vacuum-Ultraviolet Radiation in the Rare Gases*. Journal of the Optical Society of America B **4**, 595 (1987).
- [4] T. Popmintchev *et al.*, *Bright Coherent Ultrahigh Harmonics in the keV X-ray Regime from Mid-Infrared Femtosecond Lasers*. Science **336**, 1287 (2012).
- [5] M. Drescher *et al.*, *Time-Resolved Atomic Inner-Shell Spectroscopy*. Nature **419**, 803 (2002).
- [6] K. Y. Bliokh, Y. P. Bliokh, S. Savel'ev, and F. Nori, *Semiclassical Dynamics of Electron Wave Packet States with Phase Vortices*. Physical Review Letters **99**, (2007).
- [7] K. Y. Bliokh, M. R. Dennis, and F. Nori, *Relativistic Electron Vortex Beams: Angular Momentum and Spin-Orbit Interaction*. Physical Review Letters **107**, (2011).
- [8] S. Lloyd, M. Babiker, G. Thirunavukkarasu, and J. Yuan, *Electron Vortices: Beams with Orbital Angular Momentum*. Reviews of Modern Physics **89**, (2017).
- [9] M. MacDonald, K. Volke-Sepulveda, L. Paterson, J. Arlt, W. Sibbett, and K. Dholakia, *Revolving Interference Patterns for the Rotation of Optically Trapped Particles*. Optics Communications **201**, 21 (2002).
- [10] J. Rusz and S. Bhowmick, *Boundaries for Efficient Use of Electron Vortex Beams to Measure Magnetic Properties*. Physical Review Letters **111**, (2013).
- [11] K. Bliokh *et al.*, *Theory and Applications of Free-Electron Vortex States*. Physics Reports **690**, 1 (2017).
- [12] W. Paufler, B. Böning, and S. Fritzsche, *Strong-Field Ionization with Twisted Laser Pulses*. Physical Review A **97**, (2018).
- [13] C. Hernández-García, L. Rego, J. S. Román, A. Picón, and L. Plaja, *Attosecond Twisted Beams from High-Order Harmonic Generation Driven by Optical Vortices*. High Power Laser Science and Engineering **5**, (2017).
- [14] G. Gariepy *et al.*, *Creating High-Harmonic Beams with Controlled Orbital Angular Momentum*. Physical Review Letters **113**, (2014).
- [15] M. Zürch, C. Kern, P. Hansinger, A. Dreischuh, and C. Spielmann, *Strong-Field Physics with Singular Light Beams*. Nature Physics **8**, 743 (2012).
- [16] V. S. Yakovlev and A. Scrinzi, *High Harmonic Imaging of Few-Cycle Laser Pulses*. Physical Review Letters **91**, (2003).
- [17] A. Baltuška *et al.*, *Attosecond Control of Electronic Processes by Intense Light Fields*. Nature **421**, 611 (2003).

- 
- [18] M. Lewenstein, P. Balcou, M. Y. Ivanov, A. L'Huillier, and P. B. Corkum, *Theory of High-Harmonic Generation by Low-Frequency Laser Fields*. Physical Review A **49**, 2117 (1994).
- [19] M. B. Gaarde, J. L. Tate, and K. J. Schafer, *Macroscopic Aspects of Attosecond Pulse Generation*. Journal of Physics B: Atomic, Molecular and Optical Physics **41**, 132001 (2008).
- [20] W. Greiner, *Classical Electrodynamics* (Springer New York, 1998).
- [21] R. Schmidt, *Theoretische Elektrodynamik*. , Lecture notes, 2010.
- [22] D. G. Lappas, M. V. Fedorov, and J. H. Eberly, *Spectrum of Light Scattered by a Strongly Driven Atom*. Physical Review A **47**, 1327 (1993).
- [23] J. C. Baggesen and L. B. Madsen, *On the Dipole, Velocity and Acceleration Forms in High-Order Harmonic Generation from a Single Atom or Molecule*. Journal of Physics B: Atomic, Molecular and Optical Physics **44**, 115601 (2011).
- [24] D. J. Diestler, *Harmonic Generation: Quantum-Electrodynamical Theory of the Harmonic Photon-Number Spectrum*. Physical Review A **78**, (2008).
- [25] K. C. Kulander, K. J. Schafer, and J. L. Krause, *Super-Intense Laser-Atom Physics* (Springer US, 1993).
- [26] P. B. Corkum and F. Krausz, *Attosecond Science*. Nature Physics **3**, 381 (2007).
- [27] M. Protopapas, C. H. Keitel, and P. L. Knight, *Atomic Physics with Super-High Intensity Lasers*. Reports on Progress in Physics **60**, 389 (1997).
- [28] M. Protopapas, D. G. Lappas, C. H. Keitel, and P. L. Knight, *Recollisions, Bremsstrahlung, and Attosecond Pulses from Intense Laser Fields*. Physical Review A **53**, R2933 (1996).
- [29] G. van de Sand and J. M. Rost, *Semiclassical Description of Multiphoton Processes*. Physical Review A **62**, (2000).
- [30] F. Grossmann, *Theoretical Femtosecond Physics* (Springer International Publishing, 2013).
- [31] R. M. Potvliege and R. Shakeshaft, *Multiphoton Processes in an Intense Laser Field: Harmonic Generation and Total Ionization Rates for Atomic Hydrogen*. Physical Review A **40**, 3061 (1989).
- [32] L. Allen, M. W. Beijersbergen, R. J. C. Spreeuw, and J. P. Woerdman, *Orbital Angular Momentum of Light and the Transformation of Laguerre-Gaussian Laser Modes*. Physical Review A **45**, 8185 (1992).
- [33] K. Y. Bliokh and F. Nori, *Transverse and Longitudinal Angular Momenta of Light*. Physics Reports **592**, 1 (2015).
- [34] M. Uchida and A. Tonomura, *Generation of Electron Beams Carrying Orbital Angular Momentum*. Nature **464**, 737 (2010).
- [35] J. Verbeeck, H. Tian, and P. Schattschneider, *Production and Application of Electron Vortex Beams*. Nature **467**, 301 (2010).
- [36] E. Cavanagh and B. Cook, *Numerical Evaluation of Hankel Transforms via Gaussian-Laguerre Polynomial Expansions*. IEEE Transactions on Acoustics, Speech, and Signal Processing **27**, 361 (1979).

- [37] N. J. Kylstra, R. A. Worthington, A. Patel, P. L. Knight, J. R. V. de Aldana, and L. Roso, *Breakdown of Stabilization of Atoms Interacting with Intense, High-Frequency Laser Pulses*. Physical Review Letters **85**, 1835 (2000).
- [38] M. W. Walser, C. H. Keitel, A. Scrinzi, and T. Brabec, *High Harmonic Generation Beyond the Electric Dipole Approximation*. Physical Review Letters **85**, 5082 (2000).
- [39] H. R. Reiss, *Dipole-Approximation Magnetic Fields in Strong Laser Beams*. Phys. Rev. A **63**, 013409 (2000).
- [40] C. Zagoya, C.-M. Goletz, F. Grossmann, and J.-M. Rost, *Dominant-Interaction Hamiltonians for High-Order-Harmonic Generation in Laser-Assisted Collisions*. Physical Review A **85**, (2012).
- [41] C. Zagoya, C.-M. Goletz, F. Grossmann, and J.-M. Rost, *An Analytical Approach to High Harmonic Generation*. New Journal of Physics **14**, 093050 (2012).
- [42] K. Drühl and J. K. McIver, *Charged Particles in an Intense, Plane Electromagnetic Wave: Limitations of the Nonrelativistic Theory*. Journal of Mathematical Physics **24**, 705 (1983).
- [43] N. J. Kylstra, R. M. Potvliege, and C. J. Joachain, *Photon Emission by Ions Interacting with Short Intense Laser Pulses: Beyond the Dipole Approximation*. Journal of Physics B: Atomic, Molecular and Optical Physics **34**, L55 (2001).
- [44] C. C. Chirilă, N. J. Kylstra, R. M. Potvliege, and C. J. Joachain, *Nondipole Effects in Photon Emission by Laser-Driven Ions*. Physical Review A **66**, (2002).
- [45] H. R. Reiss, *Complete Keldysh Theory and its Limiting Cases*. Physical Review A **42**, 1476 (1990).
- [46] D. V. Karlovets, *Electron with Orbital Angular Momentum in a Strong Laser Wave*. Physical Review A **86**, (2012).
- [47] V. A. Zaytsev, V. G. Serbo, and V. M. Shabaev, *Radiative Recombination of Twisted Electrons with Bare Nuclei: Going Beyond the Born Approximation*. Physical Review A **95**, (2017).
- [48] R. V. Boxem, B. Partoens, and J. Verbeeck, *Rutherford Scattering of Electron Vortices*. Physical Review A **89**, (2014).
- [49] C. R. Greenshields, R. L. Stamps, S. Franke-Arnold, and S. M. Barnett, *Is the Angular Momentum of an Electron Conserved in a Uniform Magnetic Field?*. Physical Review Letters **113**, (2014).
- [50] S. M. Barnett, *Relativistic Electron Vortices*. Physical Review Letters **118**, (2017).
- [51] I. Bialynicki-Birula and Z. Bialynicka-Birula, *Relativistic Electron Wave Packets Carrying Angular Momentum*. Physical Review Letters **118**, (2017).
- [52] A. G. Hayrapetyan, O. Matula, A. Aiello, A. Surzhykov, and S. Fritzsche, *Interaction of Relativistic Electron-Vortex Beams with Few-Cycle Laser Pulses*. Physical Review Letters **112**, (2014).
- [53] K. Y. Bliokh, P. Schattschneider, J. Verbeeck, and F. Nori, *Electron Vortex Beams in a Magnetic Field: A New Twist on Landau Levels and Aharonov-Bohm States*. Physical Review X **2**, (2012).

- [54] H. Goldstein, C. P. P. Jr., and J. L. Safko, *Classical Mechanics (3rd Edition)* (Pearson, 2001).
- [55] L. D. Landau and E. M. Lifshitz, *The Classical Theory of Fields* (Pergamon, 1971).
- [56] C. E. Burkhardt and J. J. Leventhal, *Foundations of Quantum Physics* (Springer New York, 2008).
- [57] Wolfram Research, Inc., *Mathematica, Version 11.3.*, 2018.
- [58] M. V. Frolov, N. L. Manakov, W.-H. Xiong, L.-Y. Peng, J. Burgdörfer, and A. F. Starace, *Scaling Laws for High-Order-Harmonic Generation with Midinfrared Laser Pulses*. *Physical Review A* **92**, (2015).
- [59] F. Hildebrand, *Introduction to Numerical Analysis: Second Edition, Dover Books on Mathematics* (Dover Publications, 2013).
- [60] P. Holoborodko, *Gauss-Legendre Quadrature for C/C++.*, <http://www.holoborodko.com/pavel/numerical-methods/numerical-integration/>, 2018, Accessed: 2018-04-09.
- [61] C. J. Joachain, N. J. Kylstra, and R. M. Potvliege, *Atoms in Intense Laser Fields* (Cambridge University Press, 2012).
- [62] M. Feit, J. Fleck, and A. Steiger, *Solution of the Schrödinger Equation by a Spectral Method*. *Journal of Computational Physics* **47**, 412 (1982).
- [63] A. D. Bandrauk and H. Shen, *Exponential Split Operator Methods for Solving Coupled Time-Dependent Schrödinger Equations*. *The Journal of Chemical Physics* **99**, 1185 (1993).
- [64] M. Frigo and S. G. Johnson, *The Design and Implementation of FFTW3*. *Proceedings of the IEEE* **93**, 216 (2005), Special issue on “Program Generation, Optimization, and Platform Adaptation”.
- [65] U. V. Riss and H.-D. Meyer, *Investigation on the Reflection and Transmission Properties of Complex Absorbing Potentials*. *The Journal of Chemical Physics* **105**, 1409 (1996).
- [66] S. Brennecke and M. Lein, *High-Order Above-Threshold Ionization Beyond the Electric Dipole Approximation*. *Journal of Physics B: Atomic, Molecular and Optical Physics* **51**, 094005 (2018).
- [67] D. J. Griffiths, *Introduction to Quantum Mechanics* (Cambridge University Press, 2016).
- [68] J. J. Sakurai, *Advanced Quantum Mechanics* (Addison-Wesley Publishing Company, 1967).
- [69] A. V. Bogatskaya, E. A. Volkova, V. Y. Kharin, and A. M. Popov, *Polarization Response in Extreme Nonlinear Optics: When can the Semiclassical Approach be used?*. *Laser Physics Letters* **13**, 045301 (2016).
- [70] J. Mur-Petit, A. Polls, and F. Mazzanti, *The Variational Principle and Simple Properties of the Ground-State Wave Function*. *American Journal of Physics* **70**, 808 (2002).
- [71] A. V. Bogatskaya, E. A. Volkova, and A. M. Popov, *Prospects of Odd and Even Harmonic Generation by an Atom in a High-Intensity Laser Field*. *Laser Physics Letters* **14**, 055301 (2017).
- [72] A. V. Bogatskaya, E. A. Volkova, and A. M. Popov, *Spontaneous Emission of Atoms in a Strong Laser Field*. *Journal of Experimental and Theoretical Physics* **125**, 587 (2017).

- [73] A. V. Bogatskaya, E. A. Volkova, and A. M. Popov, *Spontaneous emission from the Atom Stabilized by a Strong High-Frequency Laser Field*. *Laser Physics* **27**, 095302 (2017).
- [74] R. Loudon, *The Quantum Theory of Light* (OUP Oxford, 2000).
- [75] J. D. Jackson, *Classical Electrodynamics* (John Wiley & Sons, 2012).
- [76] G. Compagno, R. Passante, and F. Persico, *Atom-Field Interactions and Dressed Atoms* (Cambridge University Press, 2005), Vol. 17.
- [77] K. Blum, *Density Matrix Theory and Applications* (Springer Science & Business Media, 2012), Vol. 64.
- [78] J. Tate, T. Augustine, H. G. Muller, P. Salières, P. Agostini, and L. F. DiMauro, *Scaling of Wave-Packet Dynamics in an Intense Midinfrared Field*. *Physical Review Letters* **98**, (2007).
- [79] H. R. Reiss and V. P. Krainov, *Approximation for a Coulomb-Volkov Solution in Strong Fields*. *Physical Review A* **50**, R910 (1994).
- [80] G. Duchateau, E. Cormier, H. Bachau, and R. Gayet, *Coulomb-Volkov Approach of Atom Ionization by Intense and Ultrashort Laser Pulses*. *Physical Review A* **63**, (2001).
- [81] K. Mishima, M. Hayashi, J. Yi, S. H. Lin, H. L. Selzle, and E. W. Schlag, *Theoretical Studies of the Long-Range Coulomb Potential Effect on Photoionization by Strong Lasers*. *Physical Review A* **66**, (2002).
- [82] E. J. Heller, *Time-Dependent Approach to Semiclassical Dynamics*. *The Journal of Chemical Physics* **62**, 1544 (1975).
- [83] H. A. Kramers, *Collected Scientific Papers* (North-Holland Publishing Company, 1956).
- [84] W. C. Henneberger, *Perturbation Method for Atoms in Intense Light Beams*. *Physical Review Letters* **21**, 838 (1968).
- [85] H. Bateman, in *Table of Integral Transforms*, edited by A. Erdelyi (McGraw-Hill Inc., 1954), Vol. 1 and 2.



# Acknowledgements

First and foremost, I want to sincerely thank Prof. Dr. Jan-Michael Rost for the great opportunity to write this thesis in his group. His guidance, encouragement and valuable insights were of invaluable assistance. Also greatly appreciated is his constant availability for discussions and his pedagogical way of explaining due to which I learned quite a lot. I am also very grateful for patience whenever I did not understand a problem or topic at first or nearly missed an important deadline. I would also like to acknowledge his kind offer to proofread a draft of this thesis.

I want to express my gratitude to Dr. Frank Grossmann, who also kindly agreed to be the second referee for this thesis. I learned a great deal from his lecture in *Femtosecond Physics*, his book on the same topic and the personal meetings, for which he was always available.

The “Max-Planck-Institut für Physik komplexer Systeme” is an excellent place to work and I feel lucky and grateful, that I had the opportunity to benefit from its facilities and to use its computing resources, on which most of the numerical calculations in this work were performed.

For his advice, all the helpful discussions and numerous assistances throughout our time as students at the “Technische Universität Dresden” my thanks go to Felix. I sincerely hope that our academic paths will cross one day.

This thesis has benefited significantly from its many proofreaders and, therefore, I am indebted to Brimel, Felix, Clemens, Jacob, Lia, Lisa and Erik.

I also want to thank Friedrich, Sebastian and Paul for many good distractions, shared laughs and good advices during lunchtime in the “Alte Mensa”.

Thanks again to Brimel, who kept me motivated a great deal and encouraged me to keep on working toward the completion of this thesis.

I thank my fellow students Arne, Breti, Clemens, Felix, Jacob, Kussi, Paul and Tom for a very memorable time, beginning from the first days as new freshman students.

Suse’s encouragement, cheerful spirit and her own amusing interpretation of a twisted electron, “Quantenquirl”, are also greatly appreciated.

Finally, and most importantly to me, I want to especially thank my parents for their incredible support and immeasurable encouragement along my own personal journey. This thesis and everything that led to it would not have been possible without them.

Thank you.

### **Statement of authorship**

I hereby certify that I have authored this Master Thesis entitled *High Harmonic Generation with Twisted Electrons* independently and without undue assistance from third parties. No other than the resources and references indicated in this thesis have been used. I have marked both literal and accordingly adopted quotations as such. There were no additional persons involved in the intellectual preparation of the present thesis. I am aware that violations of this declaration may lead to subsequent withdrawal of the degree.

Dresden, 20th July 2018

Sebastian Gemsheim